Parasitic Resonances in High Power Proton Linacs: Major Issues and Mitigation Techniques

Robert Ainsworth

Department of Physics

Royal Holloway, University of London

This thesis is submitted to the University of London for the degree of Doctor of Philosophy

June 2014

I Robert Ainsworth hereby declare that this thesis and the work presented in it is entirely my own. Where I have consulted the work of others, this is always clearly stated.

This thesis is dedicated to the memory of my Nan.

'To Infinity and Beyond...'

Buzz Lightyear

Acknowledgements

Firstly, I would like to thank my supervisor Stephen Molloy for help with this thesis. His supervision was brilliant and in many occasions went above and beyond what was required for a supervisor in both work and life.

Secondly, I would like to thank my second supervisor Stewart Boogert for his help during my PhD and for giving me my chance in accelerator physics.

A big thank you to Alexey Lyapin, who gave me a lot of help along the way especially at the beginning of my PhD.

Next I would like to thank my friends and colleagues who helped me, especially, Young-Im Kim, Laurie Nevay, Frankie Cullinan, Will Shields, Tom Aumeyr, Gary Boorman and Jochem Snuverink.

I would also like to thank Kwok Ko for inviting me to work at SLAC for two months to improve my knowledge of the ACE3P code. In particular, I would also like to thank Cho Ng, Arno Candel and Justin Rodriguez for their help during this period.

I would like to thank Nicoleta Baboi, Thomas Wamsat and Pei Zhang for their help performing measurements at DESY.

Next, I would like to thank Mats Lindroos, Steve Peggs and Dave McGinnis for inviting to work at ESS for an extended period of time and for always making me feel welcome.

Finally, I would like to thank my amazing Im for bringing me the greatest happiness (and for helping me to finish this damn thesis).

Abstract

Parasitic resonances in superconducting rf cavities may make the beam unstable and increase the cryogenic load in high power proton machines. Therefore, Same Order Modes (SOMs) and Higher Order Modes (HOMs) must be investigated fully in order to determine if damping is required.

A beam dynamics code was used developed to study the interaction of these resonances with the beam for various European Spallation Source (ESS) lattices. Each linac design is characterised by the initial kinetic energy of the beam, as well as by the velocity of the beam at each of the points at which the cavity style changes. The scale of the phase-space disruption of the proton pulse is discussed taking into account amplitude and phase errors from the Klystron, injection errors, alignment errors and the frequency spread the SOMs and HOMs.

Mitigation techniques using HOM couplers are also investigated for cavities resonating at 704 MHz. Multipacting in these couplers is a concern as thermally induced detuning of the fundamental notch filter has limited the achievable gradient in other high power machines. It is therefore important to avoid potential multipacting conditions during the design phase. Presented here are simulations using the Track3P code developed at SLAC. Multipacting regions are highlighted and the suitability of proposed HOM coupler designs are discussed.

Contents

List of Figures

List of Tables

Chapter 1

Introduction

The idea for Radio Frequnecy (rf) accelerators were first conceived in the early 1920's [1] and then realised by Wideröe [2] at the end of that decade with the construction of the first rf accelerator. In recent times, accelerators have been used in more and more applications, playing a role in major discoveries. In 2012, a new boson was discovered using the Large Hadron Collider (LHC) [3] at the European Organisation for Nuclear Research (CERN) [4] which led to the 2013 Nobel prize in physics being awarded. In addition to the study of the universe, accelerators are also in used medical applications including cancer therapy and the study of matter using light and neutron sources. The accelerator is an excellent tool and it can be confidently expected, that major advances in the future will be made with their continued use.

Accelerators can be described as either circular machines or linear machines. For a circular machine, the beam is bent in a circular orbit and stays in the machine for many turns, whereas in a linear machine, the beam traverses the machine only once. The force F, on a particle with charge q, moving through a Electric field $\vec{E}$ and Magnetic field $\vec{B}$ is given by

$$F = q(\vec{E} + \vec{v} \times \vec{B}). \tag{1.1}$$

It can be seen from this equation that $\vec{E}$ can cause a change in kinetic energy and $\vec{B}$ causes a centripetal force perpendicular to the electrons velocity v. Due to this, acceleration is performed using the electric field. Magnets

are used for the deflecting or focusing of the beam since it would require an unrealistically large electric field depending on the mass and kinetic energy of 300 MV/m to provide the same deflection as an easily obtainable magnetic field of 1 T. A more detail explanation of accelerator physics can be found in [5].

Acceleration is usually realised using either an electrostatic or rf electric field inside a cavity. For a rf accelerator, one of the key building blocks is the cavities which come in many different forms and are optimised for specific applications. Cavities can be divided into two types: normal conducting or superconducting. For many years, copper-cavity linacs were the preference however a large amount of rf power is required due to the ohmic losses in the cavity walls. The losses in superconducting radio frequency (SRF) cavities are almost 10^5 smaller and could result in massive power savings even including the cryogenics requirements making them an increasingly attractive option for future linacs.

1.1 Superconducting RF linacs

The use of superconducting cavities in linacs is becoming more popular. Some examples of SRF linacs are presented below.

1.1.1 Future Linear Collider

The further study of the universe is expected to require a next generation electron-positron collider with a centre of mass energy in the TeV range. One proposal is the International Linear Collider (ILC) [6, 7] which will consist of two SRF linacs, each on the order of 15 km long, accelerating electrons and positrons up to an energy of 500 GeV. The linac will consist of close to 16,000 SRF cavities with accelerating gradients on the order of 31.5 MV/m.

1.1.2 Free Electron Lasers

Another important application is 4^{th} generation light sources, also known as Free Electron Lasers (FELs) [8, 9]. A SRF linac may be used to accelerate

electrons until they pass through an insertion device. Here, an alternating magnetic field in the transverse direction causes the electrons to undulate and results in the production of coherent synchrotron radiation.

1.1.3 Spallation Sources

So far, only lepton machines have been discussed, however, protons and other hadrons can also be accelerated. Acceleration is more difficult due to the significantly heavier mass of these particles meaning the the velocity gain with beam energy is much slower. Recently, there has become a demand for high power applications requiring several megawatts of beam power.

Neutron scattering, a method to investigate materials, was pioneered in the 1950s. Figure 1.1 shows the evolution of neutron facilities which has been updated from [10]. Early research reactors developed instrumental techniques which began to unravel the atomic structures of simple materials. In the late 1960s, a purpose-built high flux reactor source of slow neutrons was built in France known as Institut Laue-Langevin (ILL) [11]. ILL was at the forefront of neutron science as has remained there even 40 years on.

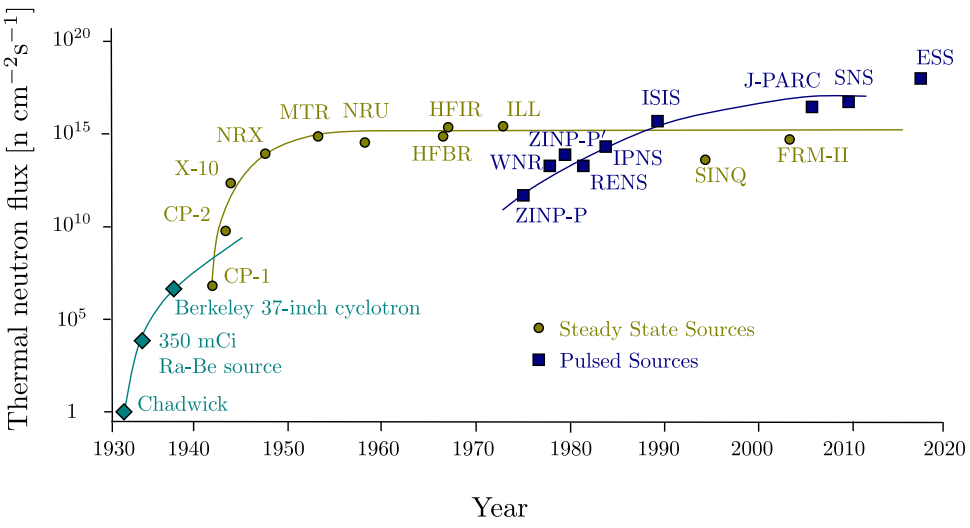

Figure 1.1: Comparison of the peak flux of thermal neutrons in facilities.

In parallel, accelerator-driven sources of neutrons were also developed. These facilities produced fast neutrons and were pulsed with high peak brightness. Early machines were based on electron linear accelerators which has significant background problems due to very intense gamma radiation bursts. To overcome this fundamental problem, proton machines were developed which do not suffer from the gamma background problems. ISIS [12], the world's first proton spallation source began construction in the late 1970s. Despite its relatively low power of 180 kW, it demonstrated that world class science could be carried out effectively with such sources.

In 2006, the first high power superconducting proton linac started operation at the Spallation Neutron Source (SNS) [13]. H^- are accelerated to the required energy using a SRF linac, stripped to produce protons and finally bunched in an accumulator ring before colliding with a liquid mercury target to produce neutrons which are used for material science. The European Spallation Source (ESS) [14] is a future neutron source and will be discussed in detail in Chapter 2.

1.1.4 Accelerator Driven Systems

Conventional fission reactors require neutrons which are produced during the fission reaction itself. One idea is to use a sub-critical reactor, in which additional neutrons are required to keep the reaction alive. These neutrons could be provided by an accelerator. This idea is known as an accelerator driven system (ADS) [15]. Nuclear waste transmutation is a possibility with this technique, in which long lived actinides are transmuted to shorter living products. Currently, there is the MYRRHA [16, 17] project which hopes to be an ADS demonstrator in Europe.

1.1.5 Radioactive Ion Beam Facilities

High power proton beams are also required for radioactive ion beam facilities (RIBs) such as the Facility for Rare Isotope Beams (FRIB) [18]. The basic

principle involves accelerating a beam into a target with the resulting collision creating a number of reaction products. Within these products are rare isotopes which can be studied or used for medical applications.

1.1.6 Neutrino Facilities

Next generation neutrino facilities also use high power proton beams. One mechanism involves the production of radioactive ions by a spallation process, which then decay via beta-decay in a storage ring and produce anti-electron neutrinos. For this to happen, a high power proton beam with kinetic energy on the order of GeV is needed. There exists the T2K [19] experiment at JPARC [20] already and future projects with this focus are the superconducting proton linac (SPL) [21] and Project X [22].

1.2 Parasitic Resonances

When travelling through a cavity, the beam does not only interact with the electric field related to the acceleration but also excites various other modes at different frequencies which are usually referred to as Higher Order Modes (HOMs). HOMs can be dangerous as they can lead to beam dynamics instabilities. The energy stored in these modes may also cause an additional heat load for the cryogenic cooling system thus, increasing cost and could possibly lead to a thermal breakdown. It is therefore, important to study the influence of these modes carefully to prevent problem during operation and to determine if damping is required and if so, the requirements.

1.3 Outline

In Chapter 2, high power proton linacs with be discussed with a focus on the European Spallation Source. The use of cavities for acceleration and parasitic modes will be discussed in detail.

Chapter 3 will focus on performing electromagnetic simulations on cavities and the results of these simulations for specific cavity designs highlighting dangerous modes.

Chapter 4 will focus on how these dangerous modes could affect the beam using a code developed to study this interaction, focusing on the ESS superconducting linac. A special focus is made to model quasi-relativistic beams taking into account other external effects such as errors from system used to power the cavities and beam noise. It will be determined if damping is required for the ESS linac and if so, the damping requirements.

In Chapter 5, potential HOM coupler designs for high power proton linacs will be investigated to determine their susceptibility to multipacting. The associated risk of each design will be discussed and modifications will be presented.

Chapter 2

Superconducting Linacs for High Power Proton Beams

Superconducting linacs have become an increasingly popular choice for high power proton beams. The SRF Linac for European Spallation Source (ESS) will be the main focus of this thesis and will be discussed in more detail. In this Chapter, accelerating cavities will be discussed with an emphasis on SRF cavities.

2.1 European Spallation Source

The European Spallation Source (ESS) is a facility for the generation of intense pulses of neutrons for studies in applied science. The accelerator is critical to operation and its role is to create protons at the source, accelerate them to the required energy, where they are then steered onto a target to create neutrons through the spallation process. In order to achieve a beam power of 5 MW, the protons will be accelerated to 2.5 GeV and average macro-pulse current of 50 mA. A more detailed explanation of is found the technical design report [23].

A general layout of the ESS linac is shown in figure 2.1. Protons are produced at the ion source (IRSC) and are then transported from a low energy beam transport (LEBT) section to a four-vane radio frequency quadrupole which accelerates and bunches the beam at 352.21 MHz. The beam then enters the normal conducting drift tube linac (DTL) via a medium energy beam

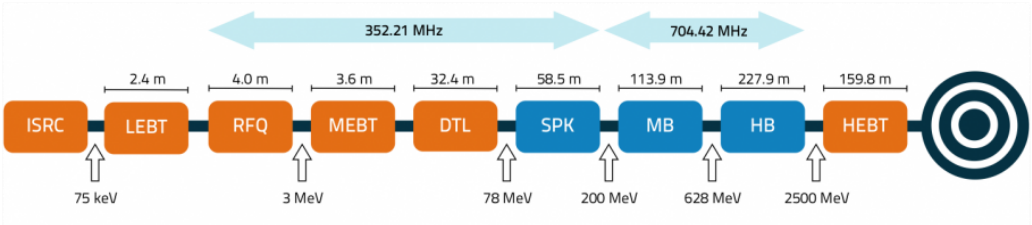

Figure 2.1: Block diagram of the ESS linac. The orange items are normal conducting, while the blue items are superconducting.

	Value	Unit
Final kinetic energy	2.5	GeV
Current	50	mA
Pulse repetition rate	14	Hz
Bunch frequency	352.21	MHz
Average power	5	MW
Peak power	125	MW

Table 2.1: Main ESS linac parameters.

transport (MEBT) section. From here, the beam enters the superconducting portion of the machine which consists of spoke (SPK) cavities, medium beta (MB) elliptical cavities and high beta (HB) elliptical cavities. The cavities in this section will immersed in liquid helium at a temperature of 2 K and are discussed in more detail below.

Spokes: Two–spoke cavities operating at 352.21 MHz. This section accelerates the beam from the exit of the DTL at 78 MeV to 200 MeV.

Medium β: Five–cell elliptical cavities operating at 704.42 MHz. The geometrical beta of this section is still under discussion, but is likely to be set at a value close to, $\beta_g = 0.65$. In this section, the beam is accelerated from 200 MeV to 628 MeV.

High β: Five–cell elliptical cavities operating at 704.42 MHz. As with the previous section, the geometrical beta is still under discussion, but the

likely value is close to, $\beta_g = 0.92$. This section accelerates the beam to its final energy of 2.5 GeV.

2.2 Cavity Basics

The focus of this thesis is parasitic resonances which will be introduced in this section along with principle of acceleration. To start with, the electromagnetic theory related to cavities is discussed and follows [24].

2.2.1 Maxwell's Equations

The laws describing all classical electromagnetism are contained within Maxwell's equations which relate the electric field $\vec{E}$ and magnetic field $\vec{B}$ with charge and current sources.

$$\nabla \cdot \vec{D} = \rho, \tag{2.1}$$

$$\nabla \cdot \vec{B} = 0, \tag{2.2}$$

$$\nabla \times \vec{E} = -\frac{\partial \vec{B}}{\partial t}, \tag{2.3}$$

$$\nabla \times \vec{H} = \vec{J} + \frac{\partial \vec{D}}{\partial t}, \tag{2.4}$$

where ρ is the charge density and $\vec{J}$ is the current density. The constitutive relations are

$$\vec{D} = \epsilon \vec{E}, \tag{2.5}$$

$$\vec{B} = \mu \vec{H}, \tag{2.6}$$

where ϵ is the permittivity, and μ is the permeability of the material in which the fields exist. In the simplest case, where there are no charges or materials such as a perfect, unbounded vacuum, the constitutive relations become

$$\vec{D} = \epsilon_0 \vec{E}, \text{ and } \vec{B} = \mu_0 \vec{H}, \tag{2.7}$$

where ϵ_0 and μ_0 are the permittivity and permeability of free space respectively. Maxwell's equations become

$$\nabla \cdot \vec{E} = 0, \tag{2.8}$$

$$\nabla \cdot \vec{B} = 0, \tag{2.9}$$

$$\nabla \times \vec{E} = -\frac{\partial \vec{B}}{\partial t}, \tag{2.10}$$

$$\nabla \times \vec{B} = \frac{1}{c^2}\frac{\partial \vec{E}}{\partial t}, \tag{2.11}$$

where $c = 1/\sqrt{\mu_0 \epsilon_0}$. A trivial solution exist where all the fields are equal to zero however, the more interesting non trivial solutions are found by separating the electric and magnetic fields. By taking the curl of (2.10)

$$\nabla \times \nabla \times \vec{E} = \nabla(\nabla \cdot \vec{E}) - \nabla^2 \vec{E} = -\frac{\partial}{\partial t}\nabla \times \vec{B}, \tag{2.12}$$

and inserting (2.8) and (2.11), the wave equation is obtained

$$\nabla^2 \vec{E} - \frac{1}{c^2}\frac{\partial^2 \vec{E}}{\partial t^2} = 0, \tag{2.13}$$

which can be solved with plane waves which depend on position $\vec{r}$ and time t.

$$\vec{E} = \vec{E}_0 e^{i(\vec{k}\cdot\vec{r}-\omega t)}, \tag{2.14}$$

where $\vec{E}_0$ is a constant vector and the phase velocity of the wave is given by the dispersion relation

$$v_p = \frac{\omega}{|k|}. \tag{2.15}$$

In a similar fashion an expression for the magnetic field can derived

$$\vec{B} = \vec{B}_0 e^{i(\vec{k}\cdot\vec{r}-\omega t)}, \tag{2.16}$$

where $\vec{B}_0$ is a constant vector and the phase velocity of the wave also defined by (2.15). Substituting the plane wave solutions back into Maxwell's equations results in the following constraints on the solutions

$$\vec{k} \cdot \vec{E}_0 = 0, \tag{2.17}$$

$$\vec{k} \cdot \vec{B}_0 = 0, \tag{2.18}$$

$$\vec{k} \times \vec{E}_0 = \omega \vec{B}_0, \tag{2.19}$$

$$\vec{k} \times \vec{B}_0 = -\frac{\omega}{c^2} \vec{E}_0. \tag{2.20}$$

It can be seen than $\vec{k}$, $\vec{E}_0$ and $\vec{B}_0$ are all mutually perpendicular and the field amplitudes are related by $E_0/B_0 = c$. A wave with a particular value of $\vec{k}$ can be referred to as a 'mode' of the electromagnetic fields in free space. One mode corresponds to a plane wave of single frequency with infinite extent in space and time.

2.2.2 Circular Waveguide

Consider a perfect circular waveguide which is a infinitely long hollow cylinder with a radius r_0 and perfectly conducting walls. Due to the rotational symmetry of the problem, a cylindrical coordinate system $\vec{x}(r, \theta, z)$ is now used. In the case of a perfect conductor, the following boundary conditions apply:

$$\vec{n} \times \vec{E} = 0, \;\; \vec{n} \cdot \vec{B} = 0, \tag{2.21}$$

where $\vec{n}$ is the surface normal. This problem has an infinite set of unique solutions split into two families known as transverse magnetic (TM) and transverse electric (TE) modes [25]. For the case of TM modes, there exists no magnetic field in the longitudinal direction and the longitudinal electric field can be found from the solution to the differential equation:

$$\frac{\partial^2 E_z}{\partial z^2} + \frac{1}{r}\frac{\partial E_z}{\partial r} + \frac{\partial^2 E_z}{\partial r^2} - \frac{1}{c^2}\frac{\partial^2 E_z}{\partial t^2} = 0. \tag{2.22}$$

The boundary conditions from (2.21) require that $E_z(r_0) = 0$ and thus, lead to a solution of the from

$$E_z \sim E_0 J_m \left(\frac{j_{n,m}}{r_0} r \right) e^{j\omega t}, \tag{2.23}$$

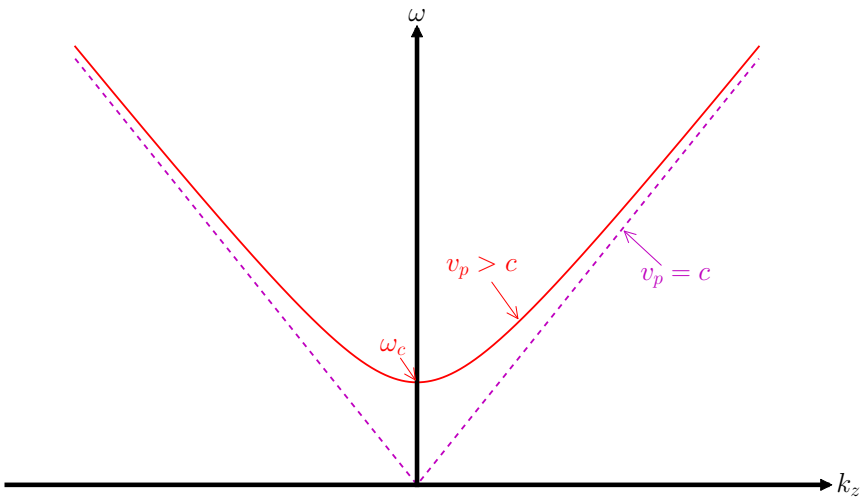

Figure 2.2: Dispersion diagram.

where $j_{n,m}$ is the n^{th} zero of the m^{th} order Bessel function J_m. The dispersion relation is given by

$$\omega_{TM,mn}^2 = \left(\frac{cj_{n,m}}{r_0}\right)^2 + k_z^2, \tag{2.24}$$

where k_z is the propagation constant in the z direction. A dispersion diagram is shown in Figure 2.2. The phase velocity at any point on the dispersion curve is the slope of the line starting at the origin to that point. The phase velocity is always greater than the speed of light and modes can only propagate along the z-axis if their frequency is above the cutoff frequency

$$f_{TM,c} = \frac{c}{r_0 2\pi} j_{n,m}. \tag{2.25}$$

TE modes, in which the longitudinal electric field component vanishes can be dealt with in a similar way. The longitudinal magnetic field is of the form

$$B_z \sim J_m\left(\frac{j'_{n,m}}{r_0} r\right) e^{i\omega t}, \tag{2.26}$$

where $j'_{n,m}$ is the n^{th} zero of the derivative of the m^{th} order Bessel function. The dispersion relation for TE modes is then

$$\omega_{TE,mn}^2 = \left(\frac{cj'_{n,m}}{r_0}\right)^2 + k_z^2, \tag{2.27}$$

and the associated cutoff frequency

$$f_{TE,c} = \frac{c}{r_0 2\pi} j'_{n,m}. \tag{2.28}$$

2.2.3 Pillbox Cavity

A pillbox cavity of length l and radius R_c can be constructed from a circular waveguide with end caps at the coordinates $z = 0$ and $z = l$. The electromagnetic field profiles inside the pillbox can be derived analytically.

The pillbox cavity also has a set of solutions similar to the circular waveguide which can be classed as TM and TE, however due to the addition of end caps, a discrete mode spectrum is produced. A third index p is used to define the mode. The dispersion relation for TM modes becomes

$$\omega_{TM,mnp} = c\sqrt{k_{TM,nm}^2 + k_z^2}, \tag{2.29}$$

where $k_{TM,nm} = j_{nm}/R_c$ and $k_z = p\pi/l$ and the corresponding relation for TE modes is

$$\omega_{TE,mnp} = c\sqrt{k_{TM,nm}^2 + k_z^2}, \tag{2.30}$$

where $k_{TE,nm} = j'_{nm}/R_c$.

The general expressions for the electric and magnetic fields of type $\mathrm{TM_{mnp}}$ in a pillbox cavity are

Figure 2.3: The electric field and magnetic fields for a TM_{010} mode in a pillbox cavity.

$$
\begin{aligned}
E_z &= E_0 J_m(k_{mn} r)\cos m\theta \cos\frac{p\pi z}{l} e^{j\omega t},\\
E_r &= -\frac{p\pi}{l}\frac{a}{x_{mn}} E_0 J'_m(k_{mn} r)\cos m\theta \sin\frac{p\pi z}{l} e^{j\omega t},\\
E_\theta &= -\frac{p\pi}{l}\frac{ma^2}{x_{mn}^2 r} E_0 J_m(k_{mn} r)\sin m\theta \sin\frac{p\pi z}{l} e^{j\omega t},\\
B_z &= 0,\\
B_r &= -j\omega\frac{ma^2}{x_{mn}^2 r c^2} E_0 J_m(k_{mn} r)\sin m\theta \cos\frac{p\pi z}{l} e^{j\omega t},\\
B_\theta &= -j\omega\frac{a}{x_{mn} c^2} E_0 J'_m(k_{mn} r)\cos m\theta \cos\frac{p\pi z}{l} e^{j\omega t}.
\end{aligned}
$$

The nomenclature of TM_{mnp} modes is defined as follows. The $m(n = 0, 1, 2, ...)$ index is the number of full period variations in θ of the field components. The $n(n = 1, 2, 3, ...)$ index is the number of zeros in the axial field component in the radial direction from the centre of the cavity to the wall excluding the centre itself. The final index $p(n = 0, 1, 2, ...)$ is the number of half period variations in the z direction. In a pillbox cavity, the lowest frequency TM mode is the TM_{010} whose frequency ω_{010} is defined only by the cavity radius and is independent of the cavity length. Figure 2.3 shows the electric and magnetic fields in a longitudinal and transverse cross-section respectively.
In order to accelerate, E_z must not vanish on the beam axis assuming the beam axis matches the cavity axis. Thus, modes of type TM_{0np} are used for acceleration and are know as monopole modes due to their rotational symmetry. Dipole modes ($m = 1$) are usually problematic in accelerating cavities due

to their net deflecting field on axis. Modes with $m = 2$ are called quadrupole modes. The electric field for a selection of monopole, dipole and quadrupole modes are shown in Figure 2.4. The typical accelerating mode for an rf cavity is TM_{010}. Modes other than the fundamental accelerating mode are known as Higher Order Modes (HOMs).

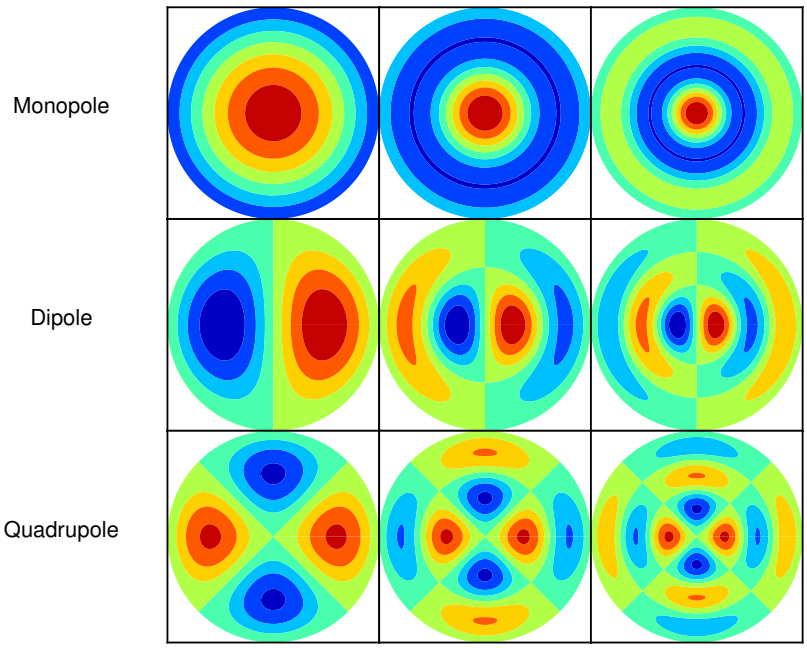

Figure 2.4: E_z for TM type modes with $m = 0, 1, 2$ in the vertical direction and $n = 1, 2, 3$ in the horizontal direction.

In order to accelerate a beam, there must be openings in the pillbox to allow the beam to enter and exit the cavity. The addition of this opening modifies the field properties and makes analytical studies much more difficult and numerical methods are needed. This means the modes are now TM-like and TE-like and there exists no exact TM_{mnp}, TE_{mnp} modes anymore.

2.2.4 Coaxial Resonator

A coaxial line is formed using a inner conductor of radius a surrounded by an outer conductor of radius b. A coaxial resonator is formed by adding end walls to the coaxial line. When the length of the resonator is a integer multiple of half-wavelengths, transverse electromagnetic (TEM) resonant modes exist. For a TEM mode, the electric and magnetic field have only transverse components and no longitudinal components. A resonance exists when $E_r = 0$ occurs at the end caps and occurs when the walls are separated by a distance $l = p\lambda/2, p = 1, 2, 3, ...$ The lowest mode occurs when $p = 1$, the half-wave resonator. The electric field for a half-wave resonator is shown in Figure 2.5.

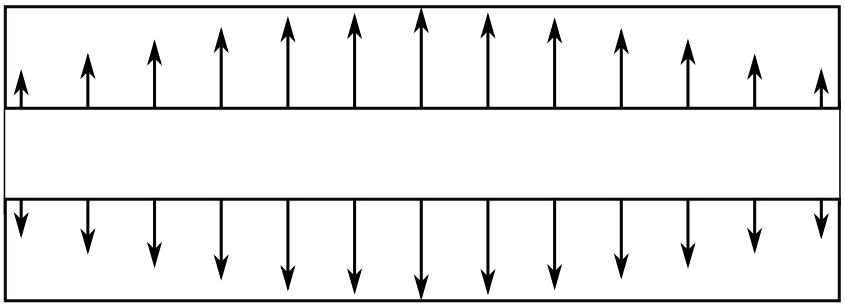

Figure 2.5: The electric field profile for a coaxial resonator.

The half-wave resonator shown can be modified to allow acceleration by adding beam holes to the inner and outer conductor at the point where the electric field is maximum, at $z = l/2$. The injection phase is chosen such that the electric field changes sign while the beam travels across the the inner conductor such that the beam is accelerated on both sides of the inner conductor. The radii of the inner and outer conductor are usually chosen to maximise the energy gain on each side.

2.2.5 Superconducting rf Cavities

The superconducting section of the ESS linac is the main focus of this thesis. This section is comprised of two types of cavities, elliptical cavities and spoke cavities. Superconducting cavities are chosen because of the low surface power-loss which is many orders of magnitude smaller than in normal conducting structures. The associated drawback from this along with the added complexity and cost of running a large cryosystem is that all the other electromagnetic modes have lower losses as well, resulting in long decay times.

Currently, the most common material used to manufacture cavities is niobium. Niobium is a Type II superconductor which has a critical temperature $T_c = 9.2\ K$. Above this temperature, superconductivity is lost and can also be lost if the surface magnetic field exceeds a critical field strength.

Different types of cavities are needed due to the quasi-relativistic nature of the beam. The beam will take a finite time to traverse the cavity, thus at different velocities, the beam will take different amounts of time to pass through the cavity resulting in different coupling to the accelerating mode. Each cavity type will be efficient at accelerating in a particular velocity range and therefore, different types are required.

2.2.6 Elliptical Cavities

Elliptical cavities [26] are named as such due to their cell shape which is defined by two ellipses joined by a common tangent. An elliptical shape is chosen to reduce the risk of multipacting and field emission which can result in local surface heating and possibly lead to a quench. Multipacting and field emission will be discussed in more detail in Chapter 5. A spherical shape could also be used however the elliptical shape is much more stable for mechanical reasons.

In order to achieve maximum acceleration, the cavity cell length is set such that the time it takes for a particle with constant velocity $v = \beta c$ to pass through the cavity is equal to half an RF period.

$$l = \frac{\beta c \pi}{\omega} = \frac{\beta c}{2f} = \frac{\beta \lambda}{2}, \tag{2.31}$$

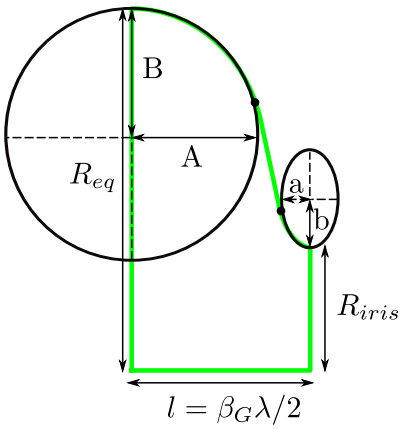

Figure 2.6: A schematic of an elliptical cavity half cell and the associated parameters which are used to define the shape.

where ω is the angular frequency of the accelerating mode. For the acceleration of electrons, $\beta \sim 1$ however for proton linacs, this is typically not the case. It is impractical to design a cavity for every beta possible, so a cavity is designed to accelerate particles in a certain β range. The cavity length is defined by the geometric beta β_G.

2.2.6.1 Multicell Cavities

In order to improve the accelerating efficiency, multi-cell cavities are used in linacs. By adding more cells, the ratio between the active accelerating length to total length improves. Multi-cell structures can also be powered using one coupler rather than needing a coupler for every cell. However, multi-cell structures also have drawbacks, they are more difficult to fabricate, increase the possibility of trapped modes as well as decrease the velocity acceptance.

For a multi-cell cavity, each cell may be considered as a resonant cavity which is weakly coupled to neighbouring cells. Therefore, the system is well described by a coupled oscillators model which predicts that each mode will split into a passband of modes with different resonant frequencies. Each mode inside this passband is distinguished by a phase advance, which for $N+1$ cells

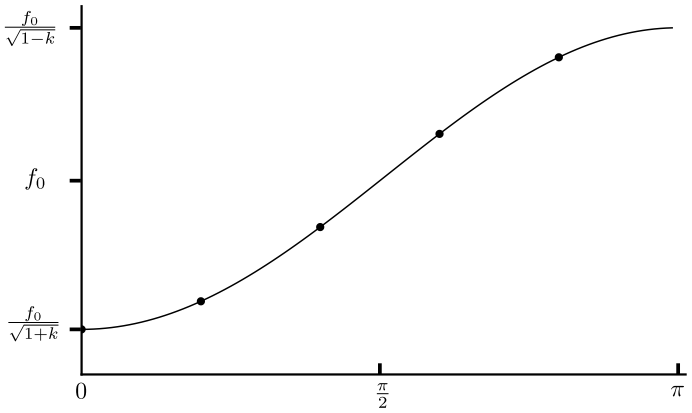

Figure 2.7: Dispersion plot for a five cell cavity where each mode is described by a point. The curve represents the passband for an cavity with infinite cells.

will result in $N+1$ modes with a phase difference $i.\pi/N$, where i is an integer running from 0 to N. Each mode may be plotted on a dispersion diagram as shown in Figure 2.7 as described by the dispersion relation for an electrically coupled cavity,

$$f_n = \frac{f_0}{\sqrt{1 + k_{cc}\cos(n\pi/N)}}, \tag{2.32}$$

where n is the mode out of N modes, f_0 is the frequency of the mode in the centre of the dispersion plot and has the same frequency as an uncoupled single cell. k_{cc} is the cell to cell coupling. For an accelerating cavity, the coupling effect of the beam pipes also needs to be taken into account, thus the ends cells have a different resonant frequency compared to the centre cells. This is necessary in order to achieve a flat field profile i.e. the same field profile in all cells. Modes in the same passband are of the same order but have a differing phase advance and thus, are know as Same Order Modes (SOMs). In this thesis, SOMs will refer to modes in the same passband as the fundamental accelerating mode.

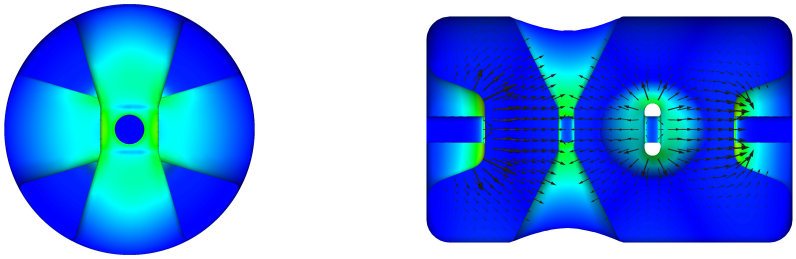

Figure 2.8: A transverse (left) and longitudinal (right) slice through a double spoke cavity. The on axis electric field distribution is shown on the longitudinal slice.

2.2.7 Spoke Cavities

Spoke cavities [27–29] are an interesting variant of the TEM resonator. They consist of n stacked half-wave cavities in which the inner conductor (spoke) is rotated by 90° from gap to gap. Figure 2.8 shows the transverse and longitudinal slice of a double spoke cavity. For a multi-spoke cavity, there also exist passbands however because the spoke cavity is a TEM resonator, the number of modes is defined by the number of conductors rather than the number of gaps as in a TM cavity. Thus, for a double spoke cavity, the fundamental passband will contain two modes, the 0-mode and the π-mode. The coupling take place chiefly using the magnetic field as opposed to elliptical cavities where the coupling is electric. The coupling is much stronger (20-30%) resulting in robust structures with field profiles insensitive to mechanical tolerances. As a result of the magnetic coupling, it also means the first mode is the accelerating mode. Although many prototypes have been developed for spoke cavities, they have yet to be tested in an operating machine. Is it expected that ESS will be the first operating machine to use spoke cavities. An interesting subtype of a spoke cavity is the crossbar H-mode cavity (CH) [30] which is also being developed for proton and ion accelerators.

2.2.8 RF Cavity Parameters

In the following subsections, important figures of merit for rf cavities are introduced, followed by the concept of power coupling and HOM damping.

2.2.8.1 Accelerating Voltage

Consider a particle traveling with velocity $v = \beta c$, charge q traversing a cell containing an on-axis electric field. At t=0, the phase of the field relative to the crest is ϕ. The energy gain of the particle travelling through the cell on axis is

$$\Delta W = q \int_{-\infty}^{\infty} E_z \cos[\frac{\omega z}{\beta c} + \phi] \mathrm{d}z, \tag{2.33}$$

which using a common trigonometric identity, can be rewritten as

$$\Delta W = q \int_{-\infty}^{\infty} E_z [\cos(\omega z/\beta c)\cos\phi - \sin(\omega z/\beta c)\sin\phi] \mathrm{d}z. \tag{2.34}$$

The integral runs from $-\infty$ to ∞ to take into account any fields that leak out of the cavity. If the field is symmetric around origin which is set to the mid-plane of the cell, the sin terms disappear. Typically, the energy gain is written as

$$\Delta W = q V_0 T(\beta)\cos(\phi), \tag{2.35}$$

where the axial rf voltage is defined as

$$V_0 = \int_{-L/2}^{L/2} E_z \mathrm{d}z, \tag{2.36}$$

and the velocity-dependent transit time factor $T(\beta)$ is define as

$$T(\beta) = \frac{\left| \int_{-L/2}^{L/2} E_z e^{j\omega z/\beta c} dz \right|}{\int_{-L/2}^{L/2} E_z \mathrm{d}z}. \tag{2.37}$$

The transit time factor accounts for the energy gain reduction due to the fact the particle takes a finite time to traverse the cell. It is especially important in proton linacs which accelerate particles over a large velocity range.

The effective accelerating voltage taking into account the synchronous phase is

$$V_{acc} = V_0 T(\beta)\cos(\phi). \tag{2.38}$$

The accelerating gradient is defined as

$$E_{acc}(\beta) = E_0 T(\beta), \tag{2.39}$$

where $E_0 = V_0/l$ is the average accelerating gradient.

2.2.8.2 Quality Factor

An important figure of merit for cavities, is the unloaded quality factor Q_0 which relates the stored energy U_0 in a particular mode to the power dissipation P_{diss} in the surface.

$$Q_0 = \frac{\omega_0 U}{P_{diss}}. \tag{2.40}$$

The Q_0 is approximately $1/e^{2\pi}$ times the number of rf cycles it takes to dissipate the energy stored in the cavity. The stored energy is found by integrating the electric field squared over the volume of the cavity. Given that the time averaged energy in the electric field equals that in the magnetic field, the stored energy is

$$U = \frac{1}{2}\mu_0 \int_V |\vec{H}|^2 \mathrm{d}v = \frac{1}{2}\mu_0 \int_V |\vec{E}|^2 \mathrm{d}v. \tag{2.41}$$

The power dissipated in the walls is caused by surface resistance and is given by

$$P_{diss} = \frac{1}{2} R_s \int_S |\vec{H}|^2 \mathrm{d}s, \tag{2.42}$$

where the integral is performed over the surface of the cavity. The Q_0 is

$$Q_0 = \frac{\omega_0 \mu_0 \int_V |\vec{H}|^2 \mathrm{d}v}{R_s \int_S |\vec{H}|^2 \mathrm{d}s}. \tag{2.43}$$

For superconducting cavities, R_s is very small. However, power is not only dissipated in the walls but can also be dissipated into an external load via a coupler. The external quality factor Q_{ext} is then defined as

$$Q_{ext} = \frac{\omega_0 U}{P_{ext}}, \tag{2.44}$$

where P_{ext} is the dissipated power in all external devices. A loaded quality factor Q_L can be defined as

$$Q_L = \frac{\omega_0 U}{P_{tot}}, \tag{2.45}$$

where P_{tot} is the total power dissipated and using energy conservation is given by$P_{tot} = P_{diss} + P_{ext}$. The loaded quality factor is inverse sum of all the subsystems and defined as

$$\frac{1}{Q_L} = \frac{1}{Q_0} + \frac{1}{Q_{ext}}. \tag{2.46}$$

2.2.8.3 Shunt Impedance

The shunt impedance provides an efficiency of the accelerating voltage for given dissipation

$$r_s = \frac{V^2}{P_c}. \tag{2.47}$$

A more useful expression is the so-called 'R-over-Q'

$$(R/Q) = \frac{r_s}{Q_0} = \frac{V_{acc}^2}{\omega U}, \tag{2.48}$$

which provides a measure of the energy exchange between the beam and a cavity mode. This quantity is particularly useful because it is independent of the surface resistance and only depends on the cavity geometry. Therefore, the R/Q is commonly used to characterise SRF cavities. Its value depends on

the velocity of the particle due to the transit time factor dependence with V_{acc}. When designing a cavity, one goal is to maximise the (R/Q) for the geometric beta of the cavity.

2.2.8.4 Power Couplers

The rf power from the generator is transferred to the cavity using an input coupler, which is also known as the fundamental power coupler (FPC) [31,32]. The FPC is also required to provide a match between the impedance of the generator and the combined impedance of the cavity-beam system, minimising the reflected rf power.

The FPC can either be of the coaxial or waveguide variety. The coaxial type is advantageous when the frequency small as it provides a more compact design or if a variable coupler is required, as the penetration depth of the probe can be varied. The waveguide coupler becomes more attractive as the frequency increases because of the decreasing dimensions. The waveguide coupler is also easier to cool as only the outer wall requires cooling.

The Q_{ext} of the FPC is typically several orders of magnitude smaller than the Q_0. The FPC also has the ability to couple to other modes and in turn reduce the Q_{ext} of these modes. However, this coupling is optimised for the accelerating mode only and thus, a dedicated device may be needed to provide damping of HOMs.

2.2.8.5 Higher Order Mode Damping

HOM damping [33] is required to remove beam-induced power which could provide concern for cryogenics and to damp dangerous modes which could cause energy spread and beam blow-up. Modes which have a high R/Q are usually thought to be a concern.

In order to provide sufficient damping to HOMs, such that they do not disturb the beam, couplers are installed on cavities. It is preferable to attach the couplers to the end tube, outside the end cells to avoid disturbing the cell geometries.

In most cases, it is desirable to have two couplers in order to adequately damp both polarisations of multipole modes. Dipoles are of most concern with quadrupole modes and other higher order multipole modes having much smaller R/Q.

There are three main varieties of HOM couplers: waveguide, coaxial and beam tube.

Waveguide Waveguide couplers allow the electric field of the HOM to couple to the field in the waveguide propagating in the TE_{01} mode. The cut-off frequency of the waveguide provides a simple method to reject the fundamental mode however the waveguide itself is quite bulky and adds extra structure cost.

Coaxial Coaxial couplers are compact and preferred for low frequency cavities. An antenna coupler can be used to coupler to the electric field or a loop can be used at the end of the antenna to couple to the magnetic field. Inductive and capacitive elements which are part of the coupler body provide damping at the desired frequencies and also suppress coupling to the accelerating mode via a rejection filter.

Beam tube The cavity beam pipe can be considered as a transmission line to coupler out HOMs with frequencies above the beam pipe cut-off. The accelerating mode is below cut-off and does not propagate out. A section of the beam pipe is line with microwave absorbing material such as Ferrite absorber to act as a load. Beam pipe couplers are particular advantageous for high current machines where several kilowatts of HOM power are dissipated.

2.2.8.6 Tuners

Frequency tuners [34, 35] play an important part in rf cavities. There exists a slow tuner and a fast tuner. Slow tuners bring the cavity resonance to the operating frequency, adjusting for changes in the cavity geometry due to cool-down or evacuation. It is required that slow tuners have a wide tuning range with the ability to shift the frequency by several hundred kHz as well provide

a resolution on the order of kHz. Fast tuners provide a much smaller tuner range compensating for effects due to Lorentz detuning. Lorentz detuning is the shift in frequency caused by strong Lorentz forces acting on the cavity walls due to the high electromagnetic fields.

Chapter 3

Electromagnetic Simulations of SCRF Cavities

This chapter will begin by introducing methods to simulate accelerating cavities, a more complete guide to electromagnetic simulations can be found in [36, 37]. These methods are then applied to cavity designs and dangerous modes are highlighted. The end of the chapter will focus on an issue related to cavity design as to whether a taper is need on the beam pipe. Large scale simulation methods are applied to determine if a taper is necessary.

3.1 Simulation Methods

In order to calculate the eigenmodes and field distributions inside an accelerating cavity, Maxwell's equations can be solved either analytically or numerically. Solving analytically provides exact solutions however this becomes difficult for problems involving complex geometries and inhomogeneous domains. To overcome this, numerical methods are employed but these also suffer from problems relating to convergence and accuracy.

A classical-boundary value problem as shown in Figure 3.1 can be described by the operator equation:

$$L(u) = s, \tag{3.1}$$

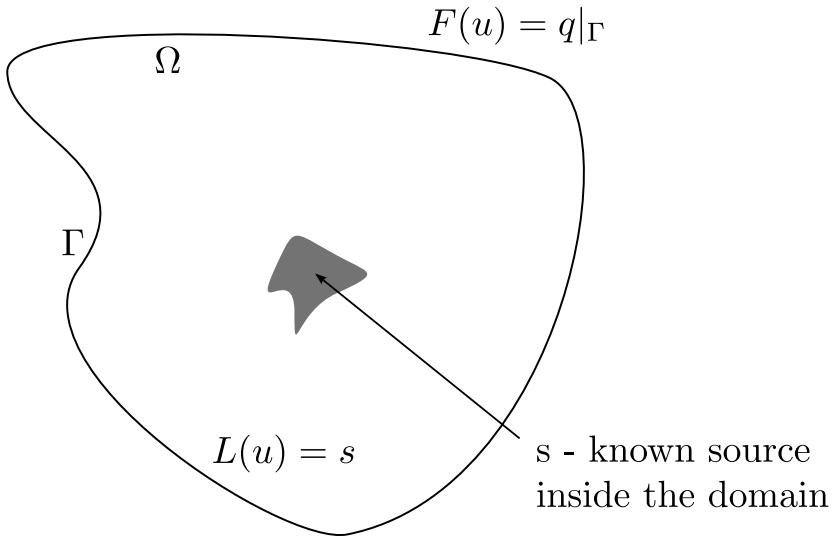

Figure 3.1: Classical-boundary value problem to be solved using the differential approach.

on the domain Ω and satisfies the boundary condition that $F(u) = q|_\Gamma$ where L is the differential operator, u is the unknown solution which is to be found, such as the fields inside a cavity and s represents the known sources inside the domain for example the charge in a cavity. Possible numerical methods used to solve this problem include the Finite Difference Method (FDM) and Finite Element Method (FEM) which will be discussed further in the next section.

3.1.1 Finite Difference Method

The finite difference method works by replacing a differential equation with a finite difference equation whereby the derivative of a function is replaced by a finite difference.

For a function $f(x)$, the derivative at x_0 is given by

$$f'(x_0) = \lim_{x \to x_0} \frac{f(x) - f(x_0)}{x - x_0}. \tag{3.2}$$

For a numerical simulation, x may not be known continuously but only at discrete points and so the derivative is approximated using three possible

schemes

- Forward difference approximation

$$f'(x_0) = \lim_{\Delta x \to 0} \frac{f(x_0 + \Delta x) - f(x_0)}{\Delta x} \approx \frac{f(x_0 + \Delta x) - f(x_0)}{\Delta x}. \tag{3.3}$$

- Backward difference approximation

$$f'(x_0) = \lim_{\Delta x \to 0} \frac{f(x_0) - f(x_0 - \Delta x)}{\Delta x} \approx \frac{f(x_0) - f(x_0 - \Delta x)}{\Delta x}. \tag{3.4}$$

- Central difference approximation

$$f'(x_0) = \lim_{\Delta x \to 0} \frac{f(x_0 + \Delta x) - f(x_0 - \Delta x)}{2\Delta x} \approx \frac{f(x_0 + \Delta x) - f(x_0 - \Delta x)}{2\Delta x}. \tag{3.5}$$

These approximations arise from the Taylor series representation of $f(x)$:

$$f(x_0 \pm \Delta x) = f(x_0) \pm \Delta x \frac{df}{dx}\bigg|_{x_0} + \frac{(\Delta x)^2}{2} \frac{d^2 f}{dx^2}\bigg|_{x_0} \pm \frac{(\Delta x)^3}{3!} \frac{d^3 f}{dx^3}\bigg|_{x_0} + \cdots \tag{3.6}$$

The approximation error is related to the number of terms neglected from the Taylor series. In the case of the forward and backward difference approximations, the error is of the order Δx, while for the central difference approximation, is of the order Δx^2. In the case of electromagnetic simulations, knowledge of the second derivative is required. Following a similar procedure to determining the first derivative, the second order differential operator is found to be

$$f''(x_0) \approx \frac{f(x_0 + \Delta x) - 2f(x_0) + f(x_0 - \Delta x)}{(\Delta x)^2} \tag{3.7}$$

With the first and second order derivative known, the wave equation can be solved at discrete mesh points. This method is one of the simplest numerical methods however, suffers from a poor convergence rate and thus, a large number of mesh points are required to get a good approximation.

3.1.2 Finite Element Method

An alternative method is to discretise the calculation domain into small elements known as finite elements.The unknown solution of this element is then expressed as a linear sum of local interpolation functions i.e. a sum of functions that provide the best fit to the data. These are known as the expansion basis. The approximate solution to the problem can then be expressed as

$$\bar{f} = \sum_{i=1}^{n} \alpha_i N_i, \tag{3.8}$$

where n is the total number of nodes, α_i is the solution at the nodes and N_i represents the expansion basis. In order to solve 3.1, one can integrate along the calculation domain using the weighted residual approach, in which the average residual is forced to zero, resulting in

$$\int_a^b L(u)w(x)\mathrm{d}x = \int_a^b sw(x)\mathrm{d}x \tag{3.9}$$

where the choice is weight function $w(x)$ defines the scheme. In the case of the Galerkin FEM, the weight function $w(x)$ is the same as the basic function $N_i(x)$. In this case, the system can represented by an eigenvalue problem using sparse matrices.

For the case of Maxwell's equations in a source free region (s = 0), u may correspond to the electric field vector $\vec{E}$ inside the region resulting in the operator equation

$$\nabla \times (\frac{1}{\mu}\nabla \times \vec{E}) - k^2\epsilon\vec{E} = 0. \tag{3.10}$$

3.1.3 Mesh Types

In order to solve the problem numerically, the model must be discretised. This done by creating a collection of vertices, edges and faces to define the object which is called a mesh. A mesh is typically defined by the shape of the faces. For a two dimensional problem, the shapes are usually rectangles or triangles. For a three dimensional problem, these are replaced by hexahedral

and tetrahedral elements respectively. The standard tetrahedral element is defined by four points where each point is a vertex, however there also exists a ten point tetrahedral where the midpoint of each edge is also defined along with the vertices. In this case, each edge is defined by three points which allows the possibility of curved tetrahedral elements which can provide a better approximation to curved surfaces. Figure 3.2 shows a four point tetrahedral element and ten point tetrahedral element overlaid on the original element.

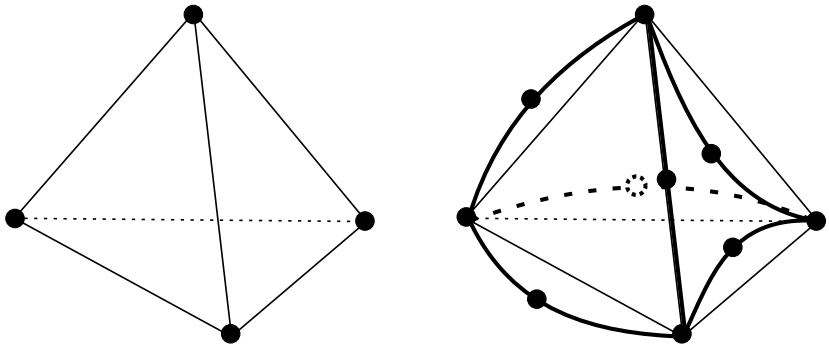

Figure 3.2: Four point tetrahedral element and ten point curvilinear tetrahedral element.

Meshes are can be either structured or unstructured. Structured meshes have regular connectivity between elements and provide greater speed however, unstructured meshes which have irregular connectivity allow the possibility of adaptive meshing where complex regions of the geometry can have a finer mesh.

3.1.4 Boundary Conditions

In addition to defining the geometry of the structures to be simulated, it is equally important to define boundary conditions. The two most important boundary conditions are the electric and magnetic boundary condition. The electric boundary condition forces the electric field to be perpendicular

($E_t = 0$) to the boundary and the magnetic field to be parallel ($n \cdot \vec{H} = 0$) to the boundary. The electric boundary condition acts as a metallic surface and so, is useful for defining walls of a cavity. The magnetic boundary condition forces the electric field to be parallel to the surface ($n \cdot \vec{E} = 0$) and the magnetic field to be perpendicular to the surface ($H_t = 0$). Figure 3.3 shows the electric field distribution in a cavity where the vertical wall has a magnetic boundary condition and the horizontal wall has electric boundary condition. Each boundary condition can be used as symmetry plane where the electric or magnetic field lines are mirrored at the boundary. This allows the possibility to reduce the simulation effort significantly by dividing the volume along the lines of symmetry, and only simulating a fraction of the volume as the simulation scale does not scale linearly with the number of mesh elements. magnetic boundary conditions can also be used to confine multipole modes to one polarisation. If the structure has axial symmetry, it makes little sense to find both polarisations as the symmetry is already forced. Adding a magnetic boundary condition forces the fields to be aligned with the wall. This also makes post-processing easier, as calculations requiring integration along the axis of maximum excitation can always performed along the wall.

Other boundary conditions are also used. Waveguide boundary conditions allow the possibility for power to leave the cavity via a particular port mode. The ability to properly model the cavity ports is important for determining parameters such as the external quality factor.

3.1.5 ACE3P

Simulations in this thesis are performed using the ACE3P (Advanced Computations Electromagnetics 3P) [38–41] code suite which is based on the higher-order finite element method and is written in C++. Curved ten-point tetrahedral elements are use to improve the accuracy of modelling complicated geometries. The codes were developed specifically to be capable of performing massively parallel computations which allow large and complicated accelerator structures to be simulated by a large number of CPUs.

ACE3P consists of six modules:

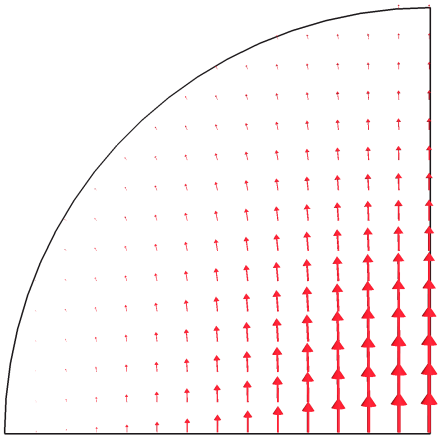

Figure 3.3: The electric field direction for electric and magnetic boundary conditons.

Omega3P Frequency domain solver for calculating cavity modes and damping. Typically used to optimise RF parameters, reduce peak surface fields, calculate HOM damping and find trapped modes.

S3P Calculate S-parameters in frequency domain for a particular system. Important when designing couplers to determine response to many frequencies not just resonances.

T3P Time domain solver for calculating transients and wakefields. A single or multiple driving bunches are used to evaluate broadband impedances or signal sensitivities.

Track3P Particle trackers for simulating multipacting in cavities and couplers by identifying multipacting barriers and sites.

Pic3P Particle in cell solver. Frequently used for calculating the beam emittance in RF gun designs.

TEM3P Thermal and mechanical solver.

ACE3P is based on the higher-order finite element method in which the computational domain is discretised into an unstructured mesh of quadratic elements and the electric field $\vec{E}$ is expanded into a set of tangentially continuous vector basis functions $N_i(x)$ up to order p within each element:

$$\vec{E} = \sum_{i=1}^{N_p} e_i \cdot \vec{\mathbf{N}}_i(x). \tag{3.11}$$

The use of higher order basis functions results in much faster convergence for fewer mesh elements. Figure 3.4 shows the frequency error between meshes of different density for a two cell cavity using different order solutions. For $p = 1$, 6 basis functions are used, the convergence is roughly linearly with number of elements. For $p = 2$, 20 basis functions are used and the convergence is quadratic with the number of elements. For $p = 3$, 45 basis functions are used and leads to a cubic relationship between frequency and the number of elements. The drawback of using higher order solutions is the higher number of basis functions leads to greater cpu and memory requirements. Typically, a compromise between order and the number of elements is made. In most cases, second order solutions are computed.
Using the above finite element discretisation and applying the required boundary conditions, the wave equation (3.10) becomes a generalised eigenvalue problem. For the the case of a lossless cavity:

$$\mathbf{Kx} = k^2\mathbf{Mx}, \tag{3.12}$$

where the matrices $\mathbf{K}$ and $\mathbf{M}$ are

$$\mathbf{K}_{ij} = \int_\Omega \left(\nabla \times \vec{\mathbf{N}}_i\right) \cdot \frac{1}{\mu} \left(\nabla \times \vec{\mathbf{N}}_j\right) \mathrm{d}\Omega, \tag{3.13}$$

$$\mathbf{M}_{ij} = \int_\Omega \vec{\mathbf{N}}_i \cdot \epsilon \vec{\mathbf{N}}_j \mathrm{d}\Omega. \tag{3.14}$$

The eigenvalue value can then be solved numerically and the electric field $\vec{\mathbf{E}}$ can be recovered using 3.11 and the magnetic field $\vec{\mathbf{B}}$ is calculated using

$$\vec{\mathbf{B}} = -jkc \sum_{i=1}^{N_p} x_i \nabla \times \vec{\mathbf{N}}_i. \tag{3.15}$$

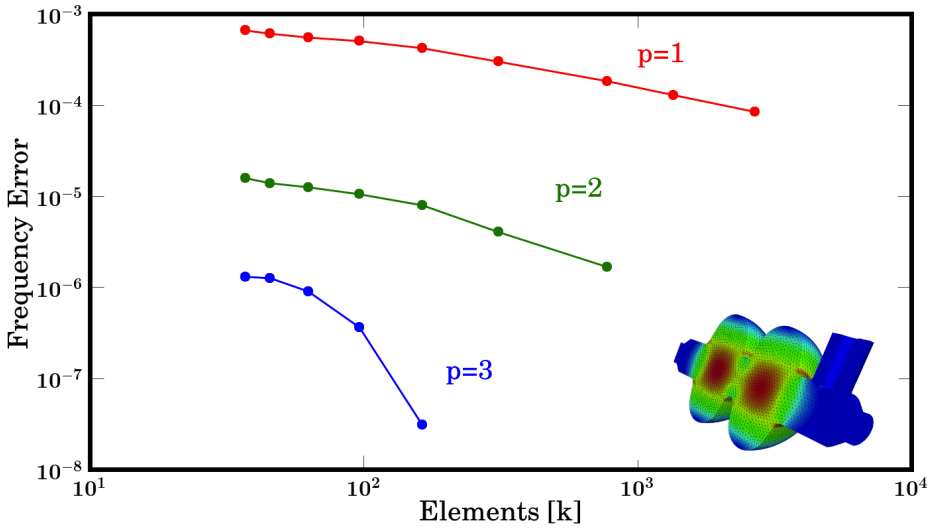

Figure 3.4: Frequency error for meshes as a function of element size with different number of basis functions.

3.1.6 NERSC

All ACE3P simulations were performed at the National Energy Research Scientific Computing Center (NERSC) [42] located in Berkeley, California. The Hopper Cray XE6 system was used which had 6384 computational nodes. Each node contains 2 twelve-core processors with access to 32GB of memory resulting in a total of 153,216 cores. Typically, most simulations performed only required 1-2 nodes however in some cases as many as 50 (1200 cpus) nodes were used.

3.2 ESS Cavities

This section will analyse the parasitic modes in each of the superconducting rf cavities for the ESS linac. Each cavity was modelled in 3D and then an

eigenmode simulation was performed on each using Omega3P, finding the first 100 modes. Care was taken to exclude simulations artefacts in post-processing which arise from the beam pipe boundaries in which non-physical boundary conditions are used. The whole machine can not be modelled, so either an electric or magnetic boundary condition is used at the beam pipe entrance and exit. The result means that in reality, less than 100 modes are studied.

The fundamental passband modes are analysed first, followed by the HOMs for each cavity. The cavity models will be used for the beam dynamics investigations in Chapter 4 but it should be noted they only represent prototype designs which are expected to change for the final machine. It is expected this will not have a huge impact on the beam dynamics investigations.

3D models of the cavities [43–45] are analysed for each family. Figure 3.5 shows a longitudinal slice of the mesh used for each cavity family with the electric field vectors for the accelerating mode. The FPC is omitted from the simulation as it expected to have a small impact on the mode distribution and in later beam dynamics investigations, the Q_{ext} is left as a free parameter and so, is not important to simulate. It is also possible for the coupler to result in kicks to the beam however, these are less important when the energy is higher as in the case for the ESS SRF linac. A magnetic symmetry plane was used in the y-plane in order to reduce the computation time as well confine multipole modes to one polarisation. The models used represent the ideal case with no imperfections, thus the cavities are forced to be symmetric and so the extra polarisations provide little information. It should be noted that by using a magnetic symmetry plane it prevents TE monopoles from being found however, this is not thought to be important because Panofsky-Wenzel theorem states there will be zero momentum impulse for a TE mode in the case where the fractional momentum change is small which applies here. Imperfections in the cavities are accounted for in the beam dynamics studies by applying a random spread to some of the parameters such as the mode frequency.

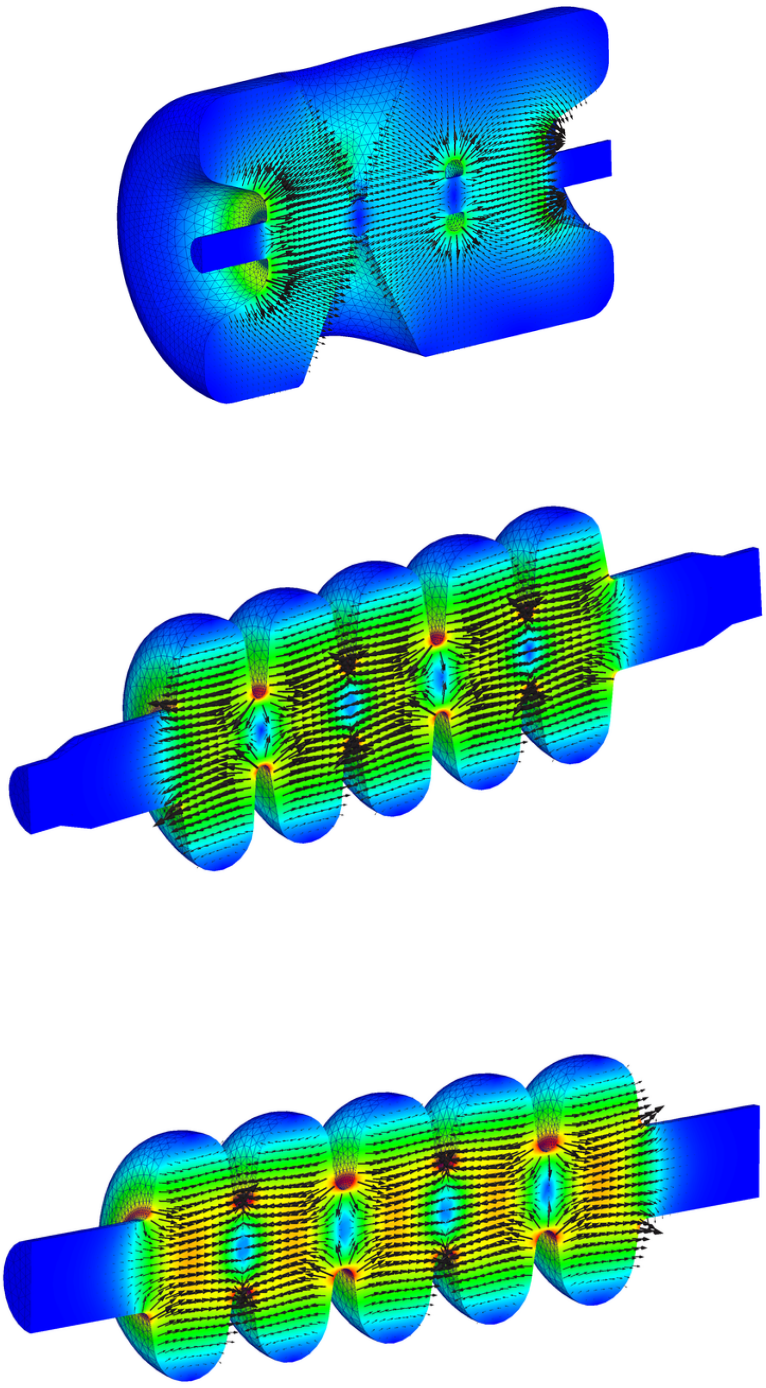

Figure 3.5: Slice of cavity family showing the field vectors for the accelerating mode.

3.2.1 Same Order Modes

The Same Order Modes (SOMs), modes that lie in the same passband as the fundamental accelerating mode are of particular interest due to their small frequency spread and high $R/Q(\beta)$ over the velocity range relative to the accelerating mode. For the spoke cavities, the number of modes in the passband is determined by the number of central conductors which for the ESS case, is two. For these studies, a third mode is also included even though it is strictly not a SOM, since it also has a high $R/Q(\beta)$ and is close in frequency to the accelerating mode.

For the elliptical cavities, the number of modes in the passband is determined by the number of cells and thus, there are four SOMs along with the accelerating mode which are considered. The centre frequencies of these modes, their distance from the accelerating mode, R/Q at the geometric beta of the cavity and maximum $R/Q(\beta)$ are shown in Table 3.1.

The dependancy of the $R/Q(\beta)$ as a function of the particles velocity is shown in Figure 3.6. It can be seen that at the beginning of the velocity ranges for the spoke and medium beta cavities, there are regions where the closest SOM to the accelerating mode has a higher $R/Q(\beta)$ than that of the accelerating mode. This raises concern that high voltages may build up, thus diminishing the quality of the beam. It is important to note that this plot could become misleading. The voltages that build up are also dependent on the frequency of the mode. Thus, the voltages in the spokes will be approximately and a factor of two smaller than in the elliptical cavities. This effect can be reduced by altering the velocity partitioning of the cavity families or altering the geometric beta of the cavities.

3.2.2 Higher Order Modes

In addition to the Same Order Modes, there is an infinite set of other modes that can exist inside the cavity which could also affect the beam. Of interest, are monopole modes which can cause acceleration or deceleration and also dipole modes, which can cause kicks in the transverse direction. The monopole and dipole modes with the highest R/Q summed over the velocity range are

Table 3.1: The $R/Q(\beta)$ evaluated at the geometric/optimum beta of the cavity and maximum $R/Q(\beta)$ for SOMs in each cavity family.

β_G	Mode	f_n [MHz]	$\lvert f_{SOM} - f_0 \rvert$ [MHz]	$R/Q(\beta_G)$ [Ω]	R/Q_{Max} [Ω]
0.5	TEM_0	351.986	0	428.43	428.43
0.5	TEM_π	362.697	10.711	2.88	134.16
0.5	TM_{010}	396.968	44.982	4.63	71.52
0.7	$\mathrm{TM}_{010,\pi/5}$	694.538	9.781	0.07	0.40
0.7	$\mathrm{TM}_{010,2\pi/5}$	697.256	7.063	0.12	1.51
0.7	$\mathrm{TM}_{010,3\pi/5}$	700.586	3.734	0.29	30.57
0.7	$\mathrm{TM}_{010,4\pi/5}$	703.255	1.064	1.55	101.01
0.7	$\mathrm{TM}_{010,\pi}$	704.320	0	313.73	363.18
0.86	$\mathrm{TM}_{010,\pi/5}$	693.191	11.226	0.02	0.11
0.86	$\mathrm{TM}_{010,2\pi/5}$	696.307	8.111	0.06	0.31
0.86	$\mathrm{TM}_{010,3\pi/5}$	700.145	4.272	0.18	5.33
0.86	$\mathrm{TM}_{010,4\pi/5}$	703.240	1.177	0.21	101.11
0.86	$\mathrm{TM}_{010,\pi}$	704.418	0	434.561	477.50

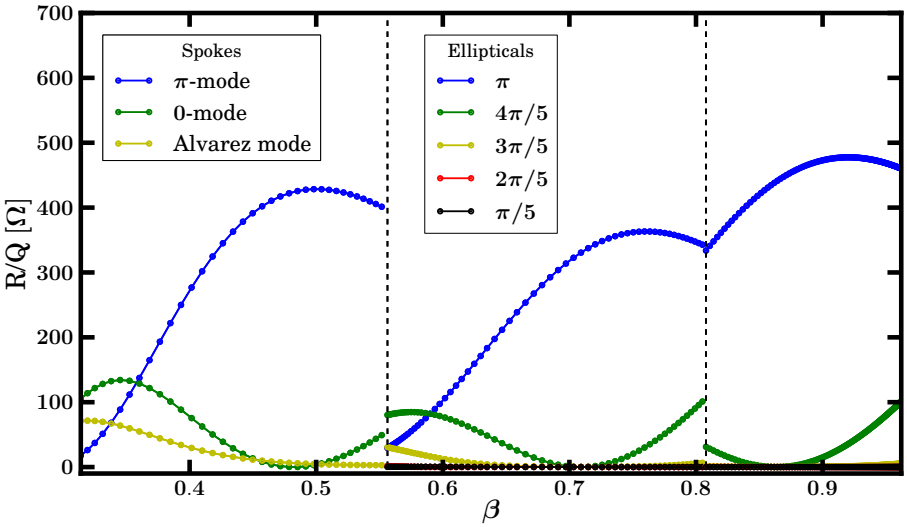

Figure 3.6: $R/Q(\beta)$ dependancy for the Same Order Modes in each cavity. The black dashed line represents the start of a new cavity family. All SOMs are shown however, for some modes the $R/Q(\beta)$ is so small it appears almost zero.

shown in Table 3.2 and Table 3.3. Each table shows the R/Q at the design beta of the cavity, the maximum R/Q and finally the sum of R/Q across the velocity range.

Also of interest, is the frequency of the HOM in relation to the machine lines which is defined as an integer multiple of the bunch repetition frequency, which for ESS is 352.21 MHz. In the case where a HOM lies precisely on such a machine line, the HOM is continually excited at the same phase leading to a resonance condition causing beam break up. Figure 3.7 shows the maximum R/Q of the first 100 modes for each cavity family where the dashed line represents the machine lines. The accelerating mode for the spoke and elliptical cavities can clearly be seen lying on the first and second machine line respectively.

Table 3.2: The $R/Q(\beta)$ evaluated the geometric/optimum beta of the cavity, the sum of R/Q of the velocity range and maximum $R/Q(\beta)$ for monopole modes.

β_G	f_n [GHz]	$R/Q(\beta_G)$ [Ω]	R/Q_{Max} [Ω]	$\sum R/Q$ [Ω]
0.5	0.563	6.44	20.98	267.28
0.5	0.864	3.79	5.13	88.58
0.5	1.038	1.56	3.50	50.28
0.5	0.628	0.25	5.18	40.97
0.5	1.104	1.22	1.75	28.01
0.7	1.6248	4.66	25.47	406.81
0.7	1.61733	6.50	6.51	165.69
0.7	1.60589	0.20	2.84	83.12
0.7	1.5814	0.19	5.68	80.42
0.7	1.58341	2.52	3.29	73.50
0.86	1.45605	40.99	61.26	5628.19
0.86	1.49157	6.35	13.67	982.72
0.86	1.44279	2.35	21.03	876.64
0.86	1.42069	0.98	14.58	667.00
0.86	1.42019	6.57	8.69	529.75

Table 3.3: The $R/Q_\perp$ evaluated the geometric/optimum beta of the cavity, the sum of $R/Q_\perp$ of the velocity range and maximum $R/Q_\perp$ for dipole modes.

β_G	f_n [GHz]	$R/Q_\perp(\beta_G)$ [Ω]	$R/Q_{\perp,Max}$ [Ω]	$\sum R/Q_\perp$ [Ω]
0.5	0.53628	56.5	57.80	1444.86
0.5	0.60548	23.24	31.46	549.90
0.5	0.75384	8.31	25.84	272.97
0.5	0.91971	5.63	11.66	145.10
0.5	0.67500	1.40	17.99	142.71
0.7	1.01157	39.90	66.26	1797.08
0.7	1.02094	36.88	37.37	1431.00
0.7	1.00475	16.30	76.78	1371.86
0.7	1.12154	0.01	20.90	569.37
0.7	1.03347	4.805	15.66	478.16
0.86	0.9836	40.25	98.04	7143.26
0.86	0.9819	67.57	67.57	6652.17
0.86	0.9942	3.39	51.65	2718.06
0.86	1.5145	16.85	25.80	2359.52
0.86	0.9426	30.82	30.82	2160.48

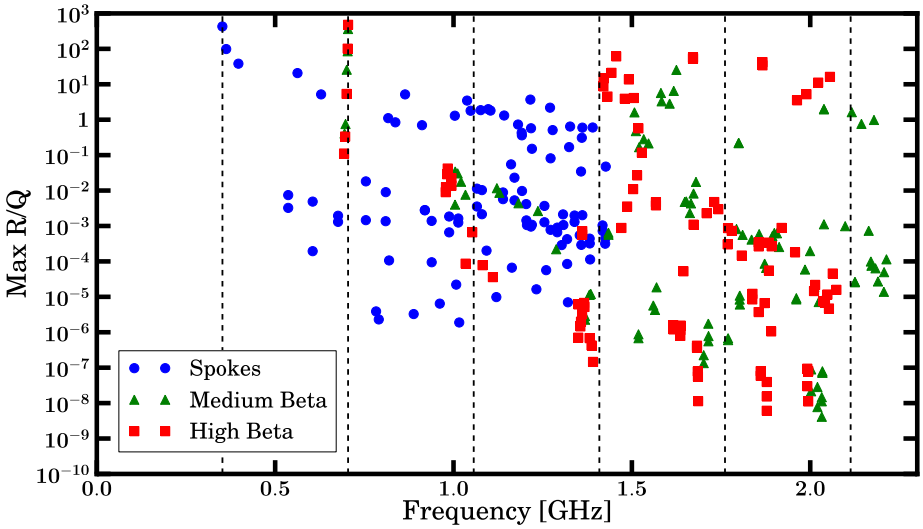

Figure 3.7: The maximum $R/Q(\beta)$ of the first 100 modes for each cavity family. The dashed line represent the machine lines which correspond to an integer multiple of the bunch repetition frequency of 352.21 MHz.

3.3 SPL Cavities

Proposed designs for the Superconducting Proton Linac (SPL) cavities are also simulated. The cavities are also made up of 5 cells and resonate at 704 MHz. The geometric beta of the cavity is slightly different to ESS however, this isn't expected to have a large effect on the simulations presented later. The SPL cavity design was used because at the time of studying the ESS designs were not available. The SPL cavity design will be used in Section 3.4 and also for the coupler studies in Chapter 5.

More information of the HOMs in the SPL cavities can be found in [46].

3.4 Cavity-to-cavity Coupling

One of the current cavity design issues is whether to include a taper in the interconnect region between two cavities. A taper has some proposed advantages such as its ability trap dark current and also to reduce the coupling of the fun-

damental mode to a neighbouring cavity. In order to investigate how efficient a taper is at reducing this coupling, the cavity-to-cavity coupling is investigated for different interconnect configurations. Simulations were performed on SPL cavity designs as previously stated.

3.4.1 Coupled Modes

For a single cavity, each cell may be considered as a resonant cavity which is weakly coupled to neighbouring cells. Therefore, the system is well described by a coupled oscillators model which predicts that each mode will split into a passband of modes with different resonant frequencies. Each mode inside this passband is distinguished by a phase advance, which for $N+1$ cells will result in $N+1$ modes with a phase difference $i.\pi/N$, where i is an integer running from 0 to N. Each mode may be plotted on a dispersion diagram as described by the dispersion relation,

$$\omega_\theta^2 = \omega_{\frac{\pi}{2}}^2 (1 - k\cos\theta), \tag{3.16}$$

where θ is the phase advance, $\omega_{\frac{\pi}{2}}$ is the frequency of the mode in the centre of the dispersion plot with a phase advance of $\pi/2$ and k is the coupling constant. Thus, the coupling is defined by the frequency spread of the modes and can represented by,

$$k = \frac{\omega_\pi^2 - \omega_0^2}{\omega_\pi^2 + \omega_0^2}. \tag{3.17}$$

It is useful to define the coupling in a terms of the frequency of the 'zero' and 'pi' mode as they have the lowest and highest frequency in a passband.

3.4.2 Coupled Cavities

For the case of cavities in a cryomodule, the interconnect region between the cavities has a cut-off frequency too high to allow the fundamental modes and other high R/Q modes to propagate. These modes decay exponentially as an evanescent field and may possibly couple to an adjacent cavity. An example cryomodule containing a string of four cavities is shown in Figure 3.8.

In a similar fashion to the previous section, cavities in a cryomodule may also be described by that of coupled oscillators where each cavity mode splits into a passband corresponding to the number of coupled cavities in the cryomodule. The coupling between these cavities can once again be described by (3.17).

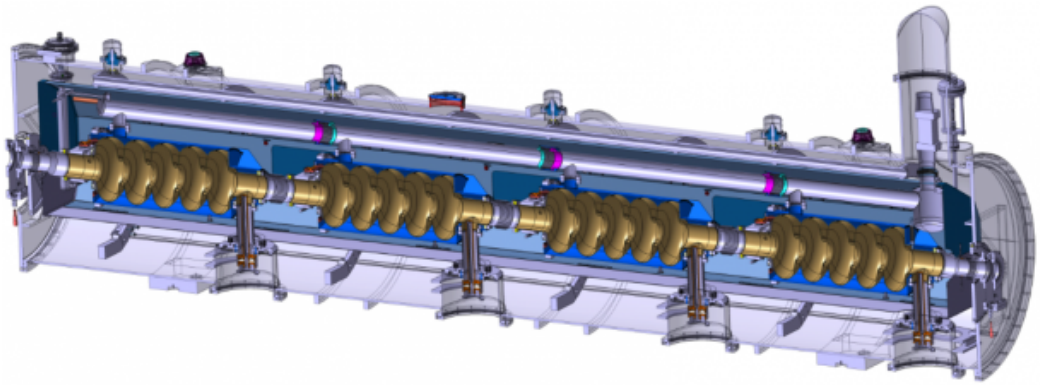

Figure 3.8: A cryomodule design for the ESS elliptical cavities.

3.4.3 Simulations

The simulations were performed on cryomodules containing only four cavities rather than eight to minimise the computing resources needed.

The mesh used for a four cavity cryomodule consisted of ∼1.5 million second order mesh points. The magnitude of the coupling between the cavities is expected to be relatively small compared to that of cell-to-cell coupling inside a cavity due to the much larger distance between the cavities compared to the cell-to-cell distance. Therefore, a very high number of mesh points are needed despite the second order nature of the mesh because the frequency separation will be much smaller and so a lower frequency error is required.

The interconnect regions will have the strongest effect on the coupling due to their small radius. The length and radius of the interconnect regions are shown in Table 3.4 along with the cut-off frequencies for the TM_{01} and TE_{11} modes.

Table 3.4: Interconnet region parameters.

Type	**Length**	**Radius**	**TM_{01} f_c**	**TE_{11} f_c**
	mm	cm	GHz	GHz
Nominal	60	40	2.87	2.19
Extended	120	40	2.87	2.19
Notaper	60	65	1.76	1.35

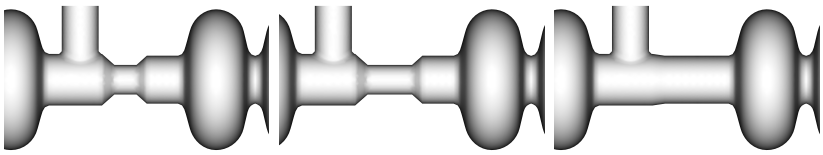

Figure 3.9: Cavity-to-cavity coupling for the nominal, extended and not tapered interconnect regions running from left to right.

The results of the simulations are shown in Figure 3.10. The coupling for the first monopole band appears to be largely unaffected by the different interconnects. This is probably because these are TM_{01} modes and are very far away from the cut-off frequency. There is a large difference between the notaper interconnect and the other two interconnects for the first two dipole bands (0.85-1.1 GHz). Although the taper reduces the coupling of the dipole modes, this is an unwanted effect if couplers are installed as it would reduce their efficiency.

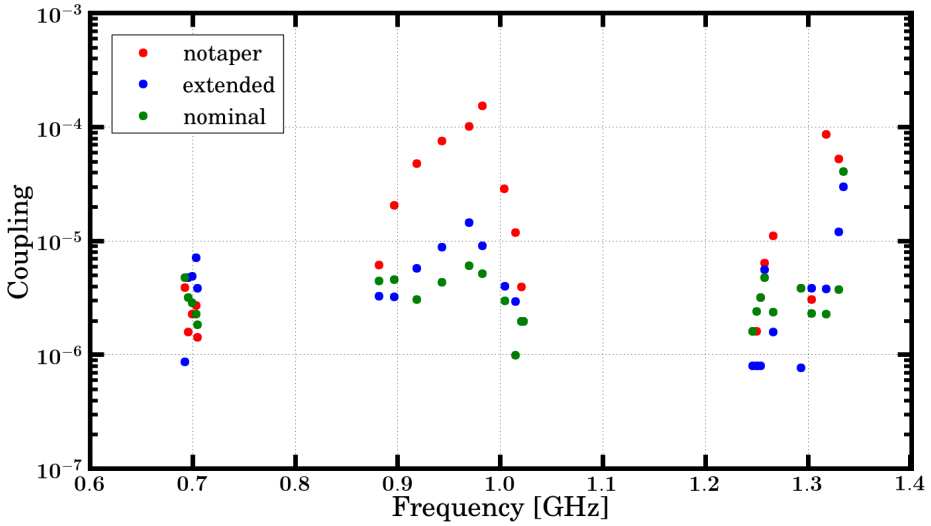

Figure 3.10: Cavity-to-cavity coupling for three interconnect regions.

Following from these simulations, the taper makes little effect to the coupling of the accelerating mode and thus, a taper at the interconnect region for cavities resonating at 704 MHz is not needed.

3.4.4 Theoretical Model

The coupling calculations shown in the previous section provide good accuracy however are very expensive in terms of computing resource given than one simulation requires $\sim$ 4000 CPU hours. A theoretical model has been developed in an attempt to provide a good approximation to the coupling using much less resources.

Inside the cavity, a particular mode will oscillate at its resonant frequency, however once this mode propagates into an interconnect region it will decay exponentially as an evanescent field away from the cavity. This formalism is mathematically identical to the situation of a Quantum Mechanical particle in a finite potential well. In the case of multiple finite wells, the energy levels of a system split when the wells become coupled which is analogous to coupled oscillator model as described earlier. Therefore, in order to predict the cavity-to-cavity coupling, each cavity was modelled as a potential well. From this,

a model was built based upon [47] which was originally used to calculate the eigenvalues for bound states of particles in multiple square well potentials.

Consider a single cavity. The mode oscillation in the cavity and in an interconnect can be described by a combination of right-going and left-going waves, as follows,

$$\psi_j(z) = A_j e^{(ik_j z)} + B_j e^{(-ik_j z)}, \tag{3.18}$$

where

$$k_j = \left[(p_{nm}/a)^2 - (\omega/c)^2\right]^{1/2}, \tag{3.19}$$

where the index j represents each region and p_{nm} is the m_{th} root of the n_{th} order Bessel function. When the mode frequency is below cut-off, k_j is complex resulting in a exponential decay. For a single cavity, there is one region for the cavity and two regions for the interconnect either side of the cavity. Across the three regions, both $\psi(z)$ and $\psi'(z)$ must be continuous, therefore at each boundary between two regions the following can be used

$${}^{j}M_j \begin{pmatrix} A_j \\ B_j \end{pmatrix} = {}^{j}\ M_{j+1} \begin{pmatrix} A_{j+1} \\ B_{j+1} \end{pmatrix}, \tag{3.20}$$

where

$${}^{m}M_j \equiv \begin{pmatrix} e^{ik_j z_m} & e^{-ik_j z_m} \\ ik_j e^{ik_j z_m} & -ik_j e^{-ik_j z_m} \end{pmatrix}. \tag{3.21}$$

The coordinate z_m represents the position of the interface between a cavity and an interconnect region. Therefore, for one cavity, using (3.20), two equations can be formed which can be used to find the resonant frequency depending on the boundary conditions used i.e. (A_0, B_0, A_2, B_2). If it is assumed that the mode is bound inside the cavity, B_0 can be set to zero to represent no outgoing wave and A_0 is set to one for simplicity. Using these initial conditions, to find the resonant frequency, one must find at what frequency there is no outgoing wave at the end of the system i.e. the roots of B_{2N}.

Using the following expression

$$\left(\prod_{2N-1}^{0} [({}^{j}M_{j+1})^{-1} * {}^{j}M_j]\right) \begin{pmatrix} A_0 \\ B_0 \end{pmatrix} = \begin{pmatrix} A_{2N} \\ B_{2N} \end{pmatrix}, \tag{3.22}$$

it is possible to compute the resonant frequencies for coupled cavities by setting $A_0 = 0, B_0 = 1$ and then search for the roots of B_{2N}. A comparison of this method against simulations explained earlier using Omega3P are shown in Figure 3.11 . The Omega3p results are shown for a $\beta_G = 0.65$ design [48] as the power coupler was omitted for this simulation. In order to set a well to resonate at the desired frequency before it is coupled, the following is used to set the length of the well

$$z_{cav} = \frac{2\tan^{-1}(\frac{k_1}{k_0})}{k_0}, \tag{3.23}$$

where k_0 is the defined in the region of the interconnect and k_1 is the region of cavity. The theoretical model shows good agreement to an order of magnitude with Omega3P up until $\sim$ 1.1GHz where the models begin to differ. This is probably due to the over simplistic nature of the theoretical model used in that each cavity is treated as just one well when it is more physical to treat each cell of a cavity as a well. In this model, the resonant frequency is defined by the well length due to its two dimensional nature however in reality, a cavity's frequency is determined by its transverse dimensions. In its current formalism, the model does not allow the introduction of power couplers or HOM couplers due to their complex nature.

3.4.5 Future Studies

The theoretical model gave a good order of magnitude approximation at low frequencies however, it still requires some modifications in order to improve its accuracy. Current ideas are to model each cell of a cavity as a potential well rather than just the whole cavity.

It may be possible to modify the code to incorporate more complex components in the future such as power couplers or HOM couplers however, as the complexity increases so will the computing time which becomes counter productive given that Omega3P can provide excellent accuracy with enough time.

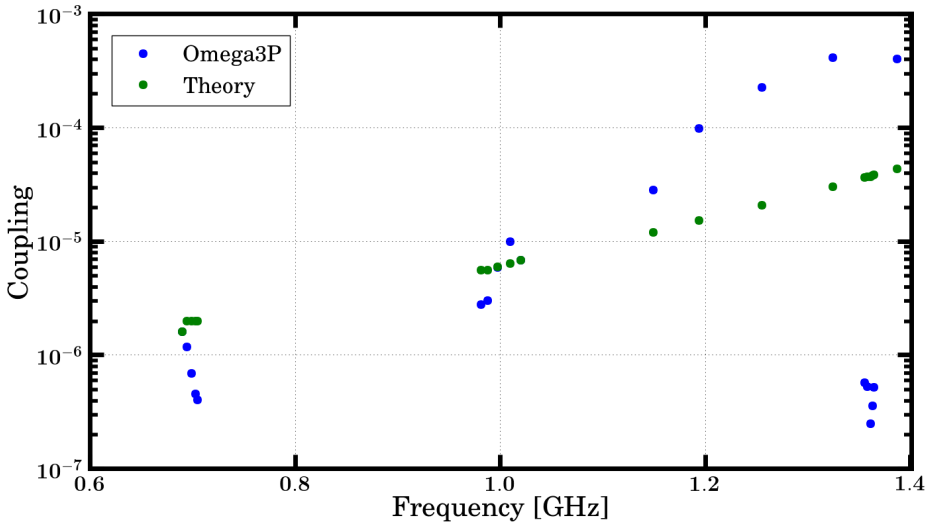

Figure 3.11: The cavity-to-cavity coupling as calculated from Omega3P and the theoretical model.

Chapter 4

Beam Dynamics Simulations including Parasitic Resonances

This chapter will use the simulation results from the previous chapter to calculate the effect of dangerous parasitic resonances on the beam dynamics for ESS. It will aim to determine if external damping is required and if so, to what degree. Experimental measurements of the shift of HOM frequencies due to cavity deformations will also be presented.

A bunch in a linac consist of a collections of particles which have approximately the same positions, phases and energies. The beam quality refers to the degree in which the particles have almost the same coordinates as the reference particle, a particle which travels with specified energy and phase.

Each particle can be described by three position and three momentum coordinates, giving a total of six coordinates. Thus, each particle can be described by a single point in six-dimensional phase space. The 6-D space can be analysed through two-dimensional phase plane projections in which each projection contains one position and one corresponding momentum component. Typically, they can be represented by ellipses, assuming zero coupling between places and linear forces acting. They area formed by the ellipse is called emittance. In reality, there are non-linear forces acting and such a RMS emittance, ϵ_r is used to estimate the area of the ellipse. For the case of the projection in the horizontal plane. The emittance is defined as

$$\epsilon_r = \pi\sqrt{\langle x^2\rangle\langle x'^2\rangle - \langle xx'\rangle^2}, \tag{4.1}$$

where x is the position and x' is the angular divergence. The angular divergence used as it is more convenient to use than the horizontal momentum. This chapter will treat bunches as points and thus, emittance will not be used however, a similar definition for the pulse space is used later on and an introduction to emittance proves useful.

4.1 Beam Physics

In an accelerator, the charge distribution in a bunch may be approximated by a gaussian with characteristic length σ_z along the direction of motion. The mode excitation by such a distribution can calculated by superimposing the voltages induced by the individual charges (dq) passing through the cavity at time t_q

$$dV = -dq\frac{\omega_n}{2}(R/Q)_n(\beta)e^{i\omega_n t_q}, \tag{4.2}$$

where ω_n is the angular frequency of mode n, β , is the velocity of the particle as a fraction of the speed of light and R/Q is given by

$$(R/Q)_n(\beta) = \frac{\left|\int_{-\infty}^{\infty} E_{z,n}(r=0,z)e^{i\omega_n\frac{z}{\beta c}}dz\right|^2}{\omega_n U_n}, \tag{4.3}$$

where U_n is the stored energy in the mode and $E_z(r=0,z)$ is the electric field along the beam axis. If the bunch is set to travel through the center of the cavity at $t=0$, the induced voltage can be written as

$$\Delta V = -\frac{\omega_n}{2}(R/Q)_n(\beta)\int e^{i\omega_n t_q}dq = -\frac{\omega_n}{2}(R/Q)_n(\beta)\int_{-\infty}^{+\infty} I(t)e^{i\omega_n t_q}dt, \tag{4.4}$$

where $I(t)$ is the current through the cavity as a function of time. In the case of a gaussian profile with a total charge q, the current is given by

$$I(t) = \frac{q}{\sqrt{2\pi}\sigma_t}e^{-t^2/2\sigma_t^2}, \tag{4.5}$$

where σ_t is the bunch length in time. Evaluating (4.4), the induced voltage becomes

$$\Delta V = -q\frac{\omega_n}{2}(R/Q)_n(\beta)e^{-\omega_n^2\sigma_t^2/2}. \tag{4.6}$$

It can be seen that in the case where $1/\sigma_t >> \omega_n$, the bunch can be treated as a point charge. In the case of ESS, the bunch length is very small compared to the considered HOM wavelength and thus, for the rest of this thesis, bunches are considered to be point-like.

Therefore, the voltage induced by a point-charge, q , according to the fundamental theorem of beam loading given by

$$\Delta V_{q,n} = -q\frac{\omega_n}{2}(R/Q)_n(\beta), \tag{4.7}$$

Due to losses, the amplitude of the voltage will decay according to

$$V_n(t) = \Delta V_{q,n}e^{-t/T_{d,n}}e^{i\omega_n t}, \tag{4.8}$$

where $T_{d,n} = 2Q_{L,n}/\omega_n$ is the voltage decay time constant with Q_L as the loaded quality factor of the complete system and is the reciprocal sum of all the subsystems

$$\frac{1}{Q_{L,n}} = \frac{1}{Q_{0,n}} + \frac{1}{Q_{ext,n}}. \tag{4.9}$$

For a superconducting cavity, the natural Q_0 is of the order of 10^{10} meaning that the Q_L is dominated by Q_{ext} and so the approximation that $Q_L \approx Q_{ext}$ is made.

In the case of dipole modes, only off-axis particles are of interest due to the non-existent field component along the axis. The dipole field present in a cavity will result in a deflection, which using Panofski-Wenzel theorem [49], can be written as

$$\Delta p_{\perp,n} = i\frac{q}{\omega_n}\frac{dV_{z,n}}{dx}. \tag{4.10}$$

The transverse voltage $V_\perp$ is defined by the relation

$$\Delta p_{\perp,n} = q\frac{V_{\perp,n}}{c}. \tag{4.11}$$

Using the fact that the voltage scales linearly with x, the transverse voltage can be written in terms of the voltage, $V_{\parallel,n}(x,\beta)$ induced by a point charge,q, traveling at a postion, x with velocity βc parallel to the beam axis.

$$V_{\perp,n} = i\frac{c}{\omega_n x}V_{\parallel,n}(x,\beta). \tag{4.12}$$

Similarly, a transverse $R/Q_{\perp,n}(\beta)$ can be introduced

$$R/Q_{\perp,n}(\beta) = \frac{|V_{\perp,n}|^2}{\omega_n U_n}. \tag{4.13}$$

Therefore, the transverse voltage induced by a charge, q, exciting a dipole mode with angular frequency, ω_n, in a cavity at position, x, is given by

$$\Delta V_{\perp} = \frac{1}{2}ixq\frac{\omega_n^2}{c}R/Q_{\perp,n}(\beta). \tag{4.14}$$

The fact that the induced voltage is imaginary shows that it is 90° out of phase with the particle and hence, there is no direct interaction between the voltage and the particle itself.

4.1.1 Monopole Interaction

As well as exciting all the modes in a cavity, the particle will also experience an energy change

$$\Delta U_n = q(\Re(V_n)\cos(\omega_n dt) - \Im(V_n)\sin(\omega_n dt)) - \frac{1}{2}\Delta V_{q,n}, \tag{4.15}$$

where $\Re(V_n)$ and $\Im(V_n)$ is the real and imaginary part of the HOM voltage already present in cavity prior to the arrival of the particle and taking into account the particle phase with respect to the HOMs. Half of the induced voltage $\Delta V_{q,n}$ will also act back on the bunch as determined from the fundamental theorem of beam loading [50].

4.1.2 RF Errors

The error in energy due to the rf is given by the difference between the actual energy gain of the particle and the energy gain on the synchronous particle.

$$\Delta U_{RF} = qV_{RF}^{*}\cos\left(\phi_s^{*} + \omega_{RF}dt\right) - qV_0\cos(\phi_s), \tag{4.16}$$

where V_{RF} represents the accelerating voltage including an amplitude error. ϕ_s^{*} is the operating phase of the cavity including some error from the klystron. $\omega_{RF}dt$ takes into account the time of arrival error. The second term shows the energy gain from ideal acceleration i.e. as seen by the synchronous particle.

4.1.3 Drift-kick-drift Model

The linac is modelled as a series of drifts and kicks at the cavity mid-plane [51, 52]. At each mid-plane the particle will interact with the cavity resulting in an acceleration kick as described by the previous sections. The size of the drifts is given by the actual distance between the cavity centres as defined by the lattice.

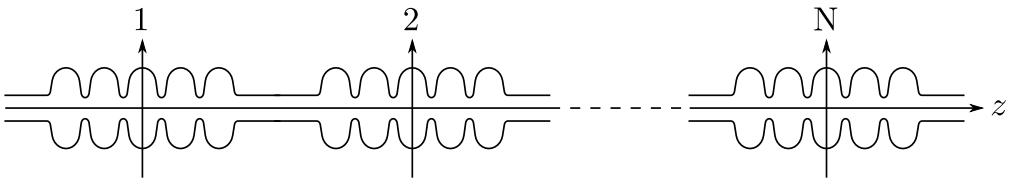

Figure 4.1: Drift-kick model.

The total energy error created by a charged particle passes through a cavity m is given by the summation of the energy errors developed by HOMs and the rf as well as the energy error $\Delta E^{(m)}$ already in front of the cavity.

$$\Delta E^{(m+1)} = \Delta E^{(m)} + \Delta U_{RF}^{(m)} + \Delta U_{n}^{(m)}. \tag{4.17}$$

This energy error will result in a time arrival error when passing through the drifts between cavities.

$$\Delta t^{(m+1)} = \Delta t^{(m)} + (dt/dE)_E \cdot \Delta E^{(m)}. \tag{4.18}$$

The gradient depends on the length of the drift, L, the mass m_0 of the particle and the relativistic γ of the particle.

$$(dt/dE) = -\frac{L^{(m)}}{c \cdot m_0 c^2 \cdot (\gamma^2 - 1)^{3/2}}. \tag{4.19}$$

Although the drift-kick-drift model is a simplified model, it is an accepted model for beam dynamics and provides an excellent approximation to the physics. More information can be found at [53].

4.1.4 Dipole Interaction

A complex voltage $V_\perp$ will yield a transverse momentum kick, as described by Panofsky-Wenzel theorem [49].

$$\Delta p_x = q\frac{\Re(V_\perp)}{c}. \tag{4.20}$$

This gives rise to a transverse trajectory change for small angles

$$\Delta x' = \Delta p_x / p_\parallel = q\frac{\Re(V_\perp)}{c p_\parallel}, \tag{4.21}$$

where $p_\parallel$ is the longitudinal momentum and $\Re(V_\perp)$ represents the real part of the voltage.

4.2 Beam Dynamics Code

In order to investigate the effects of parasitic resonances on the beam, a simulation code was developed based on the model presented in [51, 52]. The code was dedicated to the interaction between the resonances and beam itself with a special emphasis on the quasi-relativistic nature of the beam. Details of the code are discussed in the following section. A version of the code can be found at [54].

4.2.1 Concept

A train of point-like bunches are tracked through the linac calculating the energy and phase error generated, i.e. the deviation from the ideal case. At each cavity mid-plane, a kick is applied and from this, the energy error is determined. Due to the quasi-relativistic nature of the bunches, an energy error will result in a time of flight error as the bunch drifts to the next cavity mid-plane. The tracking is performed separately for the longitudinal and transverse plane as they are assumed to be uncoupled. The HOM voltage for every cavity is stored and modified in the presence of a bunch to account for the induced voltage. The voltage is then decayed ready for the next bunch.

4.2.2 Longitudinal

For a given linac design, the distance between cavities, the synchronous phase and the maximum effective accelerating voltage ($V_0T(\beta)$) are provided by TraceWin [55]. TraceWin is a code that can perform linear or nonlinear calculations in 2D or 3D. This information is combined with the length of the cavities and their operating frequencies to build the linac for the simulation code where a drift is defined at the distance between two cavity mid-planes.

RF errors from the klystron can be applied to the amplitude, V_{RF} and phase, ϕ in each cavity. In addition, SOMs and HOMs can be applied to each cavity. Each mode will have a $R/Q(\beta)$ calculated from Chapter 3 and Q_{ext} as chosen by the user. During the tracking simulation, a particle is defined to be lost if the following condition is met

$$2\phi_s < \phi < -\phi_s, \tag{4.22}$$

where ϕ_s is the synchronous phase, which is negative in the linac convention.

4.2.3 Transverse

The transverse plane is modelled using 2×2 transfer matrices as extracted from TraceWin. A transfer matrix describes the change in position and momentum of a particle passing through an accelerator element. The transfer matrices

are applied between the drift spaces between the cavity mid-planes and then at the midplane, a momentum kick is applied due to interaction with a dipole mode. The position and momentum error are calculated throughout the linac based on this scheme. For each simulation, unless mentioned specifically it is assumed that all cavities are aligned, there are no alignment errors in the focusing elements, the beam is injected on axis and the input error follows a gaussian distribution.

4.2.4 Implementation

The code is written in the Python scripting language [56] to allow user friendly syntax and an interactive interpreter. The tracking functions are written in C which are then called by Python to provide a much faster simulation time compared to Python on its own. Special care was taken to make the run scripts parallelised to allow the tracking of multiple linacs simultaneously. All simulations were run on a linux desktop with 12 dual-threaded cores and 48 GB of RAM. RAM was the limiting factor in terms of running multiple linacs. It was decided to save the energy and phase error of each bunch in each cavity. So for a train of 1 million bunches in a linac consisting of 200 cavities. Saving both energy error and phase error as 32 bit floats resulted in a 1.5 GB cost in RAM. For the input noise generation, the Mersenne Twistor random number generator was used [57].

4.2.5 Benchmark

In order to verify that the simulation provides correct results, the code was benchmarked as defined in [58]. 50,000 bunches were tracked in a generic linac calculating the energy and phase errors produced from HOMs. Figure 4.2 shows the comparision between the code used in this thesis and one used to benchmark against. The energy error and time error are plotted against each other. Upon comparison, the codes agreed with one and other to within numerical error as determined by the floating point precision.

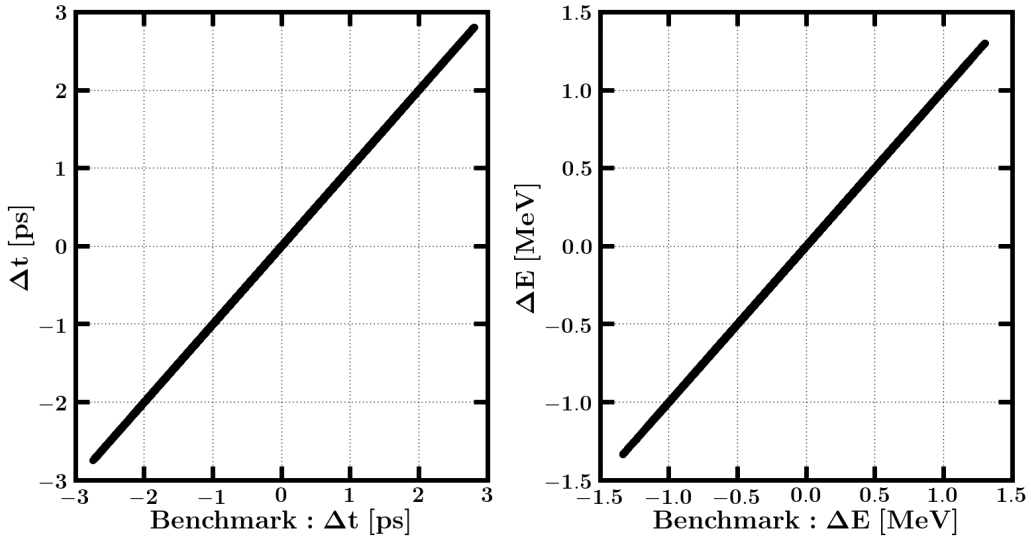

Figure 4.2: A comparison between two codes used for benchmarking.

4.3 Same Order Modes

For the studies into the SOMs, four linacs were investigated as shown in Table 4.1. The number of cavities for each family a long with their input energy are shown. The name of the linac follows from the standard ESS naming convention. Each linac was under consideration and thus, there susceptibility to SOMs was investigated to help choose the optimum.

Linacs	# Spokes	# Medium β	# High β	Energy In [MeV]
HS_2011_11_23	36	64	112	50
FD_SL_2012_04_13	32	60	120	79
FD_SSCL_2012_04_16	32	52	128	80
FD_SL_2012_05_15	28	60	120	79

Table 4.1: Linacs investigated for SOM simulations.

The HS_2011_11_23 linac made high temperature superconducting magnets and has shorter DTL resulting in a lower energy into the SRF linac. The linacs beginning FD used normal conducting magnets and included a longer DTL.

4.3.1 Input Distribution

Before studies could be performed, an input distribution for the SRF linac is required. A distribution was created by tracking one million bunches through the DTL with RF errors. The nominal values used for the errors was 1% and 1° however in the case of the HS_2011_11_23 linac, these errors resulted in losses in the superconducting section as shown in Figure 4.3. Therefore, for this linac, RF errors of 0.5% and 0.5° were deemed tolerable. The used injection patterns are shown in Figure 4.4.

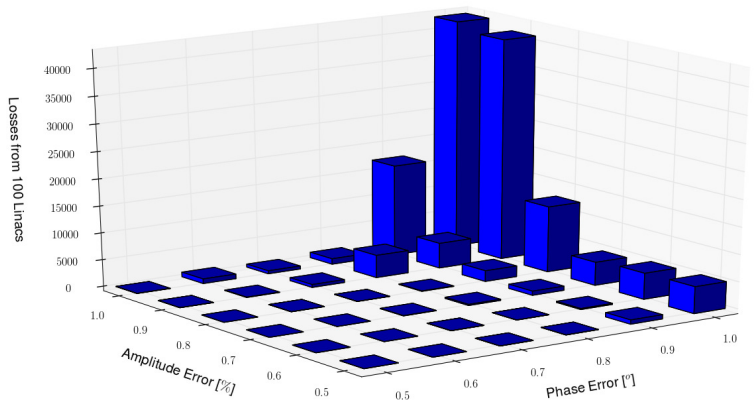

Figure 4.3: Losses in the HS_2011_11_23 linac.

4.3.2 Frequency Spread

The frequency spread of the SOMs will have a large effect on their influence. A smaller frequency spread will result in a larger coherence resulting in a stronger influence on the beam. Therefore, it is important to use a reasonable value. In the late 1980's, Ron Sundelin performed a series of studies measuring the distribution of resonant frequencies of SRF cavities [59]. The frequency spread based on empirical results is given by

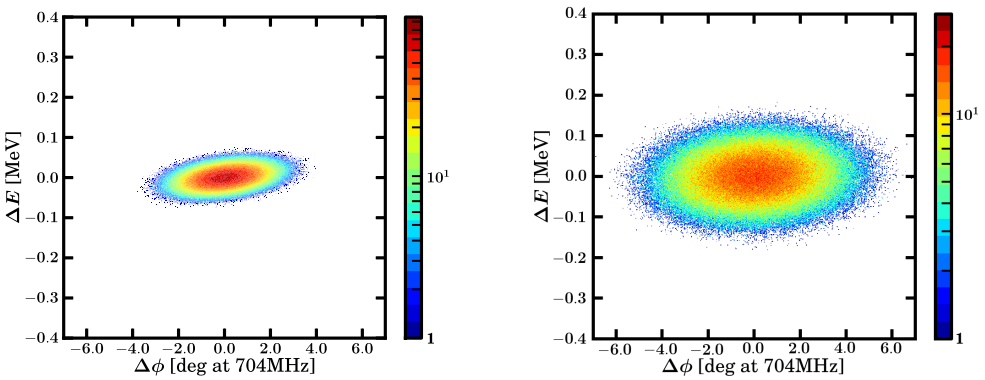

Figure 4.4: Injection patterns used for HS_2011_11_23 linac (left) and all other linacs (right).

$$\sigma = 1.09 \times 10^{-3} \cdot |f_n - f_0|. \tag{4.23}$$

where f_n is the frequency of the mode of interest and f_0 is the frequency of the accelerating mode. This means that for the elliptical cavities where the $4\pi/5$ mode is only ~ 1 MHz away from the accelerating mode, the frequency spread will be ~ 1 kHz.

4.3.3 Reference Simulation

Initially, one pulse, using the input distribution from the DTL, is tracked throughout each SRF Linac without any external effects such as rf errors or SOMs. This is to provide a reference output distribution in order to compare against. The pulse phase space at the exit of the HS_2011_11_23 linac is shown in Figure 4.5.

4.3.4 RF Errors

Jitter from the rf system will also lead to energy and phase errors. Uniformly distributed errors of $1\%, 1^\circ$ are used in each linac with the exception of the HS_2011_11_23 linac which uses errors of $0.5\%, 0.5^\circ$. Each linac is simulated 1000 times with a different set of uniformly distributed random errors each

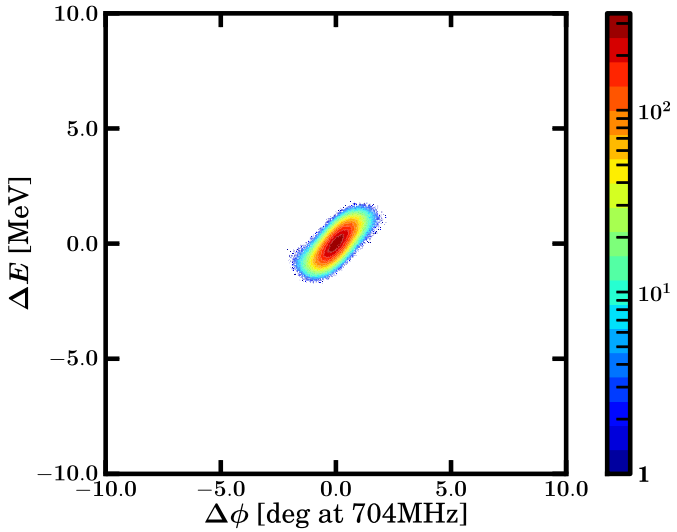

Figure 4.5: Phase space distribution at the exit of the HS_2011_11_23 linac with no external effects acting.

time. The phase space at the exit of these linacs is shown in Figure 4.6. It can be seen that there is a large increase the pulse phase space compared to the reference distribution. To quantify the growth, the area, ϵ, of the phase space created all the bunches are compared where the area is given by

$$\epsilon = \pi\sqrt{\langle\Delta E^2\rangle\langle\Delta\phi^2\rangle - \langle\Delta E\Delta\phi\rangle^2}, \tag{4.24}$$

where ΔE and Δt are the energy and phase error of the bunch with respect to the synchronous bunch. Therefore, the growth ϵ_{RF}/ϵ is used to determine the effects of the RF. In this case, the average growth is ~ 3.3. This growth will now be used as the tolerable growth due to SOMs or HOMs.

For these simulations, the effect of beam loading is ignored. Beam loading occurs as the bunch traverses a cavity, the induced electromagnetic fields act back on the bunch and the interaction does work on the particles. At high currents, the effect becomes comparable to that from the external RF and thus needs to be compensated. It is assumed that beam loading is compensated for by the RF system and thus why it is ignored.

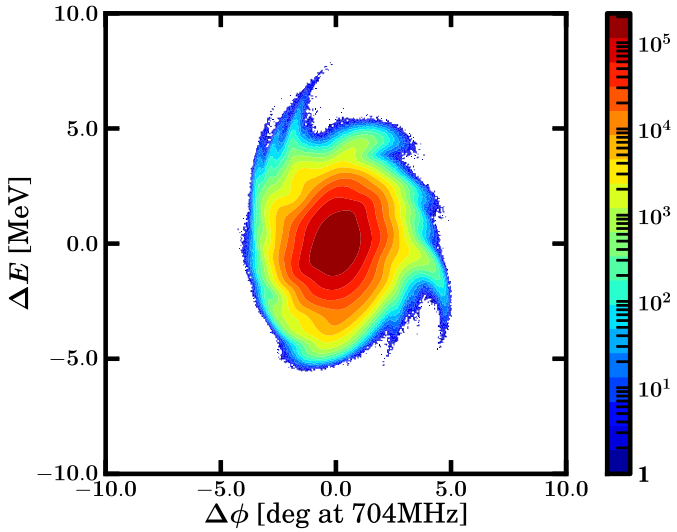

Figure 4.6: Phase space distribution at the exit of the HS_2011_11_23 linac with uniformly distributed errors of 0.5% in amplitude and 0.5° in phase.

4.3.5 Same Order Modes Simulation

Using the same input distribution as before, one pulse is tracked through each linac with a SOM present in each cavity. For each cavity family, the SOM with the highest summed $R/Q(\beta)$ over the velocity range is used for simulations. For the spokes, the second mode is used and for the ellipticals, the $4\pi/5$ mode is used. The $R/Q(\beta)$ that will be seen in each cavity for the whole HS_2011_11_23 linac is shown in Figure 3.6. Of particular concern are the regions at the beginning of the spoke and medium beta sections where the $R/Q(\beta)$ of the SOMs are larger than that of the accelerating mode. The parameters used for the simulation are shown in Table 4.2. An unrealistically large Q_{ext} of 10^8 is used to show a worst case scenario.

The simulation is performed 1000 times using a different seed for the random number generator to set the frequencies of the SOMs. All other parameters are left constant. The phase space at the exit of 1000 HS_2011_11_23 linacs is shown in Figure 4.7,

It can be seen that for the HS_2011_11_23 linac there is a large effect on the pulse phase space, with an average growth of ~ 3.1. In 15/1000 linacs, bunches

Injected Beam		Mean	σ
E	[MeV]	79	0.062
ϕ_s	[deg at 704 MHz]	-29	2.3
I_b	[mA]	50	1%
Pulse			
T_b	[ns]	2.84	
# Bunches		1,000,000	
Monopole Mode	Spoke $\beta_{opt} = 0.5$		
f_n	[MHz]	362.698	0.01
Type		0	
Q_{ex}		10^8	
Monopole Mode	medium beta $\beta_G = 0.7$		
f_n	[MHz]	703.256	0.001
Type		$4\pi/5$	
Q_{ex}		10^8	
Monopole Mode	high beta $\beta_G = 0.86$		
f_n	[MHz]	703.241	0.001
Type		$4\pi/5$	
Q_{ex}		10^8	

Table 4.2: Parameters used for SOM simulations in each linac.

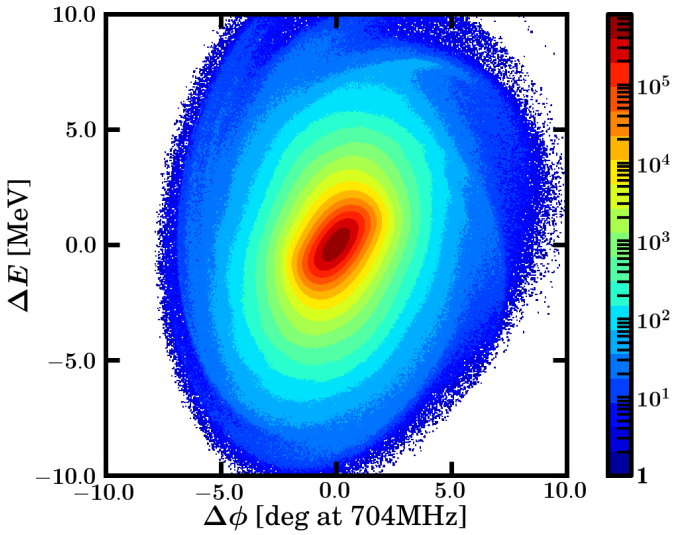

Figure 4.7: Phase space distribution at the exit of the HS_2011_11_23 linac with SOMs present in the cavities.

were lost. Figure 4.8 shows the exit distributions FD_SL_2012_05_15 linac. As before, the distribution represents the pulse phase space for 1000 linacs for the cases where there are no external effects, SOMs present and RF errors. The exit distributions for the FD_SSCL_2012_04_16 and FD_SL_2012_04_13 linacs are very similar and are therefore, not shown. The effect of RF errors and SOMs on all the Linacs are shown in Table 4.3. While the HS_2011_11_23 linac shows it is possible to design a linac susceptible to SOMs, the effect on the other linac designs is much smaller with a maximum growth of only 1.5 that of the case when no SOMs are present and still well below the growth caused by RF errors. It can be seen that these linacs show a small increase in growth due to RF errors compared to the HS_2011_11_23 linac however this is mainly due to use of larger RF errors $(1\%, 1^\circ)$ compared to $(0.5\%, 0.5^\circ)$ in the HS_2011_11_23 linac.

4.3.6 Current and Damping Scan

The final investigation was to vary the current, Ib and Q_{ext} for the simulations involving the May Baseline linac FD_SL_2012_05_09. The current was varied

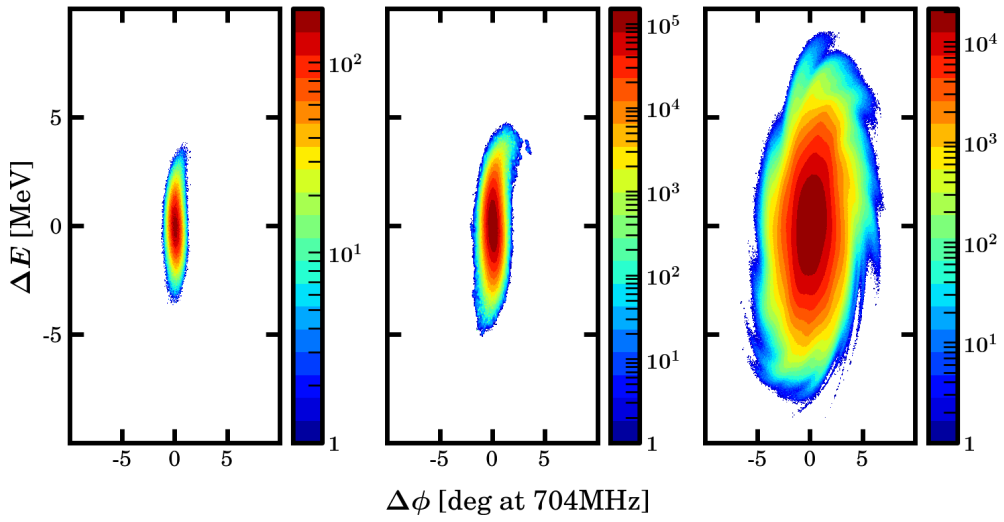

Figure 4.8: Phase space distribution at the exit of the FD_SL_2012_15_15 linac with no external effects (left), SOMS (middle) and RF errors (right).

SOMs	Average Growth	Max Growth	Rms Growth	90^{th} Percentile Growth
HS_2011_11_23	3.1	56.6	4.4	5.5
FD_SL_2012_04_13	1.02	1.2	0.02	1.03
FD_SSCL_2012_04_16	1.01	1.5	0.02	1.02
FD_SL_2012_05_15	1.02	1.47	0.04	1.04
RF Errors	Average Growth	Max Growth	Rms Growth	90^{th} Percentile Growth
HS_2011_11_23	3.3	13	1.9	5.8
FD_SL_2012_04_13	4.24	16.2	2.4	7.6
FD_SSCL_2012_04_16	3.9	14.5	2.06	6.6
FD_SL_2012_05_15	3.7	16.6	2.06	6.5

Table 4.3: Linacs investigated for SOM simulations.

from the nominal current of 50 mA to a relatively high current of 150 mA in order to determine the existence of a threshold and how close the nominal current is to that threshold. The Q_{ext} is varied from 10^4 to 10^9, despite the fact that it is expected that the actual value will lie much closer to that of the fundamental mode, 10^6. The results are shown in Figure 4.9. At the nominal current, negligible growth is observed and it is not until 90 mA where the growth starts to exceed that of RF errors. Losses are also seen at this current for $Q_{ext} > 10^7$.

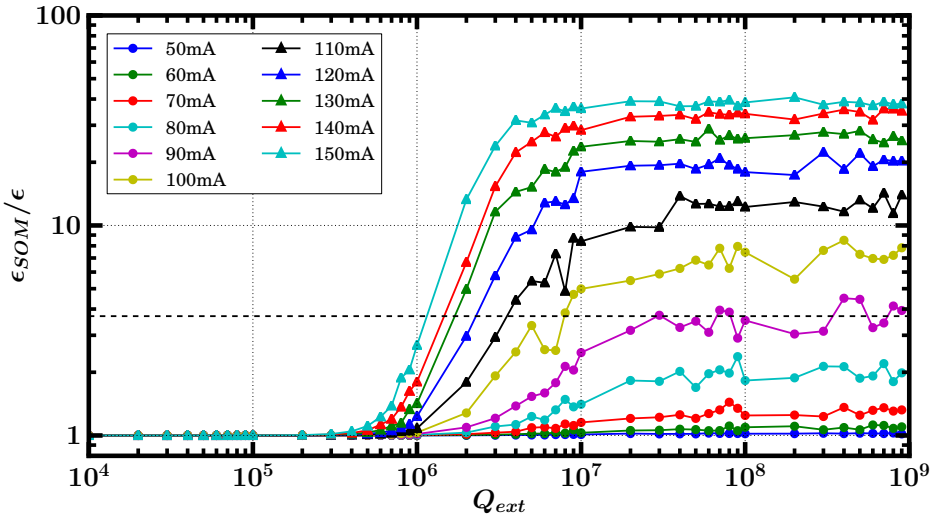

Figure 4.9: The average longitudinal phase space increase for 100 linacs at varying currents and Q_{ext} of the SOMs.

4.4 Higher Order Modes

Higher Order Modes (HOMs) are also a concern. As well as having high a $R/Q(\beta)$ across the velocity range, the frequency of these modes could also lie on a machine line resulting in a resonant amplification effect. This was not a concern for the SOMs as the fundamental accelerating mode is always tuned to lie on the machine line.

For the following simulations, only the latest baseline linac layout is used.

4.4.1 High R/Q HOMs

Initially, the HOMs with the highest R/Q, which are not on machine lines are considered. Once again the current, Ib, and Q_{ext} are scanned in the same range as for the SOMs. For each parameter, 100 linacs are simulated with a gaussian frequency as determined by Sundelin's formula. For the case of HOMs, the spread of the frequencies are of the order of MHz. The results are shown in Figure 4.10.

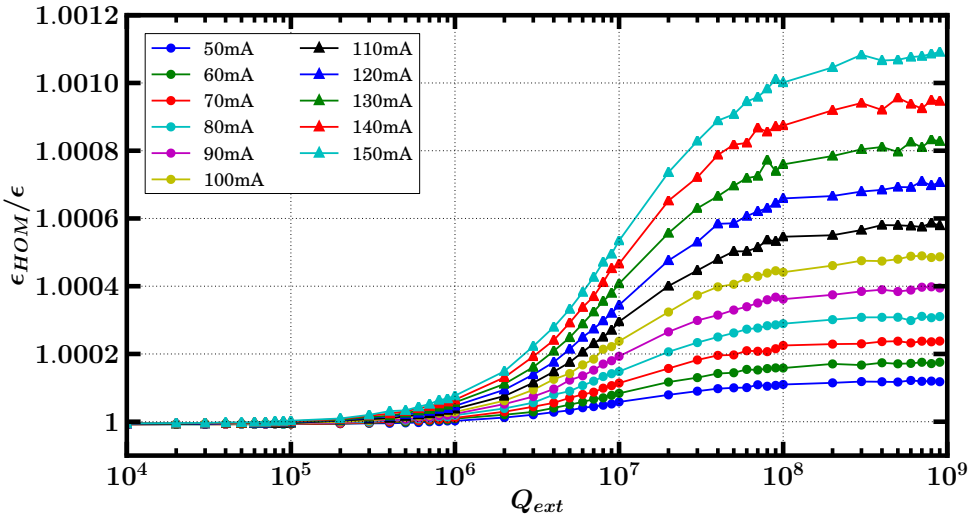

Figure 4.10: The average longitudinal phase space increase for 100 linacs at varying currents and Q_{ext} of the HOMs.

It can be seen that the growth increases with both current and Q_{ext} however even for the largest of these two parameters, the growth is negligible. Therefore, modes with high R/Q that lie far away from a machine line will not result in any unwanted effects on the beam dynamics.

4.4.2 Machine Lines

Of most concern is when a HOM lies on a machine line. In order to assess the danger presented by a particular mode, a figure of merit, κ_i is defined as

$$\kappa_i = P_i \cdot R/Q, \tag{4.25}$$

where P_i represents the probability that, for at least one cavity, the frequency of any individual HOM is shifted to lie exactly on the nearest machine line. The probability is derived from a gaussian probability density function with a width equal to the HOM frequency spread and is normalised such that it is unity when HOM lies on a machine line. Thus, for a mode lying precisely on a machine line, $\kappa_i = R/Q$ since $P_i = 1$ for such a mode, and for a mode lying many standard deviations from a machine line, P_i is effectively zero due to the very low probability of it shifting such a large distance. The mode with the highest κ_i was then simulated for 1000 linacs with only two showing any significant growth.

The final simulation was to determine the minimum distance a mode can be from a machine line without causing any significant growth. The frequency of the modes with the highest R/Q were shifted to lie exactly on the fourth machine line, 1408.84 MHz, and simulated for 100 linacs with different frequencies and Q_{ext} of 10^8. This was then repeated by shifting the centre frequency by a MHz at a time. The results are shown in Figure 4.11.
As expected when the modes lie exactly on a machine line, the impact on beam is huge and bunches are lost. However, once the frequency is shifted by 3 MHz or more, the growth is neglible. Therefore, during the cavity design phase, care should be taken to avoid any modes lying within 3 MHz of a machine line.

4.4.3 Transverse HOMs

The transverse plane is modelled using 2×2 transfer matrices as extracted from TraceWin [55]. As in the longitudinal plane, the dipole mode frequencies have a gaussian spread with a width set by Sundelin's formula. All simulations use an input gaussian distribution with a width of 1 mm in x and 0.5 mrad in x' [60].The initial simulations scanned Q_{ext} and current using the dipole modes with the highest $R/Q_{\perp}$. The results are shown in Figure 4.12.

The results for the dipoles are very similar to that of the longitudinal plane showing almost negligible growth. Shifting these modes to a machine line also

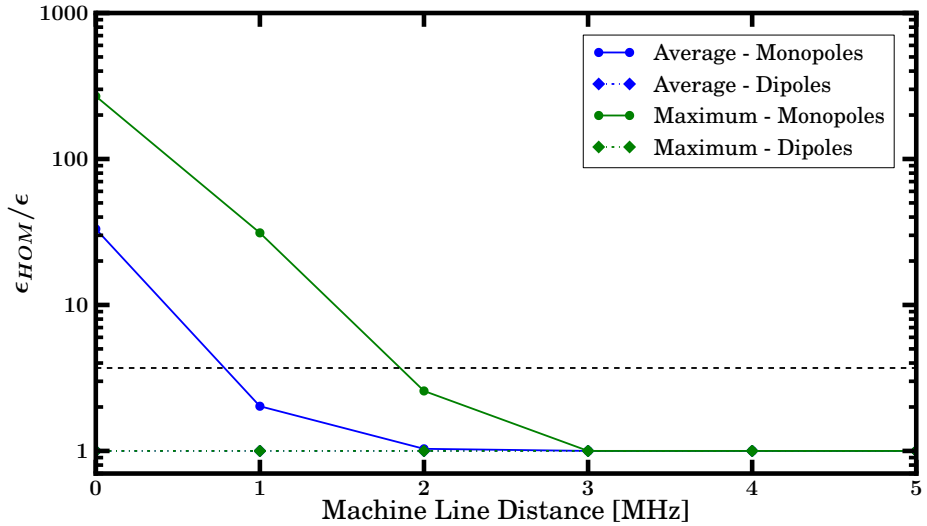

Figure 4.11: The average and maximum longitudinal and transverse phase space growth as a function of the distance a HOM is from a machine line.

showed very little effect as can be seen from Figure 4.11 and thus, dipoles modes are not expected to cause any concerns for beam quality.

4.4.4 Damping requirements

The influence of parasitic modes in the ESS linac have been investigated in the longitudinal and transverse plane. It has been shown that although it is possible to design a linac susceptible to modes in the fundamental passband, the present baseline is not affected at the nominal current and should operate up to currents of 100 mA if upgrades are desired in the future.

It was shown that Higher Order Modes in both the longitudinal and transverse plane are of little concern as long as they far away from machine lines. Close to machine lines, monopoles modes provide much more of a danger and care must be taken during the cavity design phase to avoid modes sitting on these resonances and it is recommended that a distance of a least 5 MHz will be safe. The safety limit is increased from 3 to 5 MHz to account for manufacturing errors.

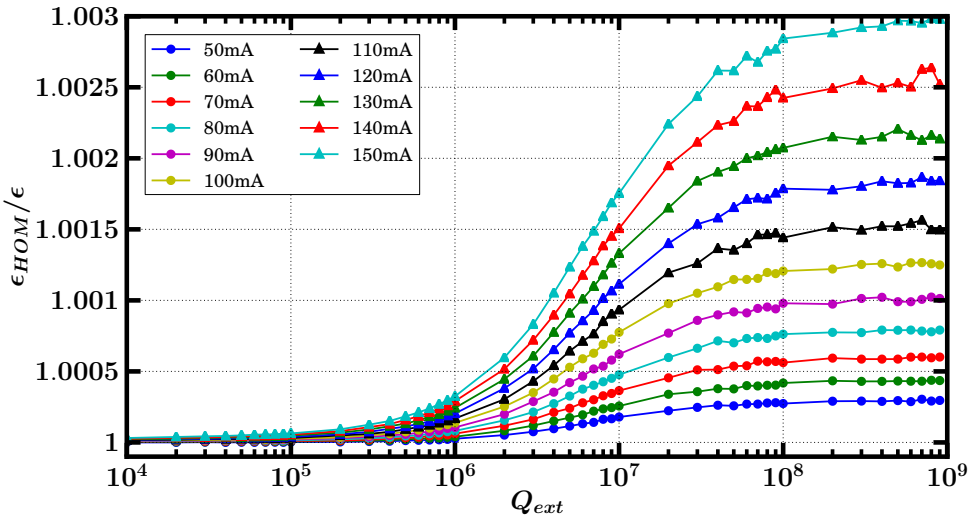

Figure 4.12: The average transverse phase space increase for 100 linacs at varying currents and Q_{ext} of the HOMs.

4.4.5 HOM Coupler Decision

Following on from this result, HOM couplers are not required for the nominal operation of the machine. However, it should be noted that by not installing couplers, this will limit the future flexibility of the machine if chopping schemes of $\sim$ 100 kHz or higher are desired.

4.5 Higher Order Mode Spectra Shift

It has been shown that, it is important that cavities are designed such that their modes are far away from the machine lines. Of concern, is if a cavity is fabricated with a mode too close to a machine line. It has been suggested [61] that detuning and retuning the cavity, as well as warming up and cooling down the cavity could cause the HOM frequencies to shift slightly due to the cavity not being perfectly elastic.

To investigate these effects, a study was performed at FLASH. FLASH [62] is a Free Electron Laser facility generating short laser-like pulses with a wavelength between about 4 and 45 nm. It is also a test facility for the European

X-ray FEL and the International Linear Collider. To accelerate the beam, seven cryomodules containing superconducting nine-cell cavities operating at 1.3 GHz are used.

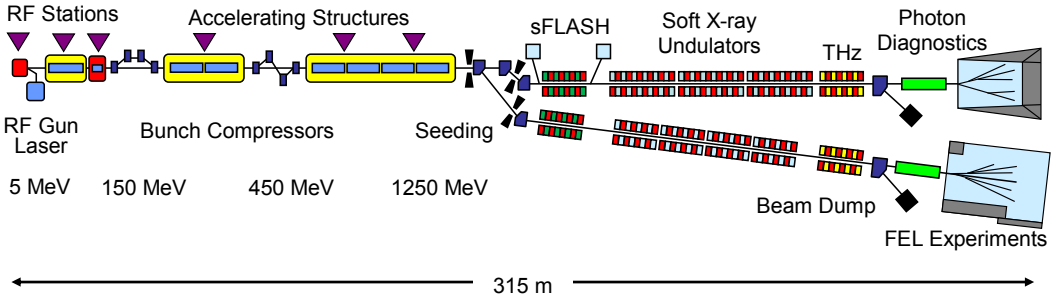

Figure 4.13: A schematic of the FLASH accelerator.

For the measurements presented here, cavities were measured in the fifth (ACC5) and seventh (ACC7) cryomodule.

4.5.1 Set-up

The Higher Order Mode spectra was measured using a Agilent 8753ES Network Analyser (NWA) connected to the HOM couplers of a cavity. For each cavity, the first two dipole passbands were measured from 1.6 GHz to 1.888 GHz along with the first quadrupole passband measured from 2.293 GHz to 2.32 GHz. An example measurement of the passbands at the beginning of the measurement process is shown in Figure 4.14. The NWA was limited to a maximum data sample of 1601 points, therefore in order to get a good resolution of the modes, 500 data samples were taken for the dipole passbands and 50 data samples for the quadrupole passbands. The high number of data samples needed meant that the time to measure all three passbands was slow and on the order of 15 minutes.

The NWA is used to measure the S-parameters. In this case, the S21 was measured which tells how much power is transmitted from port 1 to port 2.

Only eight out of the nine quadrupole modes were visible from the measurement. This possibly due to the passband falling outside the measured

frequency range, alternatively, this mode may not be visible from the S21 measurement.

The fundamental passband was not visible on the NWA. This is thought to be because the NWA was connected to the HOM couplers which by design, reject the fundamental mode.

The NWA had only 2 ports, therefore in order to prevent the need to continually plug and unplug cables, a Keithley S46 microwave switch system was used. The measurements involving the NWA and switch were automated using LabView.

4.5.2 Effects of detuning the cavities

Before the superconducting linac was warmed up, the cavities were detuned to their relaxed state. Measurements were performed on cavity 1 from ACC7 before and after detuning in order to determine the frequency shift in the measured passbands. The accelerating mode in Cavity 1 was detuned by 305 kHz. Figure 4.15 shows the shift in frequencies of the dipoles and quadrupoles for ACC7-C1. The shift is calculated by subtracting the detuned frequencies from the tuned frequencies. Thus, a negative shift means the frequency has increased. The shift varies from -700 kHz to 200 kHz in the two dipole passbands however remains around 900 kHz for the quadrupole modes. Also of interest, is how the shift for the dipoles changes from negative to positive as the frequency increases in a smooth trend and then suddenly drops at the beginning of the new passband.

4.5.3 Cool-down Measurements

During the cool-down of the superconducting linac from 300K to 2K, the passbands were continually measured to observe how their frequencies shifted during the temperature change. The first cavities from ACC5 and ACC7 were measured during the cool-down. The temperature as a function of time is shown in Figure 4.16. It can be seen that temperature drops at a relatively constant rate until around 60 K where the gradient increases. The right plot

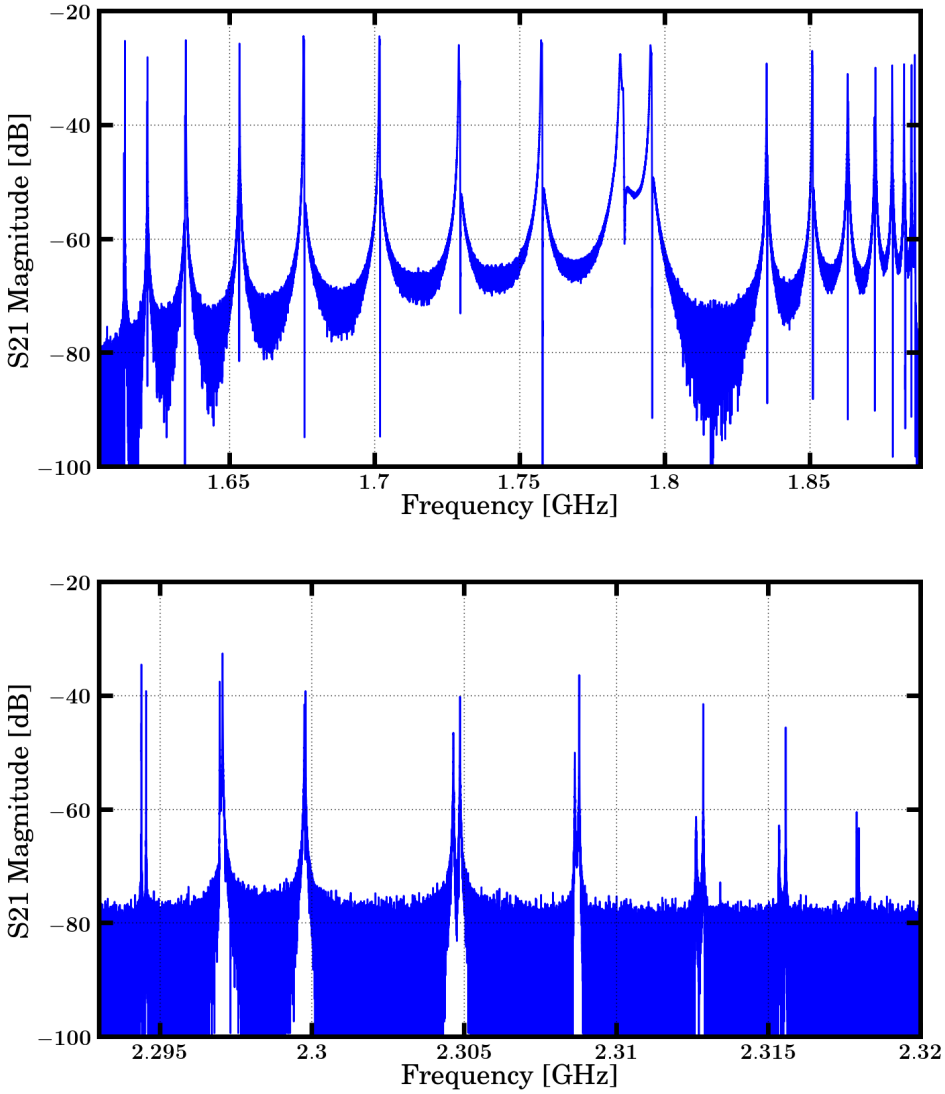

Figure 4.14: The first two dipole passbands and quadrupole passbands measured from ACC7-Cav1 before detuning.

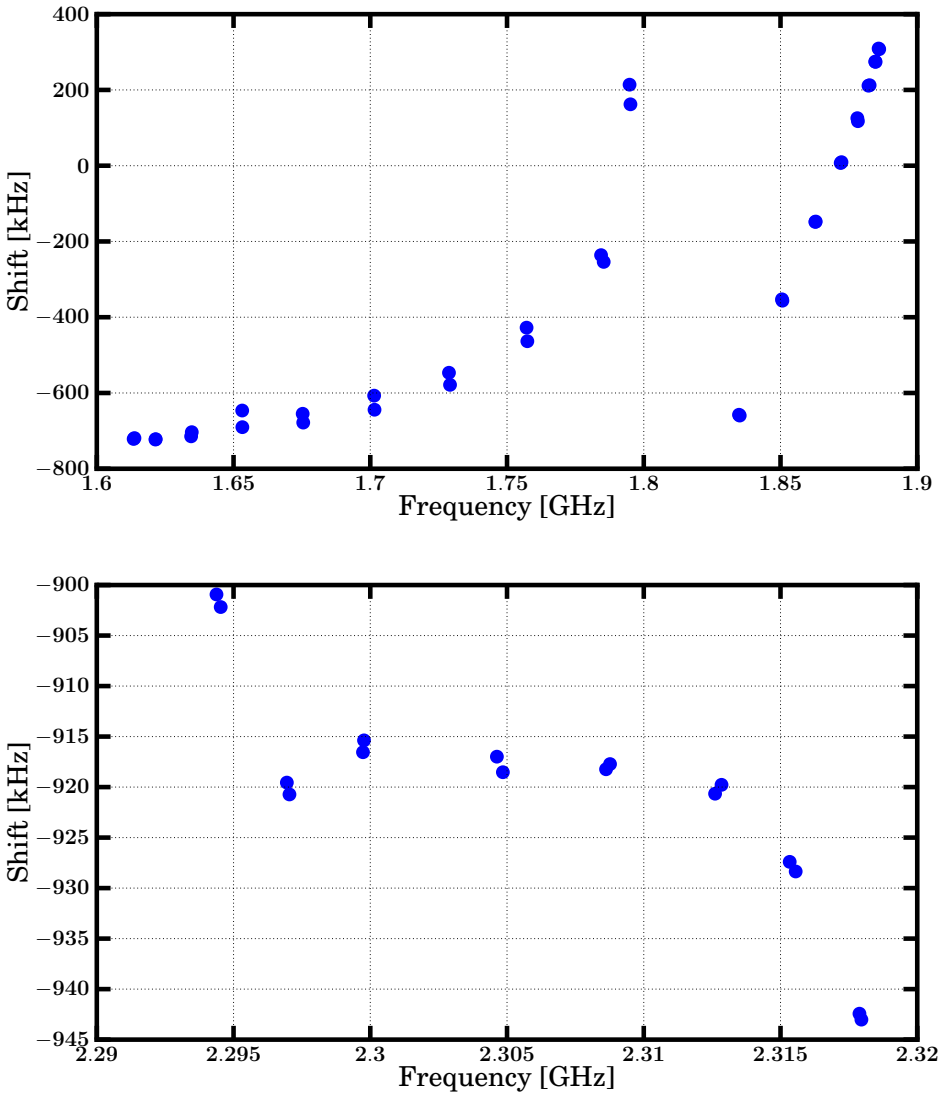

Figure 4.15: The shift in the dipole(top) and quadrupole(bottom) frequencies after the accelerating mode had been detuned by 305 kHz.

shows the temperature drop near and during the phase when the cavities become superconducting (T<9.2 K). Here the temperature has a very steep gradient from 10 K to 4.2 K where it remains constant until a final procedure is made to lower the temperature to 2 K.

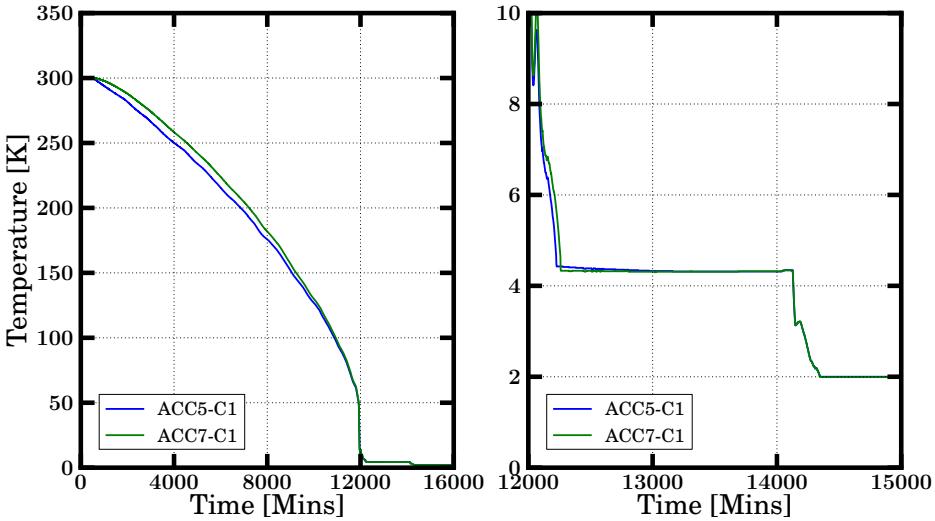

Figure 4.16: The temperature of the cavities measured as a function of time. The right plot shows a zoom in of the period when the cavities are superconducting.

The spectra of the passbands at temperatures of 300 K, 200 K, 100 K, 50 K, 10 K, 4.2 K and 2 K were then compared. It is important to note that at 10 K the temperature drop was very fast meaning that the modes could be at a temperatures below this. At high temperatures, it was extremely hard to detect the quadrupole modes and so only data from 10 K will be used in statistics.

Figure 4.17 shows the first dipole mode in ACC5-C1 as the temperature drops. It can be seen that as the temperature decreases, the frequency gradually increases as well as the quality factor. Between 10 K and 2 K, a very small frequency shift is observed however a massive increase in Q_0 compared to 50 K due to cavity now being superconducting.

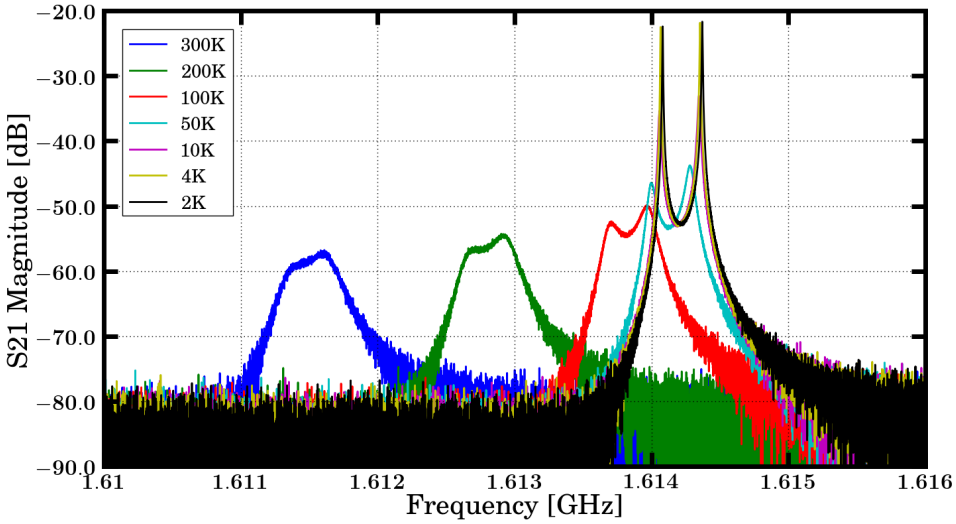

Figure 4.17: The first dipole mode in ACC5-Cav1 at different temperatures.

Figure 4.18 shows the fourth quadrupole mode in ACC7-C1 as the temperature drops. At temperatures above 50 k, the resonances are particularly hard to resolve, especially both polarisations.

Figure 4.19 shows how the dipole and the quadrupole frequencies have shifted after the cavity has been warmed up and re-cooled down to 4.2 K and 2K. The comparison is made with the detuned cavity frequencies. It can be seen that the frequency shift from 4.2 K to 2 K is quite large and is not thought to be just caused by the compression of the cavity due to cooling. The extra shift is thought to be caused by the pressure change that occurs. After being warmed up and re-cooled, it is apparent that the frequencies have not returned to their initial state and have shifted which for the majority of modes is around 20 kHz. Once again, the dipole modes show a much greater variation in shift as compared to the quadrupole modes.

4.5.4 Effects of retuning the cavities

After the cool-down was complete, the cavities were then retuned to return the accelerating mode to 1.3 GHz. The final shift in dipole frequencies between the original tuned cavity and the final cavity after being detuned, warmed

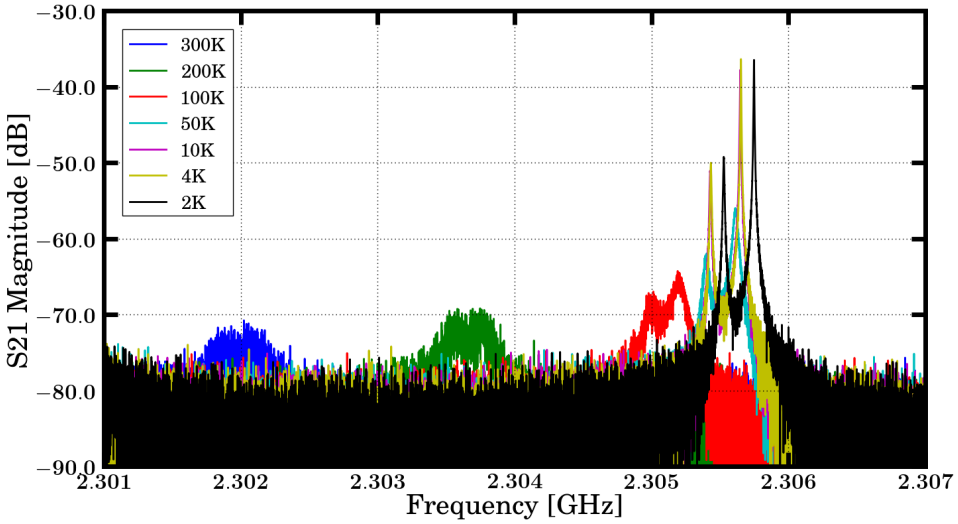

Figure 4.18: The first quadrupole mode in ACC7-Cav1 at different temperatures.

up, cooled down and retuned is shown in Figure 4.20. The final shift for the quadrupole modes is not shown due to uncertainties with the measurement.

The total shift is in most cases less than 5 kHz with some exceptions of much higher shifts. The biggest being close to 65 kHz. On-going analysis of the other cavity data is expected to determine if this shift is an anomaly.

4.5.5 Summary

The shift of the modes in the first two dipole passbands and first quadrupole passband is observed while the cavity undergoes external effects. The cavity was first detuned before being warmed to 300 K. The cavity was then cooled down to 2 K and retuned. The cavity spectra was measured at various stages. Table 4.4 shows the shift in mode frequencies for the first dipole passband in ACC7-Cav1, Table 4.5 shows the same information for the second dipole passband and Table 4.6 shows the shifts for the quadrupole passband.

Analysis of the results of one cavity suggest that the whole cycle will result in frequencies shifts on the order of several kHz. The final shifts are much

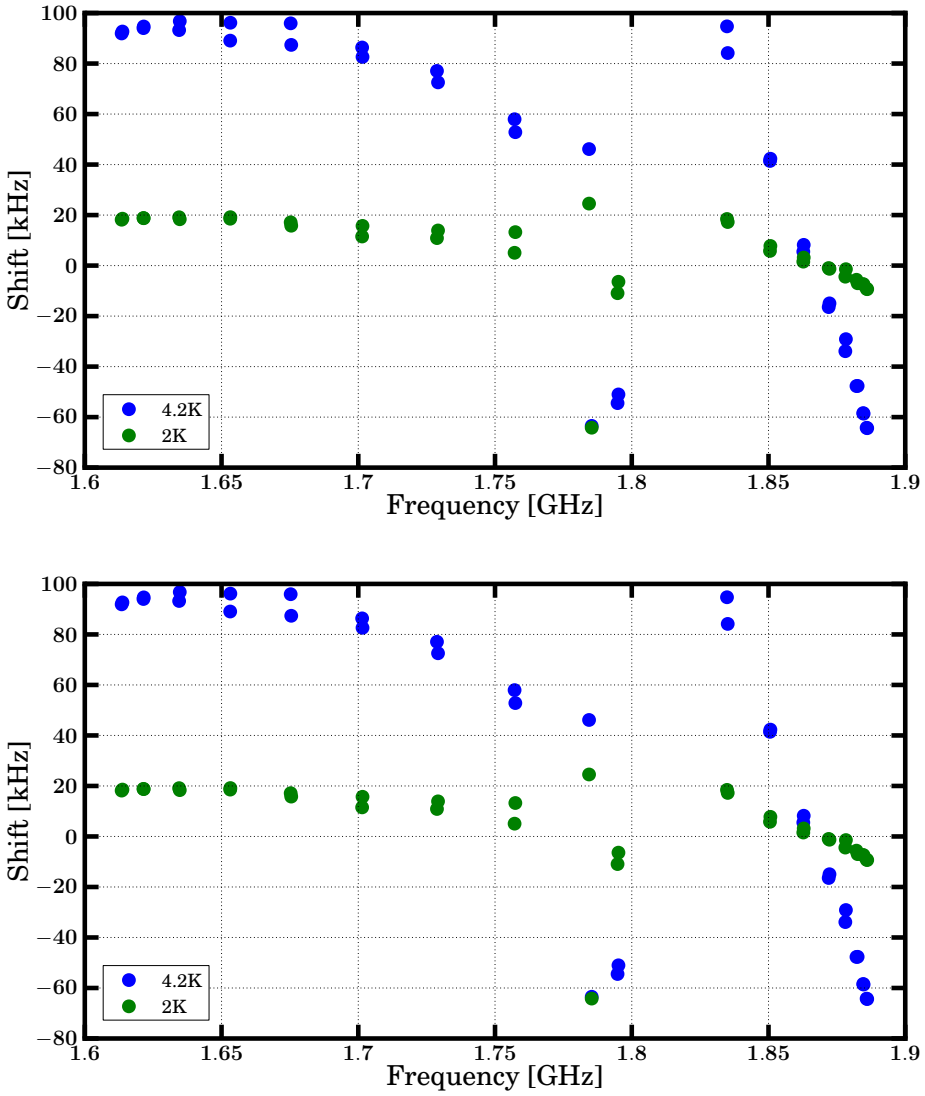

Figure 4.19: The shift between the detuned cavity before the warmup and the cavity at 4.2 K and 2 K during the cool-down. Dipole (top) and Quadrupoles (bottom) are shown.

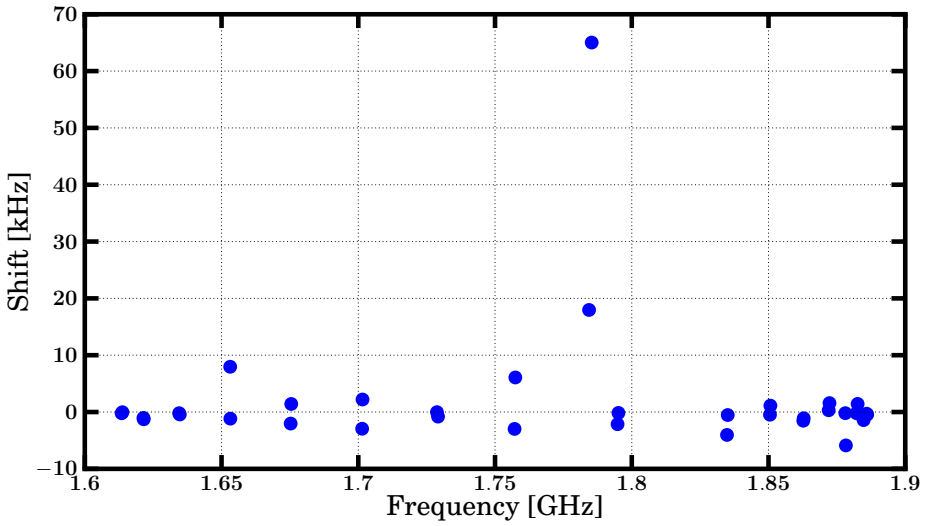

Figure 4.20: The shift in frequency after the cavity has been detuned, warmed up, cooled down and then retuned.

lower than the 5 MHz limit set out in section 4.4.4 and thus, is not thought to be of concern for cavity design.

However, it is important to note that a technique of detuning or warming up the cavities will not be enough to move a mode away from a resonance and so maintaining the 5 MHz limit during the cavity design is vital.

The tuning effects measured in this paper made use of the slow tuners. Of future interest, is the effect of the fast piezo tuners used to keep the cavity operating close to resonance during operation. It is of interest to see how the HOM spectrum responds to the fast tuners and whether this has an effect on diagnostic systems that make use of the HOMs.

Table 4.4: The shift in frequency due to tuning and temperature for the first dipole passband in ACC7-C1.

f_0 [GHz]	Δ f [kHz]							
Tuned	Detuned							Tuned
2 K	2 K	300 K	200 K	100 K	50 K	4.2 K	2 K	2 K
1.61347	-721.4	1946.5	756.7	-252.1	-561.8	-629.5	-703.2	-0.2
1.61376	-719.1	1882.0	726.4	-282.8	-569.6	-626.4	-700.5	-0.0
1.62144	-722.9	1909.0	732.9	-280.9	-564.1	-628.8	-704.0	-1.0
1.62154	-722.0	1917.8	746.7	-294.1	-576.2	-627.3	-703.2	-1.3
1.63449	-714.4	1846.9	692.7	-325.1	-579.1	-621.2	-695.3	-0.2
1.63473	-703.4	1954.2	783.9	-254.1	-545.5	-606.7	-685.1	-0.4
1.65317	-646.3	2105.8	868.9	-193.9	-483.1	-557.2	-627.8	8.0
1.65322	-690.2	1976.9	792.5	-253.7	-542.3	-594.1	-671.1	-1.2
1.67528	-654.9	2036.1	845.6	-212.5	-502.8	-559.0	-637.8	-2.0
1.67548	-678.2	2061.5	855.9	-202.9	-513.4	-590.8	-662.4	1.4
1.70141	-607.0	2120.1	903.0	-164.5	-459.9	-520.7	-595.5	-2.9
1.70155	-644.2	2117.0	899.1	-199.3	-489.6	-561.6	-628.5	2.2
1.72877	-546.6	2232.4	981.1	-104.0	-409.5	-469.5	-535.7	-0.0
1.72916	-578.5	2265.1	999.7	-98.7	-436.5	-505.9	-564.6	-0.8
1.75715	-427.5	2358.6	1109.8	6.4	-307.3	-369.6	-422.5	-3.0
1.75743	-463.4	2387.8	1121.7	2.8	-337.5	-410.5	-450.1	6.1
1.78438	-236.1	2578.5	1362.1	222.7	-131.0	-190.0	-211.6	18.0
1.78535	-253.9	2457.5	1128.2	100.3	-270.3	-317.4	-318.1	65.0

Table 4.5: The shift in frequency due to tuning and temperature for the second dipole passband in ACC7-C1.

f_0 [GHz]	Δ f [kHz]							
Tuned	Detuned							Tuned
2 K	2 K	300 K	200 K	100 K	50 K	4.2 K	2 K	2 K
1.79481	213.9	2988.3	1746.0	598.3	231.4	159.4	202.9	-2.1
1.79513	162.0	2956.5	1709.5	561.1	170.0	111.0	155.6	-0.2
1.83482	-657.5	2255.7	945.8	-197.2	-524.3	-562.8	-639.0	-4.0
1.83509	-659.6	2411.8	906.1	-224.0	-539.1	-575.5	-642.4	-0.5
1.85054	-352.8	2533.1	1239.7	85.5	-271.7	-311.3	-346.9	-0.5
1.85069	-356.4	2557.0	1260.3	93.6	-263.7	-314.0	-348.6	1.1
1.86272	-148.4	2765.9	1461.7	283.4	-100.5	-142.9	-146.9	-1.5
1.86287	-147.5	2721.0	1424.7	254.3	-108.7	-139.3	-144.3	-1.1
1.87200	7.0	2924.9	1627.9	437.4	34.5	-9.4	6.1	0.3
1.87230	9.3	2886.3	1592.5	412.4	26.8	-5.6	8.0	1.6
1.87809	125.4	3013.3	1719.2	527.2	129.0	91.5	121.0	-0.2
1.87830	117.5	2968.0	1701.3	518.7	140.6	88.4	116.1	-5.9
1.88216	211.2	3099.6	1794.4	603.9	198.7	163.5	205.6	-0.2
1.88259	212.4	3075.0	1765.4	572.0	181.7	164.8	205.4	1.4
1.88462	274.7	3181.2	1868.4	675.7	255.1	216.3	267.4	-1.0
1.88477	274.2	3157.0	1846.0	654.1	248.6	215.5	266.6	-1.4
1.88587	309.3	3202.1	1883.8	688.7	279.2	245.1	300.1	-0.3
1.88609	307.5	3329.3	1976.2	722.0	282.0	243.1	298.2	-0.4

Table 4.6: The shift in frequency due to tuning and temperature for the first quadrupole passband in ACC7-C1.

f_0 [GHz]	Δ f [kHz]				
Tuned	Detuned				
2 K	2 K	50 K	10 K	4.2 K	2 K
2.29438	-900.9	-743.8	-782.9	-788.3	-878.4
2.29453	-902.2	-751.6	-784.0	-788.7	-879.4
2.29695	-919.6	-696.9	-798.1	-803.2	-895.9
2.29704	-920.7	-766.5	-798.5	-803.6	-897.0
2.29973	-916.5	-756.2	-794.0	-799.1	-893.5
2.29977	-915.4	-954.4	-792.9	-797.9	-892.4
2.30463	-917.0	3866.1	-794.0	-799.0	-893.1
2.30485	-918.5	-425.2	-795.5	-800.2	-895.7
2.30862	-918.2	3223.2	-793.3	-798.7	-894.4
2.30877	-917.7	3159.0	-792.7	-798.1	-894.9
2.31261	-920.7	3219.3	-793.5	-797.2	-898.1
2.31284	-919.8	3321.6	-792.7	-797.7	-896.5
2.31534	-927.4	1967.5	-799.0	-803.4	-904.3
2.31555	-928.4	1952.7	-800.3	-805.0	-904.9
2.31789	-942.4	1783.7	-813.4	-818.1	-919.0
2.31796	-943.0	1642.0	-814.5	-818.6	-919.4

Chapter 5

Higher Order Mode Coupler Design

In the previous chapter, it was concluded that Higher Order Mode couplers would not be needed for the baseline ESS lattice design. However, it could still be possible that baseline changes, such as the inclusion of fast choppers, could occur, in which case this decision would need to be revisited. Thus, studies were performed on HOM coupler designs to decide if they could be used, if they are needed for the ESS cavities. These studies would also be directly applicable to other machines making use of 704 MHz cavities. This chapter will begin with an introduction to coupler design and look at the risks associated with two particular designs. Modifications to improve this designs are then presented.

5.1 Higher Order Mode Coupler

There exists different possible methods to dampen Higher Order Modes in superconducting cavities. For the case of ESS and SPL, a coaxial type coupler is chosen. Waveguide couplers provide better broadband damping however may be too large to fit in the cryomodule. Ferrite absorbers may also be ruled out by space limitations.

To design a coaxial coupler, two objectives must be met. Firstly, to maximise the damping of all dangerous HOMs across the frequency range and

secondly, to minimise the amount power coupled out of the accelerating mode. To help understand the coupler design, a circuit model is considered.

The coupler port can be treated as the output port of a generator, such as a current source, in parallel with an internal impedance, C_s. If $\vec{E}$ is the electric field of the HOM, I_0 is the current picked up by the antenna with a short circuit across the port. I_0 can be determined by performing an integral of the electric field over the area of the coupling antenna.

$$I_0 = \omega\epsilon_0 \int \vec{E} \cdot \mathrm{d}s, \tag{5.1}$$

where ω is the frequency of the HOM in question. If a real load R is connected across the coupler, the maximum dissipated power P that can be obtained is

$$P = \frac{1}{4}\frac{I_0^2}{\omega C_s}, \tag{5.2}$$

where the load R is at its maximum value, $1/\omega C_s$. In order to maximise the dissipated power, the probe should be designed to minimise the stray capacitance which means to reduce the features that add capacitance but do not interact with the electric field lines from the HOM. The external quality factor of the coupler is:

$$Q_{ext} = \frac{\omega U}{P} = \frac{4UC_s}{\epsilon_0^2(\int \mathbf{E} \cdot \mathrm{d}s)^2} = \frac{4U}{\omega R\epsilon_0^2(\int \mathbf{E} \cdot \mathrm{d}s)^2}. \tag{5.3}$$

The coaxial coupler can extract HOM power from the cavity using two methods. One via the electric field using an antenna and the other via the magnetic field using a loop. The interaction between the cavity and antenna can be analysed using a lumped circuit model as shown in Figure 5.1.

The elements R, L, C represent the cavity as a resonator. The capacitance C_c corresponds to the electric field lines that terminate on the antenna tip. R, L, C and C_c will in general be different for each mode. It is important to make the impedance for the HOMs as low as possible in order to provide damping. The transforming part of the coupler is a microwave circuit. It is usually desired to use a standard (50 Ω) coaxial transmission line to remove the HOM power from the cryostat. In order to bring the optimum value of R

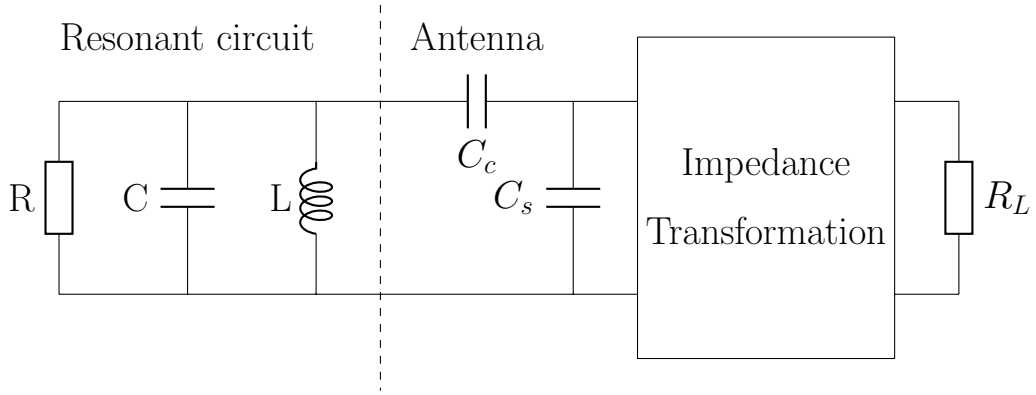

Figure 5.1: An equivalent circuit representing the interaction between the cavity and an electric antenna.

closer to 50 Ω, an inductor L is added in parallel to the stray capacitance C_s in order to compensate C_s. Exact compensation can be achieved but only at a single frequency

$$f_c = \frac{1}{2\pi\sqrt{LC_s}}. \tag{5.4}$$

The inductance L is usually chosen such that f_c matches the frequency of the mode with the highest R/Q in order to provide the strongest damping. Damping for one mode can be maximised by choosing the inductance L appropriately however this will be at the expense of damping for other modes. Nearby modes can also be efficiently damped with some bandwidth Δf around the frequency f_c at which the compensation is optimal with

$$\Delta f \approx \frac{1}{RC_s}. \tag{5.5}$$

Thus, it is important to make C_s small to achieve a large bandwidth. As discussed earlier when designing coaxial couplers, it is also important to suppress coupling to the fundamental mode as much as possible. This can be achieved by adding a parallel LC filter where L_f and C_f are tuned to the fundamental mode frequency.

Currently, two designs have been proposed. An antenna style coupler which based on the successful Tesla style coupler [63] . This design [64] is based on

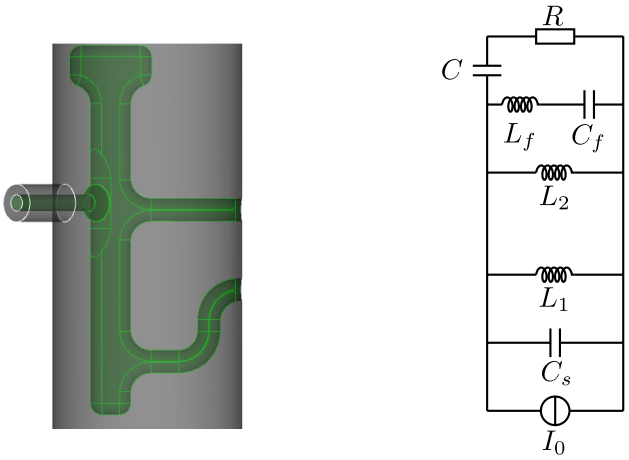

Figure 5.2: The CAD model and equivalent circuit mode for the Tesla design.

the coupler used in SNS but rescaled such that the fundamental mode filter is tuned to 704 MHz. The CAD model and equivalent circuit is shown in Figure 5.2. In this case, the coupler is supported by two inductive stubs L_1 and L_2 which provides a stiff design as well as creating a loop in which liquid helium can easily be passed along to provide an excellent method of cooling. Above the L_2, the fundamental model filter is determined by a coaxial resonator which can be tuned by modifying the gap between the inner conductor and the top of the coupler vacuum vessel.

The other design is a hook style coupler designed by Rostock University [65] and is similar to that used at LEP. The CAD model and equivalent circuit is shown in Figure 5.3. The coupler is supported by only one inductive stub L_2 making the coupler more sensitive to mechanical vibrations and makes cooling more difficult without a loop. The fundamental mode filter is controlled using the hook at the bottom of the coupler. The filter is tuned by rotating in the coupler inside the coupler vacuum vessel. This coupler was designed for the SPL specifications which has a vacuum vessel with a diameter of 36 mm compared to the tesla style which had a diameter of 56 mm. This placed a limitation on the radius of the hook limiting the size the L_f. Also, if the gap between the outer wall and the hook is too small, the coupler becomes very sensitive to errors. To account for this, a large capacitive plate was added to

give the gap an acceptable distance.

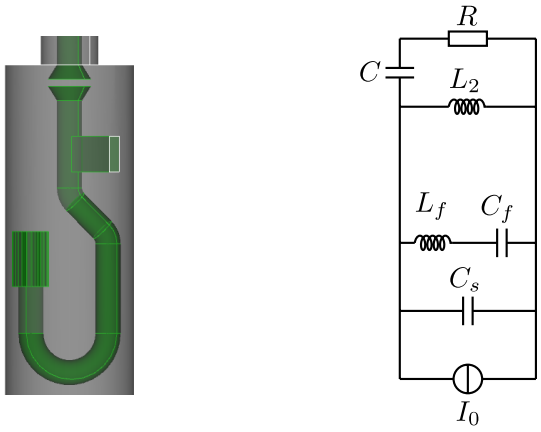

Figure 5.3: The CAD model and equivalent circuit mode for the hook design.

It has been observed [66] in the superconducting linac of the Spallation Neutron Source (SNS) that couplers installed to remove the HOM power excited by the beam have been the source of many problems, and the evidence points to field emission (FE) and multipacting as the primary causes of these issues [67].

5.2 Field Emission

Field emission is the emission of electrons from the cavity surface in regions of high electric field. Emission occurs from particular spots known as emitters which are located in high electric field regions. The basic theory follows, that electrons inside a metal are confined inside a potential well such that the electrons fill the energy levels of the conduction band, up to the Fermi level ε_f. In normal circumstances, the electron is unable to escape due to insufficient energy. Additional energy, as given by the work function ϕ, is required for the electron to escape which usually comes in the form of thermal energy or radiation energy.

Using the quantum mechanical picture, the wave-function of the electron will decay rapidly outside of the well however, if the well is thin enough there

is a finite possibility that some electrons can tunnel through and escape the metal.

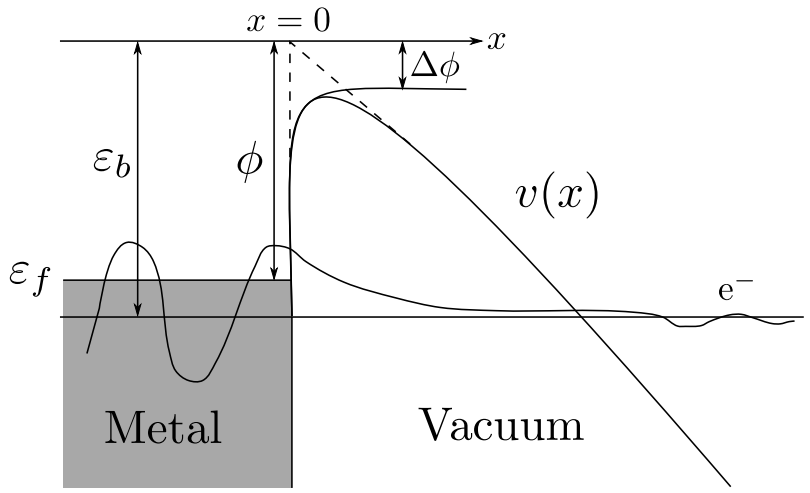

Figure 5.4: Schematic drawing of electrostatic potential at a metal surface. If an electric field is applied the well becomes triangular.

Fowler and Nordheim (FN) [68] showed that when a electric field is applied, the resulting potential $v(x)$ barrier becomes triangular allowing electrons to tunnel through increasing the probability an electron can tunnel out of the well. Figure 5.4 shows a potential well in the with and without an external electric field.

Fowler and Nordheim developed a theory to predict the current from an emitter however, a comparison between experiment shows the FN prediction underestimates the current substantially. The excess is attributed to a field enhancement factor β_{FN} which is thought to be directly related to the emitter itself. The current was modified to include this enhancement factor as is given by

$$I(E) = \frac{AA_e(\beta_{FN}E)^2}{\phi} \exp\left(-\frac{B\phi^{3/2}}{\beta_{FN}E}\right), \tag{5.6}$$

where A_e is the effective emitting area, E is the instantaneous electric field and A and B are constants. As electrons are emitted they will take different trajectories which are determined by the phase of the rf period. It is possible that

some electrons will be captured by the accelerating field and traverse the entire structure. They may also strike devices such as the couplers. A large fraction of the electrons will also be steered the magnetic field and strike the wall from which the emission originates producing heat and bremstrahlung x-rays. Field emission is one of the primary initiating mechanisms of multipacting, which will be described in the following section.

5.3 Multipacting

Multipacting is a resonant process which can lead to an electron avalanche in rf structures. The huge number of electrons will absorb rf power limiting the performance of the structure and result in large temperature rises when the electrons collide with the structure walls.

The basic concept of multipacting is when electrons are emitted from the structure's surface, it is accelerated by the electromagnetic fields and will eventually impact the surface again leading to the production of a secondary electrons. The number of secondary electrons produced depends on the characteristics of the surface and the impact energy of the initial electron. This process will repeat causing an exponential increase in the number of electrons if specific resonance conditions are satisfied.

The onset of multipacting is usually observed when the field level remains constant even as more rf power is supplied effectively reducing the Q_0 at a particular threshold. In most cases, a multipacting barrier can be overcome by processing. This is done by allowing the the multipacting to occur for several minutes while the rf power is slowly increased. Eventually, the Q_0 improves and the multipacting stops. Typically, many multipacting barriers appear at higher fields however these may be processed also. These barriers are referred to as soft barriers as they can be processed however some barriers can not be overcome and are known as hard barriers. Figure 5.5 which is adapted from [69] shows Q_0 versus field gradient curve when raising fields in the cavity for the first time. Provided the cavity is kept under vacuum, the soft barriers will not reappear.

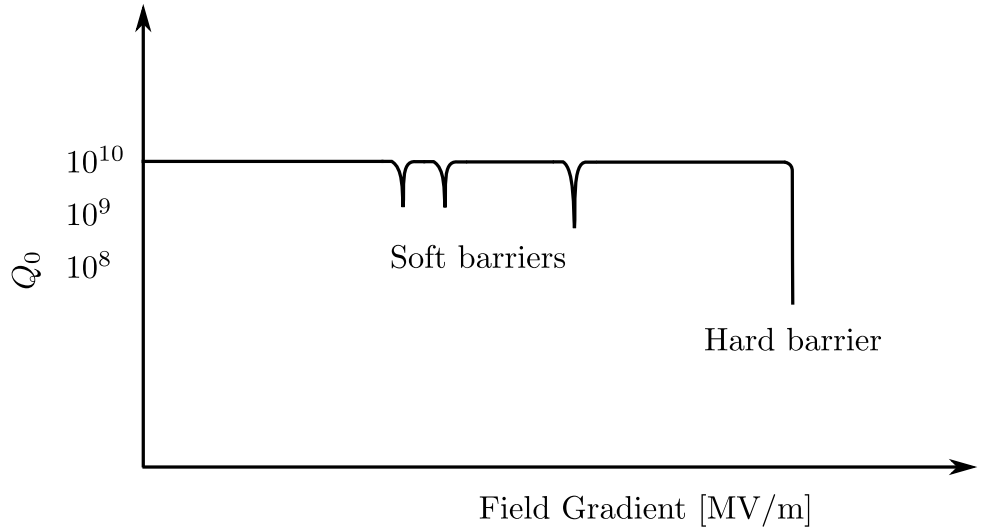

Figure 5.5: Q_0 versus E curve for a SRF cavity showing several multipacting barriers when the fields are raised for the first time.

5.3.1 Secondary Electrons

The number of secondary electrons emitted is given by the secondary electron yield $\delta(K)$ of a material which is measured experimentally. It describes the number of electrons that are emitted due to a impact of energy K. A typical SEY for Niobium is shown in Figure 5.6.

The number of electrons N_e emitted at the kth impact is given by

$$N_e = N_0 \prod_{m=1}^{k} \delta(K_m), \tag{5.7}$$

where N_0 is the number of electrons emitted initially from a unique position and K_m is the kinetic energy at the mth impact. Multipacting occurs when $N_e \to \infty$ as $k \to \infty$.

5.3.2 One-Point Multipacting

One-point multipacting is when electrons impact the structure wall at, or very close to where the electron was originally emitted from. The electrons are

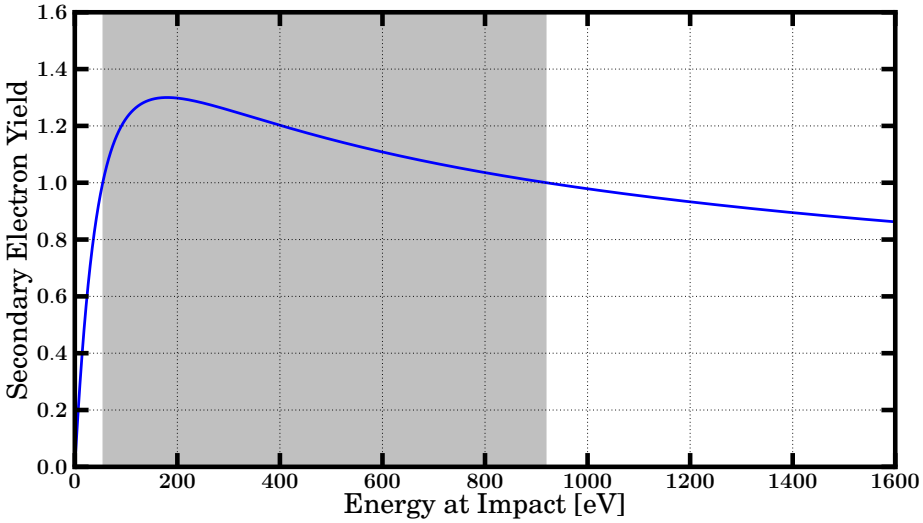

Figure 5.6: Typical SEY data for Niobium. The shaded region shows the energy region where the SEY > 1.

primarily accelerated by the electric field perpendicular to the surface while, at the same time, the magnetic field close to the surface forces the electrons along a quasi-cyclotron orbit. The number of rf periods it takes for the electron to return to its emission site is denoted by the multipacting order. Example trajectories of order one, two and three are showing in Figure 5.7. Assuming a simple cyclotron orbit, the orbit frequency scales as

$$\omega_c \propto \frac{eB}{m}, \tag{5.8}$$

where e and m are the charge and mass of the electron respectively and B is the local magnetic field. For multipacting of order n to occur, the drive frequency of the cavity ω_g is an integer multiple of the orbit frequency ω_c. Thus, the fields at which multipacting can occur scale as

$$B_n \propto \frac{m\omega_g}{ne}. \tag{5.9}$$

Thus an infinite number of multipacting barriers are predicted up to to the maximum allowable field however for a barrier to actually occur, it is also required that $\delta(K) > 1$ for the impact energy. Therefore, in order for a

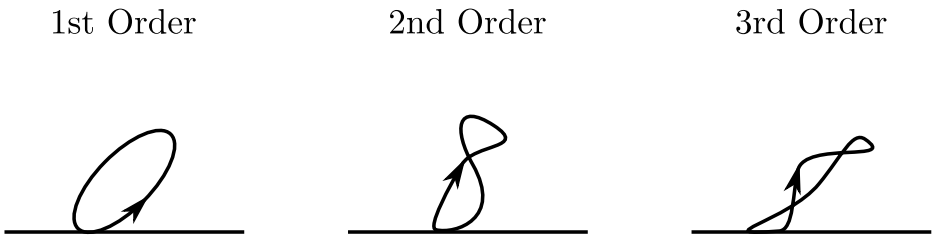

Figure 5.7: Example one-point multipacting trajectories for first, second and third order multipacting.

resonance to occur, the rf period must be an integer multiple of the cyclotron period and the secondary electron yield must be greater than 1.

The elliptical shape of the accelerating cavities was implemented to reduce the onset of one-point multipacting. The shape means the magnetic field varies along the cavity wall resulting in no stable trajectories. The electrons will drift towards to cavity equator where $E_\perp$ is so small, secondary electrons do not gain enough energy to produce an avalanche.

5.3.3 Two-Point Multipacting

Two-point multipacting is when the electron trajectory includes two impact sites which are usually opposite a symmetry plane. The condition for resonance requires that the time between impacts is a half-integer multiple of the rf period.

Two-point multipacting can be treated analytically but considering a parallel plate capacitor as shown in Figure 5.8 which is adapted from [69]. Ignoring fringe fields, the electric field is given by $E_0 \sin(\omega_g t)\hat{x}$ where $E_0 = v/d$. V is the applied voltage between the plates and d is the plate separation. At a time $t = 0$, the acceleration of the electron emitted from the right plate at a phase φ_0 is given by

$$\mathbf{a}(t) = -\frac{eE_0}{m} \sin(\omega_g t + \varphi_0)\hat{x}. \tag{5.10}$$

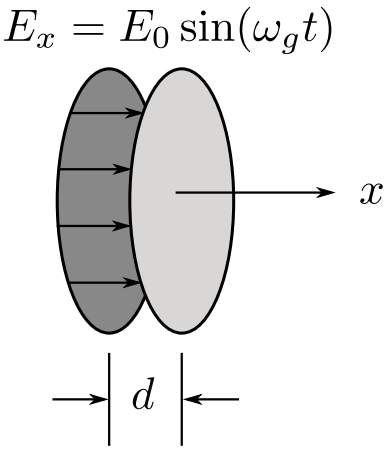

Figure 5.8: Parallel plate description of two-point multipacting where the right place is at $x = 0$.

The electron's position at time t can be found by integrating (5.10) twice and imposing the initial condition that $x_0 = 0$.

$$x(t) = \frac{eE_0}{\omega_g^2 m}\left[\sin(\omega_g t + \varphi_0) - \sin\varphi_0\right] - \frac{eE_0}{\omega_g m} t\cos\varphi_0. \tag{5.11}$$

If the case when φ_0 is considered, i.e. when the electric field begins to point in the $+\hat{x}$ direction then (5.11) simplifies to

$$x(t) = \frac{eE_0}{\omega_g^2 m}(\sin\omega_g t - \omega_g t). \tag{5.12}$$

Thus, the electron will drift across the gap following an oscillatory motion. Given that the resonant condition for multipacting requires that the electron traverse the gap in an half-interger period. Then

$$x\left(t = \frac{[2n-1]\pi}{\omega_g}\right) = -\frac{(2n-1)\pi eE_0}{\omega_g^2 m} = -d. \tag{5.13}$$

Therefore, the gap voltage at which two-point multipacting of order n can occur is given by

$$V_n = E_0 d = \frac{d^2 \omega_g^2 m}{(2n-1)\pi e}. \tag{5.14}$$

Unfortunately, in reality, most structures are too complicated to use the analytical approach and numerical methods are required. However, the analytical approach is useful to understand the basic mechanism.

Inside the cavity itself, two-point multipacting is rare because the distance between walls is so large, the energy at impact to too large to produce a secondary electron. However, in other rf components such as coaxial line or couplers, two-point multipacting is much more common due to the small gaps between surfaces.

5.4 Track3P Simulation

One concern in using HOM couplers is that a multipacting region will develop for a particular accelerating gradient, causing the quality factor, Q_0, of the cavity to drop below the desired level. Alternatively, MP causing large amounts of energy being lost in the walls of the coupler leading to thermal deformation [70] and a detuning of the notch. Another concern is that arcing in the coupler can cause the HOM filter to short and therefore removing the bandstop filter. Such detuning or arcing may lead to excessive amounts of the fundamental mode being coupled out of the cavity, thus dropping the Q, and risking damage to the HOM monitoring electronics. As mentioned previously, it was found that in the superconducting linac of the Spallation Neutron Source (SNS) that HOM couplers have been the source of many problems [66] and have since been removed.

Therefore, multipacting simulations are performed on both potential coupler designs in order to determine the safest design. Multipacting simulations were performed using the Track3P code [71] from the ACE3P suite. Track3P has been successfully used to predict multipacting in real devices [72]. In order to allow proper calculation of field gradient, each coupler CAD model was attached to a SPL cavity design. Initially, it was decided to modify the cavity design to reduce the total number of cells from five to two in order to reduce

the model size with the hope of reducing the CPU cost of the multipacting simulation. However, it was later discovered that simulation was performed on a localised part of the mesh where the particles existed so reducing the number of the cells had very little effect. All simulations were performed with two cell cavities in order to maintain consistency.

Once the mesh was prepared, an eigenmode simulation was performed using Omega3P in order to obtain the drive fields needed for the multipacting simulation. Track3P was then used to track the particles through these fields and determine if multipacting could be a problem.

To begin a Track3P simulation, a bounding box must be specified in order to determine the sites of the initial electron emission. Once the box is defined, a particle will be emitted at the centre of every surface mesh face inside the bounding box. Thus, the number of initial particles in a particular region can be controlled by altering the mesh density in that region. Once the simulation begins, a particle is emitted with an energy of 2 eV every 100th of a rf cycle for one cycle i.e. every 3.6° of the RF phase. After one rf cycle, these particles are then tracked until the total number of rf cycles specified by the user is reached which in this case is 20 rf cycles.

During the simulation, if a particle impacts a surface and the phase conditions are correct, another particle will be emitted with an energy of 2 eV with a direction perpendicular to the impact surface. If a particle survives more than four impacts, it is classed as a resonant particle. In this case, the initial position, position of impact, impact phase and impact energy are recorded and saved. This mode presents some concerns is the fact that the electrons are always emitted normally to the emitting surface, instead of using a statistical range of emission angles [73]. Such a range may cause resonant trajectories to be diluted by the non- zero chance than an emitted electron will not return to the initial site.

The simulation model used in Track3P does not include secondary electrons, and so a post-processing step using the enhanced counter function is needed in order to predict the scale of multipacting. The enhanced counter function shows the total number of secondary electrons at the end of the simulation normalised by the initial number of electrons.

$$ECF = \frac{1}{N_i}\sum_{n=1}^{N_i} N_{e,n} = \frac{1}{N_i}\sum_{n=1}^{N_i}\prod_{m=1}^{k}\delta(K_{m,n}), \tag{5.15}$$

where N_i is the total number of initial particles tracked, $N_{e,n}$ is the total number of electrons emitted by the nth particle after m impacts. Therefore, of concern are field gradients in which the enhanced counter function is greater than unity as this predicts that the number of particles are increasing.

For the simulations of the two HOM couplers, each coupler was split into 6 regions where each region defines the bounding box used for the initial emission sites. This was to allow a simpler analysis of the post-processing output. Figure 5.9 shows both couplers split into the six regions.

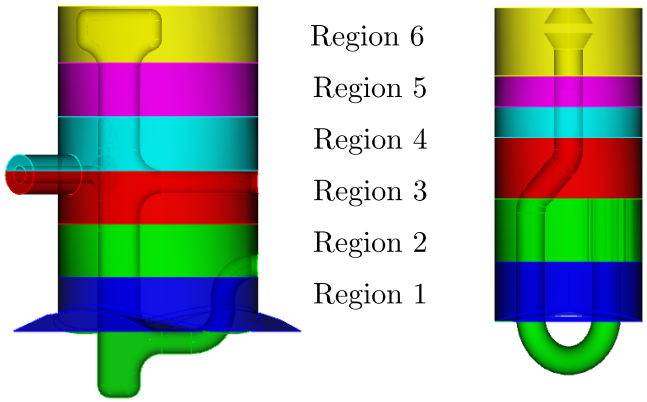

Figure 5.9: Both coupler designs showing the six regions which defined the bounding boxes used for the initial emission sites in Track3P simulation.

Each region contained around 150-200 initial emission sites and thus emitting every 3.6° for one RF cycle, 150,000-200,000 particles are tracked in each region for a single field gradient. 125 field gradients were scanned from 0.2 MV/m up to 25 MV/m in steps of 0.2 MV/m. The results of the simulations are presented in the following subsections.

5.4.1 Multipacting in Tesla style design

Due to the fact no previous studies were performed on this design with regards to its position and orientation, a study was carried out to find which rotation

resulted in the best performance and kept the notch at 704 MHz. It is important that the notch remains at 704 MHz for the simulations otherwise this will effect the drive fields used for multipacting simulation . A course scan was performed from 0.3 GHz to 1.3GHz then combined with a finer scan from 0.7 to 0.72 GHz. The design with the notch closest to 704 MHz was chosen.

With the orientation now set, multipacting simulations can be performed as described in the previous section. Figure 5.10 shows the impact energy of resonant particles as each field gradient scanned. The shaded blue region represents the energy range for which the typical secondary electron yield of Niobium is greater than unity and thus the region in which impacts are of most concern.

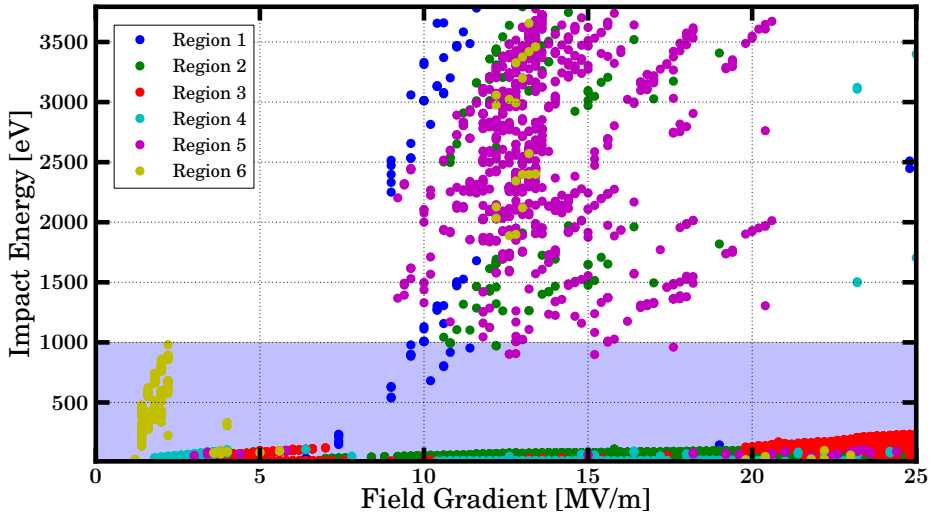

Figure 5.10: The impact energy of each resonant particles for various field gradients for the Tesla design. Impacts inside the shaded region are considered dangerous as the SEY$>$ 1 here.

The impacts locations of these resonant particles are shown in Figure 5.11. Figure 5.12 shows the enhanced counter function calculated using the typical SEY data shown in Figure 5.6.

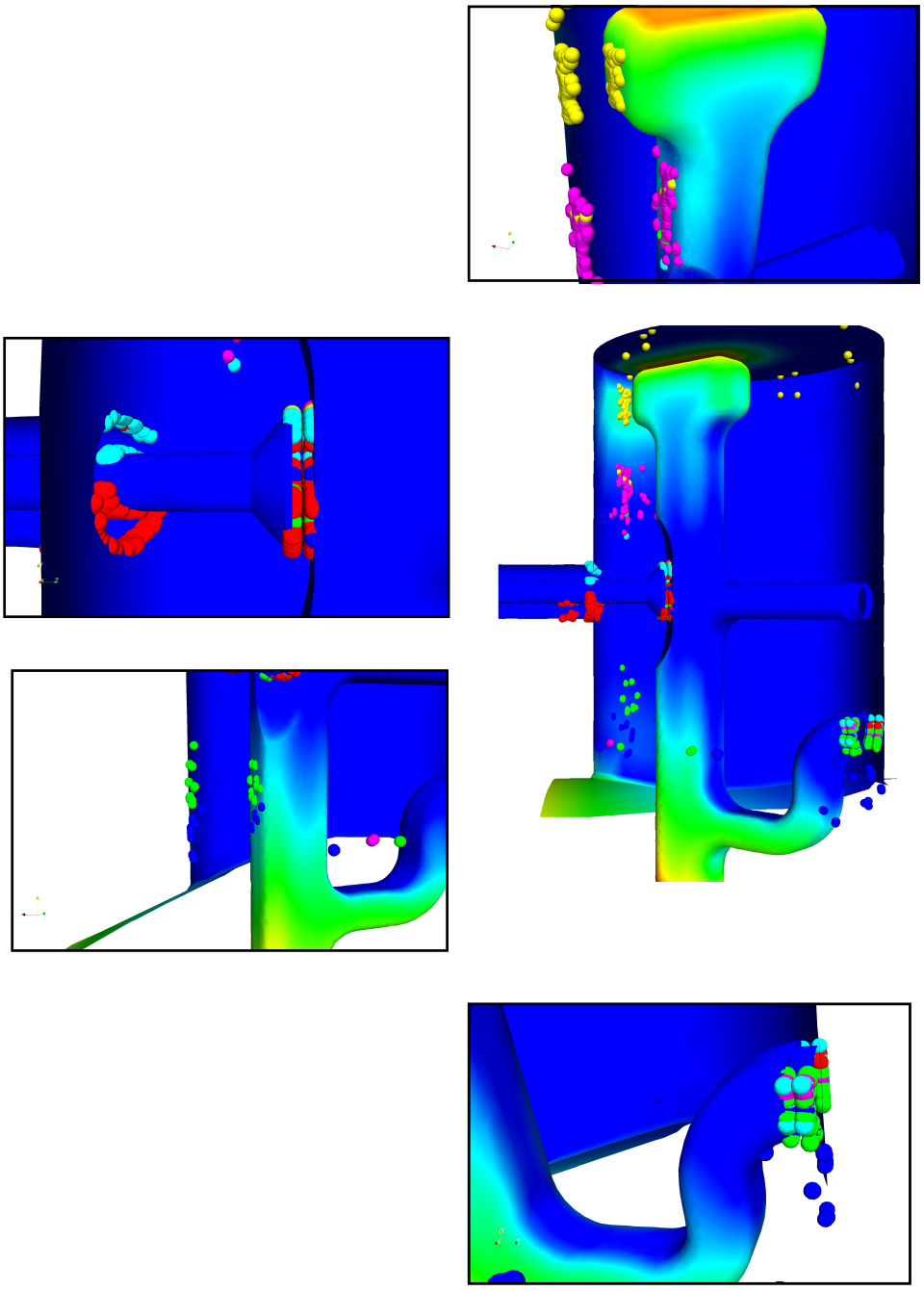

Figure 5.11: The location of resonant impacts inside the Tesla coupler. The coloured spheres show the locations for different regions.

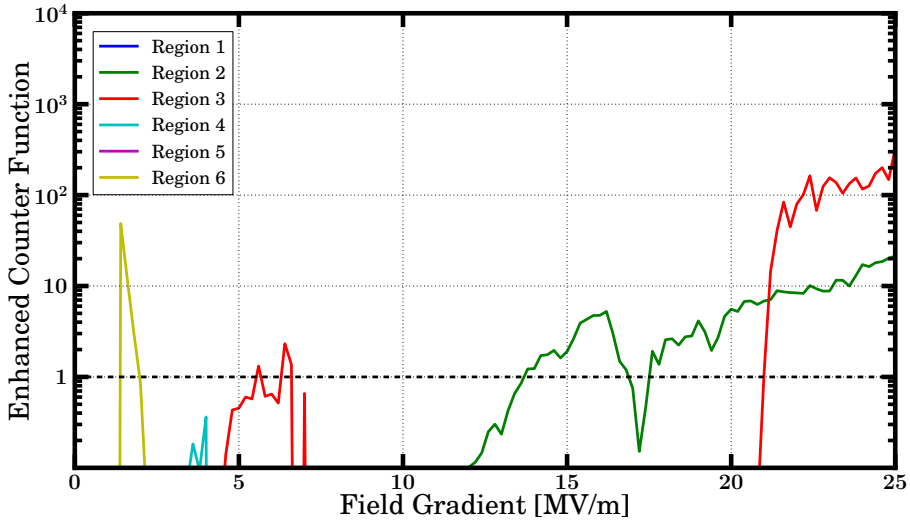

Figure 5.12: The enhanced counter function for the Tesla design. Regions where the ECF is greater than 1 are considered dangerous.

The majority of the resonant particles represent 2-point multipacting in which the electrons travel back and forth between the outer wall of the coupler and the inner conductor. Region 1 shows very little activity with impacts concentrated around the gap between the outer wall and the lower leg of the inner conductor. Region 2 shows a much higher number of resonances across a large field gradient range starting from around 9 MV/m up until 25 MV/m. The impacts occur in the small gap where the lower leg joins to the outer wall. The large bands are visible from 13-16 MV/m and and larger a band between 18-25 MV/m. Region 3 relates to impacts at the coaxial feedthrough and results in dangerous resonances around 6 MV/m and also a large band from 21-25 MV/m. Region 4 also shows some resonances at the coaxial feedthrough but to a much smaller degree than Region 3. Region 5 shows a lot of resonant impacts however most of them occur at higher energies due to the large distance between the inner conductor and outer wall and are not though to be dangerous. Finally, Region 6 shows resonances at the top of the inner conductor where it becomes wider. This results in a narrow band at low field gradient which could be problematic.

5.4.2 Multipacting in Hook Design

Figure 5.13 shows the impact energies versus field gradient for resonant particles. Again, the shaded region represents the typical energy range where the SEY for niobium is greater than one and therefore, where avalanche effects may occur. The majority of the impacts are caused by two point multipacting of order one between the coupler wall and the large capacitive plate located in region 2. There also exists some multipacting events in region 6 at the gap between the feedthrough and the central conductor as shown in Figure 5.14 however from the enhanced counter function shown in Figure 5.15, it can be seen that this is expected to cause no serious problems and the main concern is the narrow band between 0.4 MV/m and 0.8 MV/m which is almost a factor of 100 stronger compared to any band in the Tesla design.

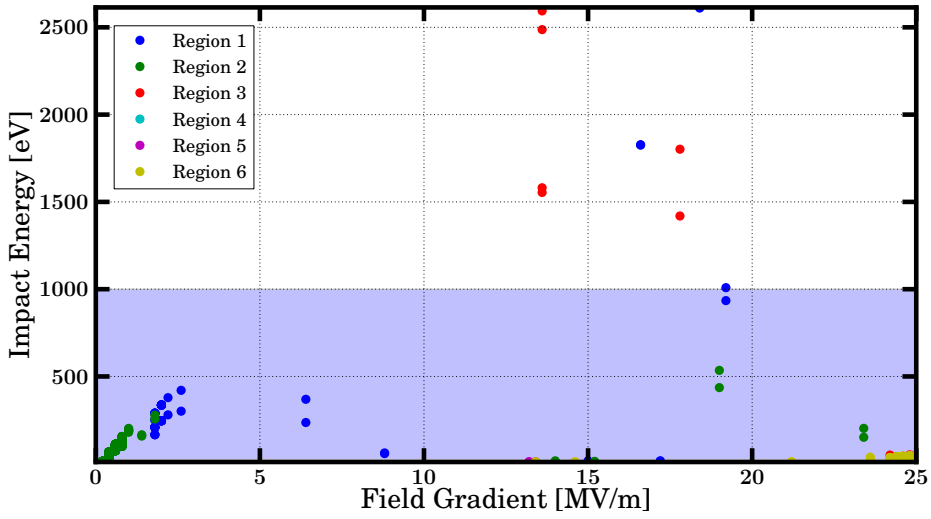

Figure 5.13: The impact energy of each resonant particles for various field gradients for the hook design. Impacts inside the shaded region are considered dangerous as the SEY$>$ 1 here.

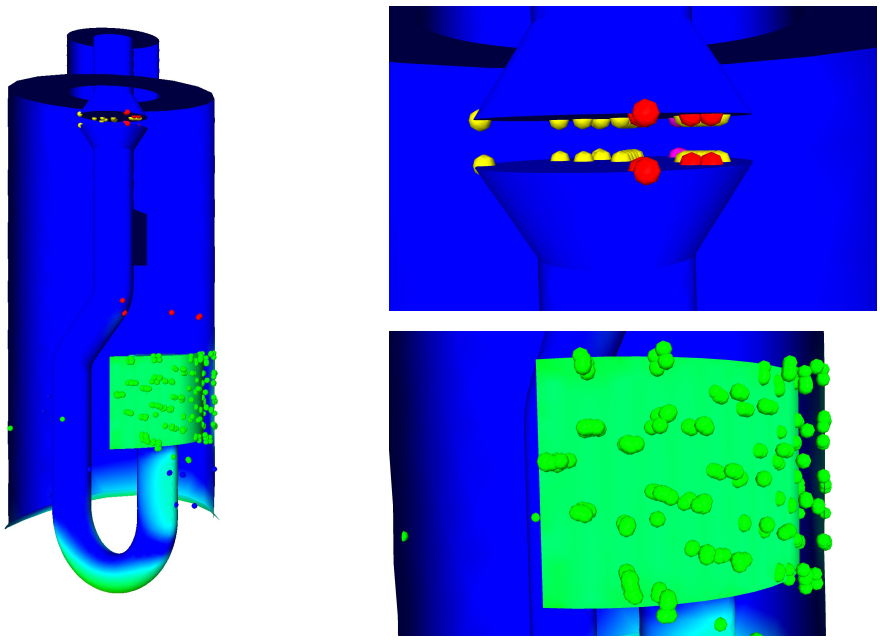

Figure 5.14: The location of resonant impacts inside the hook coupler. The coloured spheres show the locations for different regions.

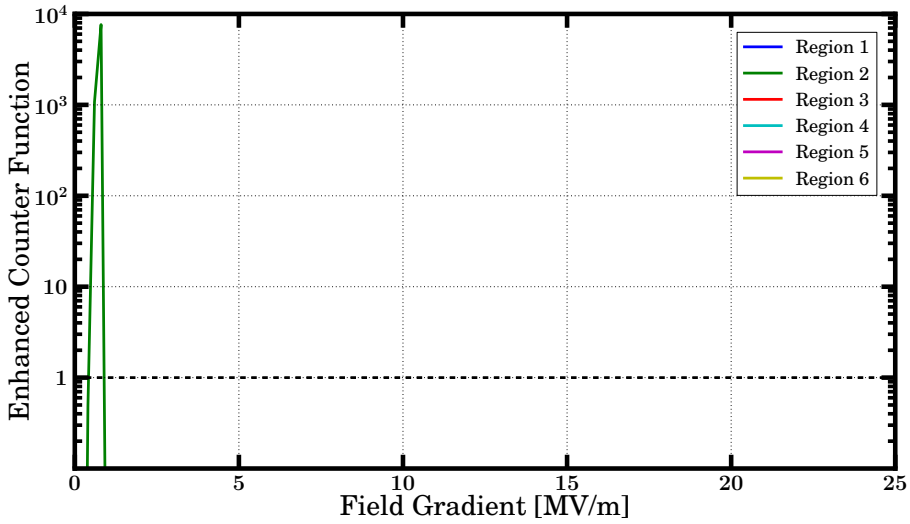

Figure 5.15: The enhanced counter function for the hook design. Regions where the ECF is greater than 1 are considered dangerous.

5.5 Modifications

Simulations of both coupler designs showed multipacting activity which could cause problems. The hook style design showed very little activity compared to the Tesla style design however, it also showed the most dangerous band due to the large capacitive plate.

Both designs were then modified in an attempt to reduce the possibility of resonant trajectories and also improve their transmission properties. The following subsection describes the alterations made to the coupler designs, and the resulting effect on their performance.

5.5.1 Higher-order circuits

One concern for cavities similar to the ESS and SPL designs is the frequency separation between the accelerating mode and the first Higher Order Mode which which occurs at a frequency of around 900 MHz. It is desirable to try to increase the transmission at this frequency, therefore, a much steeper transition from the notch at 704 MHz to this frequency of 900 MHz is required. One possible method is to use a higher-order circuit approach [74]. Consider a Butterworth filter, a filter designed to have a passband as flat as possible. Figure 5.16 shows a filter with n capacitive and inductive elements as well as the frequency response for increasing number of elements. It can be seen that for $n \to \infty$, the frequency response tends to the ideal case where the gain=1 for $\omega \leq 1$ and gain=0 for $\omega > 1$. Thus, by increasing the number of inductive and capacitive elements in the circuit, the transition from the passband to the stop-band can be increased. This method can be employed in couplers to allow increased damping closer to the notch.

5.5.2 Modified Tesla design

Before focusing on modifying the transmission properties, attempts were made to reduce the MP activity. The Tesla design showed MP regions on the flat surfaces of the inner conductor that were closest to the outer wall, in particular at the top where the size is increased and also between the wall and the bottom

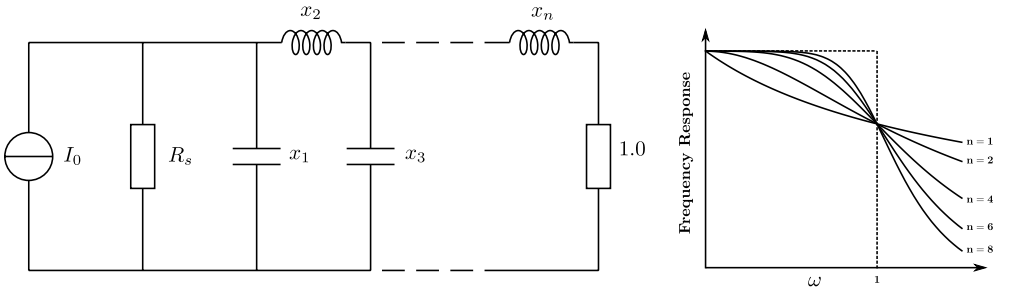

Figure 5.16: A circuit model of a nth order circuit and the associated frequency response for increasing order.

leg. The first modification involved rounding the majority of these flat surfaces. Rounding all the surfaces altered the LC characteristics of coupler and thus, the height of the coupler was increased in order to account for this and retune the notch back to 704 MHz. Once re-tuned, a Track3p simulation was repeated as before. The results are shown in Figure 5.17.

In comparison to Figure 5.10, it can be seen that there is a huge reduction in the number of resonant trajectories in particular at the top of the coupler (Top) where only 6 resonant particles were found and only half of these inside the dangerous SEY region.

A majority of the trajectories were between the outer wall of the coupler and the bottom leg joint (Join) which involves a 90° step. In further iterations this join was smoothed which easily suppressed persistent trajectories.

Trajectories also existed at the feedthrough (Coax) which was to be expected due to capacitive coupling here. The feed though plate was replaced with a concave surface to help minimise resonant trajectories.

The most problematic region was between the outer wall and the bottom leg (Leg-wall gap) just below the joint. Although the number of trajectories is lower than at the join, removing these is much trickier. Solutions would be to reduce the radius of the leg further however making it more difficult to tune notch back or remove the bend in the this leg thereby changing the transmission properties.

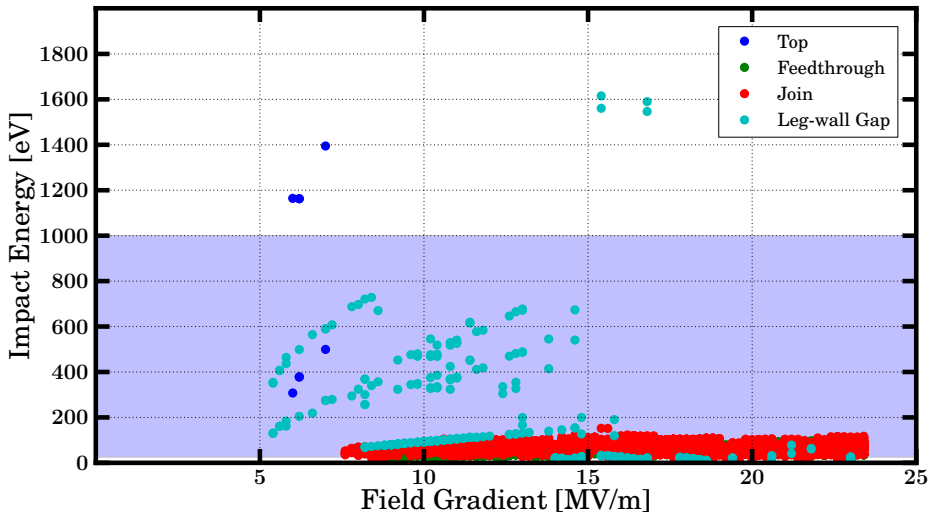

Figure 5.17: The impact energy of each resonant particles for various field gradients for the modified Tesla design. Impacts inside the shaded region are considered dangerous as the SEY>1 here.

The main focus for optimising the transmission properties was for the S21 to rise as steeply as possible after the notch in order to damp the first dipole band which typically starts at 900 MHz. Modifying the existing geometry had small changes on this rise and it was determined that the rotation with respect to cavity the had the largest effect. In order to increase the damping at lower frequencies, the bandwidth of the notch must be reduced and therefore the size of minimum electric field at the feedthrough.

It may be possible to improve the transmission further by adding additional elements to the geometry but it is highly desired to keep the coupler design simple and small. A simple method to improve the transmission properties would be to change the diameter of the coupler however, the couplers were designed with a dimensional constraint of 50 mm for the diameter. The final design is shown in Figure 5.18.

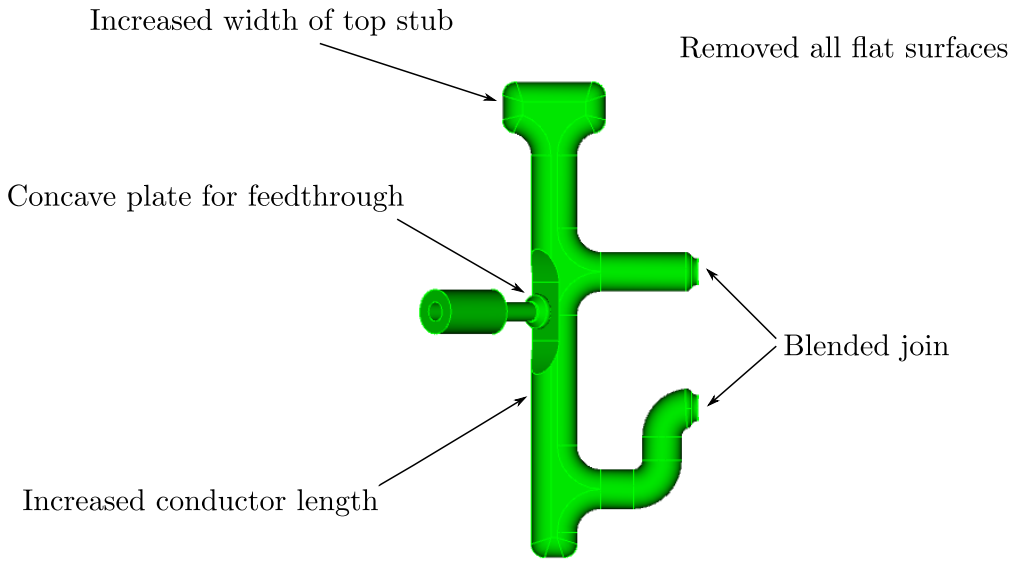

Figure 5.18: Final modified tesla design.

5.5.3 Modified hook design

The hook design suffered from a severe MP band at low field gradients between the large capacitive plate and the outer wall of the coupler. In an effort to reduce the dangerous trajectories in this region, ridges were added to the capacitive plate as previous efforts for power couplers had been successful [75]. Figure 5.19 shows two designs in which ridges were included along with the original. The enhanced counter function at low field levels is also shown. The "Ridges 1" design results in a lower maximum of the enhanced counter however it also broadens the field level band at which is occurs. "Ridges 2" performed poorly and increased the level of the MP activity. Thus, is was decided the best option was to attempt to remove the capacitive plate completely.

In order to keep the notch at 704 MHz, the loss of capacitance due to removal of the plate needed to be accounted for elsewhere. The simplest method is to increase the radius of the hook. However this places the hook very close to the outer wall, making the transmission very sensitive to errors.

Adding an extra inductive post to the feedthrough results in a higher order

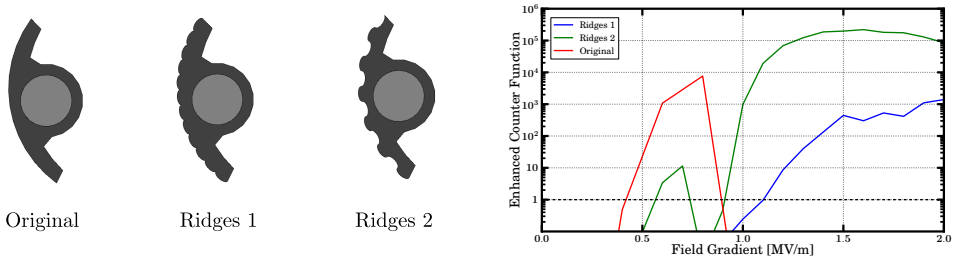

Figure 5.19: Modified capacitive plate to include ridges (left). The enhanced counter function for each design.

circuit with a double-notch effect as used in a BNL design [76]. This effectively increases the bandwidth reducing sensitivity. The position of the inductive post on the other side of the capacitive element also improves the high pass filter properties of the coupler resulting in the transmission curve rising much faster allowing better damping of the first dipole band which typically starts at 900 MHz. The final design is shown in Figure 5.20.

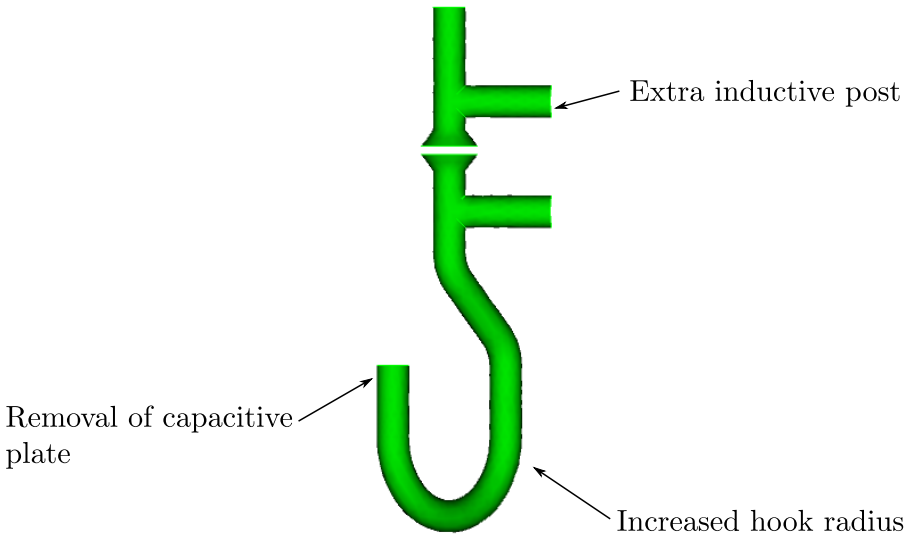

Figure 5.20: Final modified hook design.

Figure 5.21 shows the designs susceptibility to multipacting. It can be seen

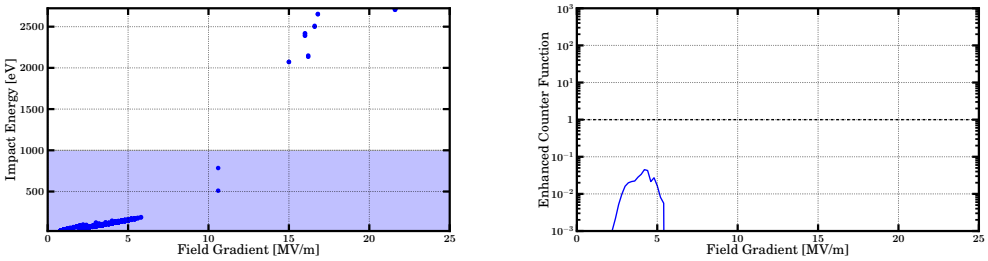

Figure 5.21: The impact energy of each resonant particles for various field gradients for the modified hook design. Impacts inside the shaded region are considered dangerous as the SEY$>$ 1 here. (left) and the enhanced counter function (right).

from enhanced counter function that while a multipacting band is present is below the threshold of unity and thus expected to be processed easily.

5.5.4 Comparison

Modification to both the Tesla style and the hook style coupler show a reduction in problematic resonant MP trajectories. A comparison of their transmission properties is shown in Figure 5.22 where the dashed line represents the location of the accelerating mode. The modified hook design appears to be the more desirable coupler due to its wider effective bandwidth provided by the double notch with the transmission remaining below -80 dB for $\pm$ 50 MHz around the accelerating mode. Therefore, a massive shift in the notch position would be required for problems to occur such as power from the accelerating mode being coupled out.

The hook design also provides higher damping at lower frequencies. One disadvantage is that this design is more susceptible to vibration resonances due to its single connection to the outer wall by one post however the advantage of this is that with no fixed point lower down, the coupler can be demounted from the cavity. The inclusion of the extra inductive post also increases the fabrication complexity. Further optimisation is necessary to provide easier tunability of the coupler and improve the mechanical properties. The Tesla

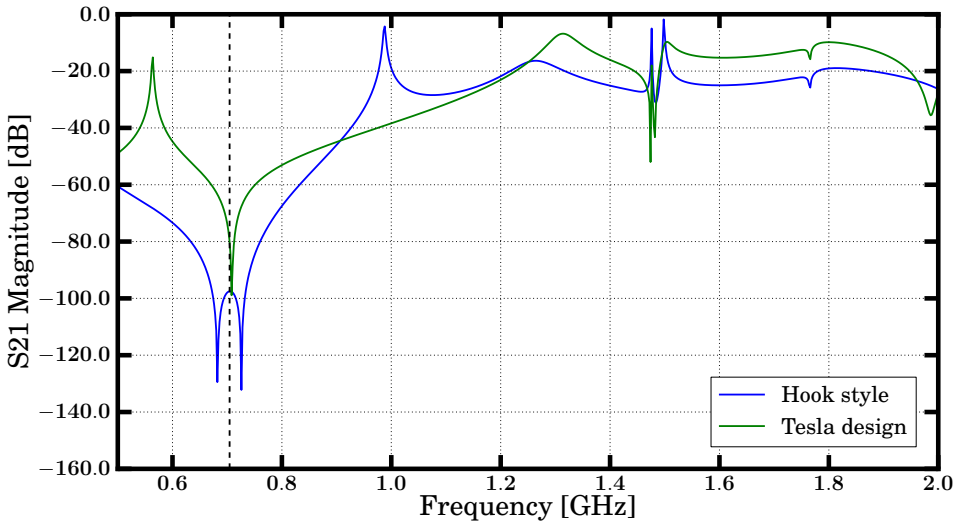

Figure 5.22: The S21 for both couplers as excited by a TM_{01} mode.

design is stiffer due to its welded joints and also easier to cool with the two legs providing a closed loop to pass liquid helium through.

Following on from these investigations, if a coupler is required eventually for the ESS cavities, the hook design provide the best transmission properties along with the least technical risk from multipacting. The hook design is expected to be harder to fabricate and more sensitive to mechanical effects however these are believed to be less important than the transmission properties and sensitivity to multipacting.

Chapter 6

Conclusions

The work in this thesis was motivated to find the answer to two problems relating to Higher Order Modes in High Power Proton linacs relying on superconducting technology. Firstly, the question of whether or not additional HOM damping measures are required for the ESS SRF linac and secondly, if couplers are required, how to provide a design that can reduce the significant technical risks associated with using them. To tackle these problems, large scale simulations were performed on prototype cavity and coupler designs and a dedicated code for simulating the influence of parasitic resonances on the beam was developed.

Simulations were performed on prototype cavity designs highlighting dangerous modes. In addition, large scale simulations involving a string of four cavities were performed to determine the level of coupling between them. It was found that the inclusion of a taper in the cavity design provides little benefit in terms of reduction of coupling particularly for the accelerating mode and thus, are not required unless for other uses such as the reduction in dark current.

The code "HOMDynamics" was used to determined if the ESS SRF linac required HOM dampers and whether the velocity partitioning need to be changed if the effect from SOMs was too high. Of particular focus, was dealing with quasi-relativistic beams and studying the errors from the rf system or input noise. The code was successfully benchmarked against other codes. Simulations were performed initially focusing on the SOMs in different lattice designs

for the linac. It was found that it is possible to design a linac susceptible to SOMs however the latest baseline linac for ESS shows no serious problems below 100 mA; a current well above the design value. This is shown in Figure 6.1. Thus, although there are points are along the linac where the SOMs will have a larger coupling to the beam than the accelerating mode, no change is required to the geometric beta of the cavities or to the velocity partitioning.

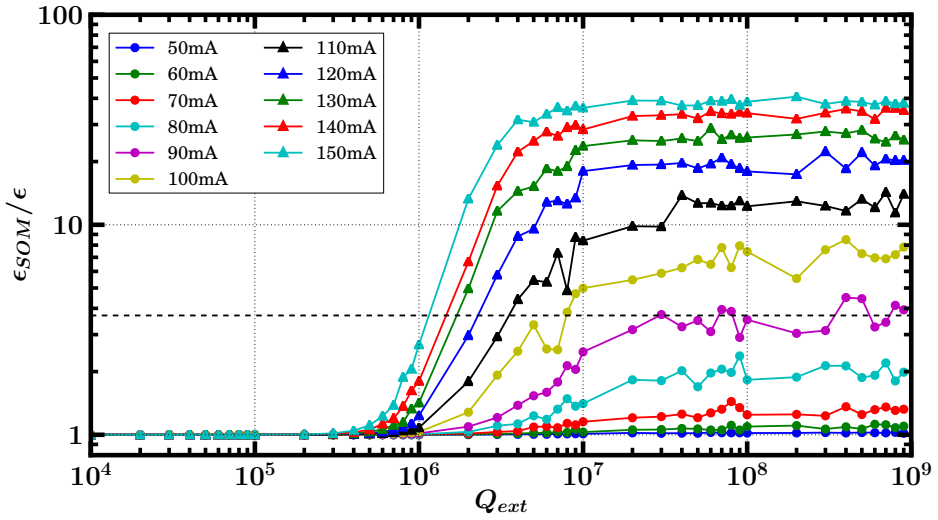

Figure 6.1: The average longitudinal phase space increase for 100 linacs at varying currents and Q_{ext} of the SOMs.

Simulations were then performed in both the longitudinal and transverse plane studying the influence of HOMs on the baseline linac design. It was found that dipole modes pose no serious problem for proton linacs which is in good agreement with previous studies. The longitudinal plane is much more important for protons due to the quasi-relativistic nature of the beam. The influence of injection noise, HOM frequency spread, RF errors and machine lines were all investigated as function of beam current and HOM damping. It was found that HOMs are of little concern if they lie far enough away from a machine line. It was determined that for dangerous modes in ESS, dedicated HOM damping is not required as long as they lie at least 3 MHz from a machine

line. Both results can be seen in Figure 6.2. Therefore, HOM dampers have been removed from the ESS baseline design. However, it should be noted this will limit the future flexibility of the machine as no fast chopping schemes can be used. The results found in this thesis agree with the growing trend that HOM couplers are not required for high power proton machines such as at SNS and Project X.

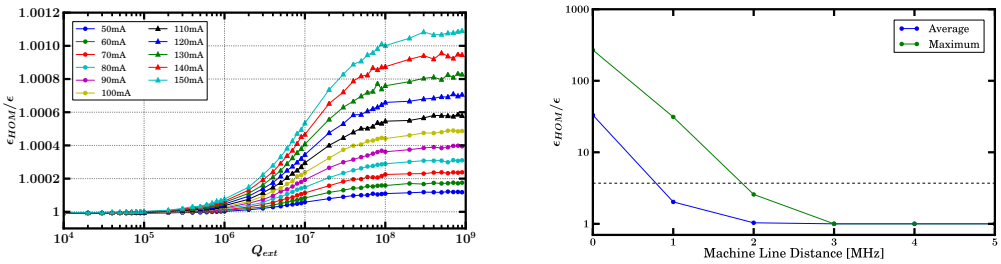

Figure 6.2: The average longitudinal phase space increase for 100 linacs at varying currents and Q_{ext} of the HOMs (left). The average and maximum longitudinal phase space growth as a function of the distance a HOM is from a machine line (right).

Two potential HOM coupler designs for cavities resonating at 704 MHz were simulated to determine their susceptibility to multipacting. Both designs showed regions where multipacting was predicted to be very strong. Both designs were then modified to reduce resonant trajectories and also improved the transmission properties. The most promising design was based on a hook design with an extra inductive post. The extra inductor produced a double notch effect providing a larger bandwidth for the notch filter while allowing high damping at frequencies much closer to the accelerating mode. This design also showed the least sign of dangerous trajectories which could lead to multipacting. While this design will not currently be used for the ESS cavities, it has the possibility to be slightly modified and used in other machines, specifically the SPL cavities at CERN or even cavities operating at different frequencies if the coupler is scaled correctly. The final modified coupler designs along with their associated S21, are shown in Figure 6.3.

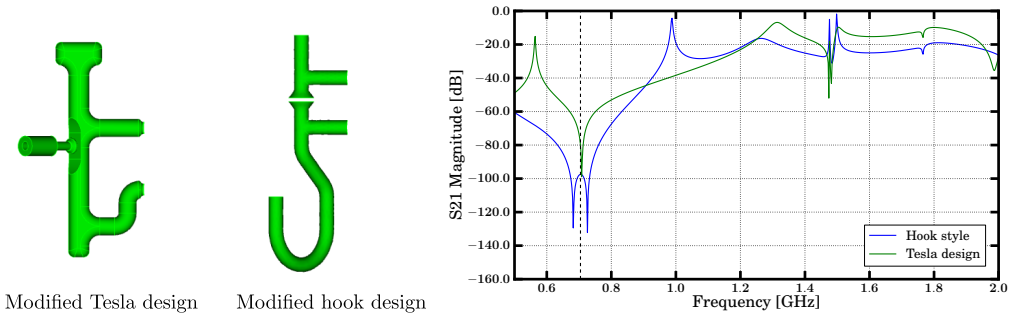

Figure 6.3: The final modified coupler designs along with their associated S21 performance.

This thesis was able to answer to the major question as to whether HOM couplers are required for ESS SRF linac. Removing the couplers from the baseline design reduces the cost of the machine as well as reduces the technical risk associated with couplers. It has been shown numerically that parasitic resonances in a proton linac are much less dangerous then first thought compared to previous experience relating to electron linacs in particular dipole modes.

Bibliography

[1] Gustaf Ising. Prinzip Einer Methode Zur Herstellung Von Kanalstrahlen Hoher Voltzahl. *Arkiv fr matematik, astronomi och fysik*, 1924. 15

[2] Rolf Wideroe. Ueber Ein Neues Prinzip Zur Herstellung Hoher Spannungen. *Archiv fuer Elektronik und Uebertragungstechnik*, 1928. 15

[3] Large Hadron Collider (LHC). Homepage. `http://home.web.cern.ch/about/accelerators/large-hadron-collider`, 2013. 15

[4] European Organization for Nuclear Research (CERN). Homepage. `http://home.web.cern.ch`, 2013. 15

[5] Thomas Wangler. *RF Linear Accelerators*. Wiley VCH, 1998. 16

[6] International Linar Colider (ILC). Homepage. `http://www.linearcollider.org/ILC`, 2013. 16

[7] Chris Adolphsen, Maura Barone, Barry Barish, Karsten Buesser, Philip Burrows, et al. The International Linear Collider Technical Design Report - Volume 3.I: Accelerator & in the Technical Design Phase. 2013. 16

[8] A. Zholents. Major trends in linac design for x-ray fels. *LINAC12*, 2012. 16

[9] T. Raubenheimer. Lcls operation experience and lcls-ii design. *LINAC12*, 2012. 16

[10] K. Skld and D. Price. Neutron Scattering. *Academic Press*, 1986. 17

[11] Institut Laue-Langevin (ILL). Homepage. http://www.ill.eu/, 2013. 17

[12] ISIS. Homepage. http://www.isis.stfc.ac.uk/, 2013. 18

[13] Spallation Neutron Source (SNS). Homepage. http://neutrons.ornl.gov/, 2013. 18

[14] European Spallation Source (ESS). Homepage. http://europeanspallationsource.se/, 2013. 18

[15] Jean-Luc Biarrotte, Sebastien Bousson, Tomas Junquera, Alex C. Mueller, and Aurelia Olivier. A reference accelerator scheme for ads applications. *Nuclear Instruments and Methods in Physics Research Section A: Accelerators, Spectrometers, Detectors and Associated Equipment*, 562(2):656 – 661, 2006. 18

[16] H Abderrahim, P Kupschus, E Malambu, Ph Benoit, K Van Tichelen, B Arien, F Vermeersch, P Dhondt, Y Jongen, S Ternier, and D Vandeplassche. Myrrha: A multipurpose accelerator driven system for research and development. *Nuclear Instruments and Methods in Physics Research Section A: Accelerators, Spectrometers, Detectors and Associated Equipment*, 463(3):487 – 494, 2001. 18

[17] MYRRHA: Multi purpose hybrid research reactor for high-tech applications. Homepage. http://myrrha.sckcen.be/, 2013. 18

[18] Facility for Rare Isotope Beams (FRIB). Homepage. http://www.frib.msu.edu/, 2013. 18

[19] T2K. Homepage. http://t2k-experiment.org/, 2013. 19

[20] JPARC. Homepage. http://j-parc.jp/index-e.html, 2013. 19

[21] F Gerigk, , et al. *Conceptual design of the SPL II: A high-power superconducting H^- linac at CERN*. CERN, Geneva, 2006. 19

[22] Project X. Homepage. http://projectx.fnal.gov/, 2013. 19

[23] S. Peggs et al. *ESS Technical Design Report*. 2013. 21

[24] Andrzej Wolski. Theory of electromagnetic fields. 2011. 23

[25] J. D. Jackson. *Classical Electrodynamics*. Wiley, 1999. 25

[26] J.K. Sekutowicz. Superconducting elliptical cavities. 2012. 31

[27] A. Facco. Low and Medium Beta Superconducting Cavities. 2004. 34

[28] H. Padamsee. *RF Superconductivity: Science, Technology and Applications*. 2009. 34

[29] Frank Gerigk. Cavity types. 2011. 34

[30] G. Clemente, U. Ratzinger, H. Podlech, L. Groening, R. Brodhage, and W. Barth. Development of room temperature crossbar-¡span class=”aps-inline-formula”¿¡math display=”inline”¿¡mi¿h¡/mi¿¡/math¿¡/span¿-mode cavities for proton and ion acceleration in the low to medium beta range. *Phys. Rev. ST Accel. Beams*, 14:110101, Nov 2011. 34

[31] D. Alesini. Power coupling. 2011. 38

[32] W.D. Moeller. Design and technology of high-power couplers, with a special view on superconducting RF. 2011. 38

[33] E. Haebel. Couplers: Tutorial and update. *Part.Accel.*, 40:141–159, 1992. 38

[34] H.D. Graef. Experience with control of frequency, amplitude and phase. *Part.Accel.*, 40:127–140, 1992. 39

[35] S.N. Simrock. Experience with control of frequency, amplitude and phase. *Part.Accel.*, 46:117–130, 1994. 39

[36] Dragan Poljak. *Advanced Modeling in Computational Electromagnetic Compatibility*. Wiley, 2007. 41

[37] Ramesh Garg. *Analytical and Computational Methods in Electromagnetics*. Artech House, 2008. 41

[38] SLAC Advanced Computations Department. ACE3P. `https://portal.slac.stanford.edu/sites/ard_public/acd/Pages/Default.aspx`, 2013. 46

[39] Lie-Quan Lee, Zenghai Li, Cho Ng, and Kwok Ko. Omega3P: A Parallel Finite-Element Eigenmode Analysis Code for Accelerator Cavities. 2009. 46

[40] Arno Candel, Andreas Kabel, Lie-Quan Lee, Zenghai Li, Cho Ng, et al. State of the art in electromagnetic modeling for the Compact Linear Collider. *J.Phys.Conf.Ser.*, 180:012004, 2009. 46

[41] R. A. Marsh, F. Albert, S. G. Anderson, G. Beer, T. S. Chu, R. R. Cross, G. A. Deis, C. A. Ebbers, D. J. Gibson, T. L. Houck, F. V. Hartemann, C. P. J. Barty, A. Candel, E. N. Jongewaard, Z. Li, C. Limborg-Deprey, A. E. Vlieks, F. Wang, J. W. Wang, F. Zhou, C. Adolphsen, and T. O. Raubenheimer. Modeling and design of an x-band rf photoinjector. *Phys. Rev. ST Accel. Beams*, 15:102001, Oct 2012. 46

[42] National Energy Research Scientific Computing Center (NERSC). Homepage. `http://www.nersc.gov/`, 2013. 49

[43] G. Orly. Private communication. 50

[44] G. Constanza. Private communication. 50

[45] G. Devanz and J.Plouin. Conceptual design of the = 0.86 cavities for the superconducting linac of ess. *SRF11*, 2011. 50

[46] Marcel Schuh. Study of Higher Order Modes in Superconducting Accelerating Structures for Linac Applications. 57

[47] R. M. Kolbas and N. Holonyak. Man-made quantum wells: A new perspective on the finite square-well problem. *American Journal of Physics*, 52(5):431–437, 1984. 62

[48] 704 MHz Cavity Design. `http://rcalaga.web.cern.ch/rcalaga/704MHz/`, 2013. 63

[49] W. K. H. Panofsky and W. A. Wenzel. Some considerations concerning the transverse deflection of charged particles in radio-frequency fields. *Review of Scientific Instruments*, 27(11):967–967, 1956. 67, 70

[50] Perry B. Wilson and James E. Griffin. High energy electron linacs; application to storage ring rf systems and linear colliders. *AIP Conference Proceedings*, 87(1):450–555, 1982. 68

[51] Marcel Schuh, Frank Gerigk, Joachim Tuckmantel, and Carsten P. Welsch. Influence of higher order modes on the beam stability in the high power superconducting proton linac. *Phys.Rev.ST Accel.Beams*, 14:051001, 2011. 69, 70

[52] J. Tuckmantel. Beam simulations with initial bunch noise in superconducting rf proton linacs. *Phys.Rev.ST Accel.Beams*, 13:011001, 2010. 69, 70

[53] Linear Dynamics in Particle Accelerators. `http://pcwww.liv.ac.uk/~awolski/main_teaching_Cockcroft_LinearDynamics.htm`, 2013. 70

[54] HOMDynamics code. `https://code.google.com/p/homdynamics/`, 2013. 70

[55] TraceWin. `http://irfu.cea.fr/Sacm/logiciels/index3.php`, 2013. 71, 83

[56] Python. `http://www.python.org/`, 2013. 72

[57] Makoto Matsumoto and Takuji Nishimura. Mersenne twister: a 623-dimensionally equidistributed uniform pseudo-random number generator. *ACM Trans. Model. Comput. Simul.*, 8(1):3–30, January 1998. 72

[58] M Schuh, J Tckmantel, JL Biarrotte, and D Kaltchev. Code Benchmarking of Higher Order Modes Simulation Codes. Technical Report sLHC-Project-Note-0010. CERN-sLHC-Project-Note-0010, CERN, Geneva, Jan 2010. 72

[59] S. Molloy. An empircal study of hom frequencies. (92). 74

[60] M. Eshraqi. Private communication. 83

[61] T. Khabiboulline et al. Experiments on hom spectrum manipulation in a 1.3 ghz ilc sc cavity. *PAC11*, 2011. 85

[62] K. Honkavaara et al. Status of flash. *IPAC12*, 2012. 85

[63] J. Sekutowicz. Higher order mode coupler for TESLA. 1994. 100

[64] R. Calaga. Some aspects of 704 mhz superconducting rf cavities. *currently unpublished*. 100

[65] C. Potratz et al. Coupler design and optimization by gpu accelerated dg-fem. *IPAC11*, 2011. 101

[66] S. Kim. Sns superconducting linac operational experience and upgrade path. *LINAC08*, 2008. 102, 109

[67] I. E. Campisi, F. Casagrande, M. T. Crofford, Y. W. Kang, S. H. Kim, et al. Status of the sns cryomodule test'. 2007. 102

[68] R. H. Fowler and L. Nordheim. Electron emission in intense electric fields. *Proceedings of the Royal Society of London. Series A*, 119(781):173–181, 1928. 103

[69] H. Padamsee, J. Knobloch, and T. Hays. *RF Superconductivity for Accelerators*. 1998. 104, 107

[70] C. E. Reece, E. F. Daly, G. K. Davis, W. R. Hicks, T. Rothgeb, H.L. Phillips, J. Preble, H. Wang, , and G. Wu. Diagnosis, analysis, and resolution of thermal stability issues with hom couplers on prototype cebaf srf cavities. *SRF2007*, 2007. 109

[71] Lixin Ge, Kwok Ko, Ki Lee, Zenghai Li, Cho-Kuen Ng, et al. Analyzing Multipacting Problems in Accelerators using ACE3P on High Performance Computers. page MOSDI1, 2012. 109

[72] Wencan Xu, Z. Altinbas, S. Belomestnykh, I. Ben-Zvi, M. Cole, et al. Design, simulations, and conditioning of 500 kW fundamental power couplers for a superconducting rf gun. *Phys.Rev.ST Accel.Beams*, 15:072001, 2012. 109

[73] M.A. Furman and M.T.F. Pivi. Probabilistic model for the simulation of secondary electron emission. *Phys.Rev.ST Accel.Beams*, 5:124404, 2002. 110

[74] Herman Blinchikoff and Anatol Zverev. *Filtering in the Time and Frequency Domains*. SciTech, 2001. 117

[75] Tetsuo Abe, Tatsuya Kageyama, Hiroshi Sakai, Yasunao Takeuchi, and Kazuo Yoshino. Multipactoring suppression by fine grooving of conductor surfaces of coaxial-line input couplers for high beam current storage rings. *Phys. Rev. ST Accel. Beams*, 13:102001, Oct 2010. 120

[76] W. Xu et al. New hom coupler design for high current srf cavity. *IPAC11*, 2011. 121